

Cylinder Drag Reduction Using Discrete Surface Roughness

An Experimental Investigation Into the Effect of Cylindrical Roughness Elements

Prajwal Deval

Delft University of Technology



Cylinder Drag Reduction Using Discrete Surface Roughness

An Experimental Investigation Into the Effect of
Cylindrical Roughness Elements

by

Prajwal Deval

to obtain the degree of Master of Science
at the Delft University of Technology,
to be defended publicly on the 29th August, 2023 at 10:00 AM.

Student number: 4811526

Project duration: December 1, 2022 – August 29, 2023

Thesis committee:	Dr.ir. B.W. van Oudheusden	Chair	TU Delft, Aerodynamics
	Dr. W. Yu	Examiner	TU Delft, Wind Energy
	Dr. A. Sciacchitano	Supervisor	TU Delft, Aerodynamics
	Dr. W. Terra	Supervisor	NOC*NSF Embedded Scientist, Aerodynamics

Cover: Accessed from Rutger Pauw under CC (modified)

Preface

This thesis represents a culmination of my MSc study student at TU Delft. The past 9 months have been a process of learning, understanding, relearning and applying; something I have thoroughly enjoyed. For this experience, I would like to especially thank my supervisors Andrea and Wouter for their invaluable insight which has helped me in producing this work. Without their support, it would not have been possible to complete it, let alone within the 9 nominal months reserved for the thesis.

This thesis not only turns me from an engineering student to an engineer but also marks the end of my student life at TU Delft. It is impossible to look back at the last five years of the bachelor and master without extending gratitude to my closest people Manolaki, Mira, Aytok, Alex, Gopal, Irmak, Manolo and Octavian. You have been my unconditional support and I would be lying if I claimed I didn't depend on you all for keeping me going during the toughest of times. I can never thank you enough for the days and nights of resolute encouragement I have been lucky to receive.

Most of all, my gratitude for allowing me the greatest of opportunities to study and unlock new worlds goes to my lovely family. धन्यवाद, की आपने मुझे हमेशा आगे बढ़ने की शक्ति दी और मुझ पर भरोसा रखा, प्रणाम।

Prajwal Deval
Delft, August 2023

Abstract

This thesis investigates the influence of Cylindrical Distributed Roughness Elements (polka-dots) on cylinder flow, with a focus on potential applications in sports aerodynamics. The primary goals are twofold: to explore the mechanism behind tripping and to analyse how the dimensions (height, width, spacing) of polka-dots affect flow characteristics.

The research employs an experimental approach, utilising balance measurements to quantify drag within the relevant Reynolds number range experienced by the limbs of speed-skaters. Additionally, Particle Image Velocimetry (PIV) measurements are conducted to examine the boundary layer and wake flow, revealing insights into how different polka-dot geometries impact flow characteristics.

11 polka-dot configurations were tested wherein the polka-dot height, diameter and spanwise (flow-normal) spacing was varied. Two PIV domains were imaged: the boundary layer flow before and after the polka-dot (covering an azimuthal range of about 40° of the circular profile), and the wake domain of the cylinder (about 2 diameters into the downstream flow). The boundary layer flow images were used to characterise the flow seen by the polka-dot array, and how it is affected by changes in the polka-dot geometry. The wake domain PIV imagery was used to examine the shape and dimensions of the cylinder wake.

Among the 11 tested polka-dot configurations, 10 effectively triggered drag reduction to varying extents within the relevant regime. The minimum drag coefficient was achieved by the configuration with the polka-dots of greatest diameter. It was also seen that increasing polka-dot height is likely to cause premature separation which is further exacerbated by a narrower polka-dot spacing.

In general, results indicate that shorter and wider polka-dots cause transition at lower Reynolds numbers, and a greater reduction in drag occurs when transition takes place at higher Reynolds numbers. Polka-dots placed in closer proximity initiate flow tripping earlier, while wider spacing results in more substantial drag reduction. However, it is observed that the polka-dots, when spaced closer together, see a lower flow velocity for the same polka-dot height and may lead to premature separation.

In terms of the wake width, a high linear correlation is seen between the measured wake width and the measured coefficient of drag ($r^2 \approx 0.9$). It is also seen that for drag coefficient values close to the minimum drag coefficient value, the wake width sees minimal change. The change in wake geometry is then seen as a change in the wake tapering (downstream decrease of the wake width) and the streamwise wake length. Therefore, a larger wake imaging domain in the streamwise direction is likely to allow for a more accurate correlation of the wake geometry and the drag coefficient.

While the study offers valuable insights, several recommendations are put forth for further research. Expanding the wake imaging domain is suggested to enhance correlations with the drag coefficient, and investigating spanwise flow variations would provide deeper insight into the tripping mechanism.

Contents

Preface	iii
Abstract	v
Nomenclature	ix
1 Introduction	1
2 Cylinder Aerodynamics & Drag Reduction	3
2.1 Sports Aerodynamics	3
2.2 Cylinder Flow	5
2.2.1 Viscous Flow Regime	6
2.2.2 Subcritical Flow	7
2.2.3 Critical Flow	8
2.2.4 Supercritical Flow	9
2.2.5 Transcritical Flow	9
2.2.6 Regime of Interest	11
2.3 Approaches to Drag Reduction	16
2.3.1 Tripping Mechanism and Its Effect	17
2.3.2 Tripping Potential of an Element	18
2.4 Research Questions	21
3 Particle Image Velocimetry	23
3.1 Principles of PIV Measurement	23
3.2 PIV Processing Techniques	25
4 Experimental Setup	27
4.1 Cylinder Models	28
4.1.1 Cylinder Geometry	28
4.1.2 Manufacturing of Wind Tunnel Models	30
4.2 Wind Tunnel	32
4.3 Balance Measurements	34
4.3.1 Physical Attachment	34
4.3.2 Balance Details	35
4.3.3 Measurement Methodology	36
4.4 Particle Image Velocimetry	36
4.4.1 PIV Setup	37
4.4.2 PIV Processing	39
4.5 Data Reduction	40
4.5.1 Balance Data	40
4.5.2 PIV Data	40
5 Results	47
5.1 Bare Cylinder Results	48
5.2 Polka-Dot Analysis	51
5.2.1 Effect of Polka-Dot Height	51
5.2.2 Effect of Polka-Dot Aspect Ratio	57
5.2.3 Effect of Polka-Dot Spacing	62
5.3 Wake Width Analysis	66
6 Conclusions and Recommendation	73
6.1 Conclusions	73
6.1.1 Effect of Polka-Dot Height	74

6.1.2	Effect of Polka-Dot Diameter	75
6.1.3	Effect of Polka-Dot Spacing	75
6.1.4	Wake Flow Analysis	75
6.2	Recommendations	76
References		79
A	Boundary Layer Flow Contours	83

Nomenclature

Abbreviations

Abbreviation	Definition
DNS	Direct Numerical Simulation
DRE	Discrete Roughness Element
FDM	Fused Deposition Modelling
FoV	Field of View
HSL	High Speed Laboratory
ISA	International Standard Atmosphere
PIV	Particle Image Velocimetry
RPM	Revolutions Per Minute
TrBL	Transition in Boundary Layer
TrSL	Transition in Shear Layer
TrW	Transition in Wake

Symbols

Symbol	Definition	Unit
A	Athlete reference area	m^2
AR	Polka-dot aspect ratio	-
$C_{d,min}$	Minimum C_d	-
C_D	Athlete drag coefficient	-
C_d	Cylinder 2D drag coefficient	-
C_f	Frictional drag coefficient	-
$C_{p,b}$	Base pressure coefficient	-
C_p	Pressure coefficient	-
D	Cylinder diameter	mm
d	Polka-dot diameter	mm
H	Shape factor	-
k	Roughness height	mm
l	Cylinder length	cm
r	Radial direction	mm
R_{AB}	Cross correlation function of images A & B	-
Re	Cylinder Reynolds number	-
Re_{crit}	Critical cylinder Reynolds number	-
$Re_{k,crit}$	Critical roughness height based Reynolds number	-
Re_k	Roughness height based Reynolds number	-
S	Polka-dot spacing	mm
t_i	Time level i	s
u	Mean x-velocity	m/s
u'	Standard deviation of x-velocity	m/s
u_k	Flow velocity at height k	m/s
V	Athlete velocity	m/s

Symbol	Definition	Unit
V_{corr}	Corrected velocity	m/s
V_{unc}	Uncorrected velocity	m/s
V_{∞}	Free stream velocity	m/s
δ_{95}	Boundary layer 95% thickness	mm
δ^*	Boundary layer displacement thickness	mm
ϵ	Wind-tunnel blockage	-
ϵ_{sb}	Solid blockage	-
ϵ_{wb}	Wake blockage	-
θ	Boundary layer momentum thickness	mm
ν	Kinematic viscosity	m ² /s
ρ	Density	kg/m ³
ϕ	Azimuth	°

List of Tables

2.1	Parameters that athlete drag is a function of (ρ , V , C_D and A) and how they can be controlled by changes made by the athlete and in the athlete's garment.	4
2.2	Flow regimes of a right circular cylinder presented with the respective Reynolds number ranges. It is important to note that these numbers can vary depending upon free stream turbulence, surface roughness and vibrations in the flow.	5
2.3	Ranges of Reynolds numbers experienced at the ankle and calf of male speed-skaters based on the average speed of world record times in December 1997. Adapted from Timmer and Veldhuis [33].	11
4.1	Parameters and their symbols used to parameterise the polka-dot configurations.	28
4.2	The dimensions of polka-dot configurations in series A and B cylinders where the polka-dot height is varied as signified by the grey column.	29
4.3	The dimensions of polka-dot configurations in series C cylinders. The column highlighted in grey signifies that within this series, only the diameter (and therefore the aspect ratio too) is varied.	30
4.4	The dimensions of polka-dot configurations in series D cylinders. The pairs of rows highlighted together correspond to the configurations where the individual polka-dots have identical height and aspect ratio such that the only change between them is the spacing as signified by the grey column.	30
4.5	Specification of the equipment and software used in the PIV setup.	37
4.6	The optical and laser related variables of each of the PIV setups.	39
5.1	The measured values of Re_k for each of the series C configurations ($k = 1.5$ mm, $S/d = 1.5$) at each measured cylinder Reynolds number.	58
5.2	The measured values of Re_k for each of the series A configurations ($d = 1.5$ mm, $S/d = 1.5$) at each measured cylinder Reynolds number.	66
5.3	The measured values of Re_k for each of the series B configurations ($d = 1.5$ mm, $S/d = 2.5$) at each measured cylinder Reynolds number.	66
5.4	The r^2 scores for the regression of the C_d with the wake width measured at different downstream locations of the cylinder.	67
6.1	The effect of polka-dot geometrical parameters on the drag and flow characteristics of the cylinder.	74

List of Figures

1.1	A cylinder model fitted with polka-dots as was used in this research.	1
2.1	The incremental improvement in the world record time for the 5000m men's speed-skating event between 1972 and 2018.	4
2.2	The two coordinate systems used in this report (Cartesian marked in red and cylindrical marked in blue).	5
2.3	A sketch and smoke flow-visualisation image of a cylinder in the creeping viscous regime where no flow separation is seen.	6
2.4	A sketch and smoke flow-visualisation image of a cylinder in the separated symmetric viscous flow regime. Here, flow is separated, but still fully laminar, symmetrical and steady.	6
2.5	A fully laminar von Karman vortex street formed in the wake of a cylinder at $Re = 150$ adopted from Williamson [36].	7
2.6	Satellite image of clouds visualising the shed vortices from a volcano (bottom left) acting as a disturbance in atmospheric flow. As the shed vortices propagate to the top right of the frame, the flow breaks into full turbulence, corresponding to the 'TrW' state of flow as termed by Zdravkovic [37].	8
2.7	A sketch and an image of different substages of the the subcritical regime. Figure 2.7a corresponds to TrSL3 where the flow is immediately turbulent after laminar separation while Figure 2.7b corresponds to TrSL2 where the laminar wake develops and propagates before Kelvin-Helmholtz eddies (termed disturbance eddies by Zdravkovich) are seen in the shear layer interface.	8
2.8	Flow visualisation showing one side of with a successful transition and reattachment of flow and the other undergoing laminar separation. As a result, the wake is asymmetrical and there is a large difference in separation location on each side. Since there is a net deflection of the airflow in the positive-y direction, there will be a non-zero sideforce measured in the negative-y direction. Adopted from Bozhkov et al. [5].	10
2.9	A sketch and image of a cylinder in critical flow. The boundary layer transitions to turbulent and the separation is turbulent.	10
2.10	Sketch adopted from van Moll [18] of a cylinder in supercritical flow. The boundary layer transitions to turbulent without forming a laminar separation bubble (at the angular location marked ϕ_t).	11
2.11	Cylinder drag coefficient plotted against Reynolds number [24] [35].	12
2.12	The drag coefficient varying with Reynolds number around the regime of interest.	13
2.13	The friction drag expressed as a proportion of total drag over a range of Reynolds numbers [32] [1].	13
2.14	Pressure distribution about a cylinder in the subcritical ($Re = 1.1 \cdot 10^5$), critical ($Re = 6.7 \cdot 10^5$), supercritical ($Re = 8.5 \cdot 10^6$) flow regimes [12][13][24]. The potential flow solution is also presented here for reference.[2]	14
2.15	The negative pressure coefficient obtained experimentally and plotted against Reynolds number [12] [13] [24].	15
2.16	Flowchart highlighting the techniques used for and the consequential flow changes that arise from reducing the drag of a cylinder. The red crosses signify branches that are impractical or impossible for implementation on skin-suits and the yellow crosses signify the branches that are not considered in this research.	16
2.17	Examples of discrete roughness elements to trip the flow adopted from Demartino and Ricciardelli.[10]	17

2.18	The mechanisms in the four stages of roughness induced transition visualised through a DNS carried out by Suryanarayanan et al.[29]	18
2.19	The experimental study carried out by von Doenhoff and Braslow regarding the effect of spanwise spacing on tripping potential.	20
3.1	A typical PIV setup. Adopted from Raffel et al.[20]	24
3.2	The PIV as used by Brown for assessing cyclist wake aerodynamics. Adopted from Brown [6].	24
3.3	An interrogation window shown from two subsequent PIV images. The first frame is captured at time t_1 and the second at time t_2 . The inferred fluid velocity in this window is shown with the arrow in the middle.	25
3.4	A visualisation of the averaging of the correlation as presented by Meinhart et al. [17]	26
3.5	A pictorial representation of the order of computation and averaging carried out in the (a) average velocity method and (b) average correlation method. The number of image pairs is shown to be 200 since all PIV runs used an ensemble of 200 image pairs.	26
4.1	An explanation of the polka-dot dimensions d , k , and S . Two polka-dots out of an array are shown here. The hatched area represents the cylinder surface.	29
4.2	A schematic representation of the dimensions of the polka-dot pattern printed on the photo-paper before being wrapped over the cylinders.	31
4.3	The cylinders sleeves after being taped into the a round shape to fit over the PVC pipe base.	32
4.4	The W-Tunnel at the TU Delft HSL.	33
4.5	The drag curve of a cylinder presented with the regime of interest as shown in Section 2.2.6, and the Reynolds number attained in the experimental campaign.	33
4.6	Experimental setup showing the cylinder attached to the force balance using the mounting fixture.	35
4.7	A schematic representation of the PIV setup showing the cylinder in the flow and the two fields of view present (not to scale).	37
4.8	A picture of the two PIV cameras positioned relative to the cylinder. The calibration boom is only used during the capturing of images for scaling. When the PIV measurements are carried out, the calibration boom is removed altogether.	38
4.9	The estimation of the cylinder profile location in FoV 1 for cylinder 5 ($k = 1.5$ mm, $d = 3$ mm). In both subfigures, the plotted quantity is the velocity magnitude, but a colorbar is not shown as this quantity is not of interest here.	41
4.10	A schematic overview of the boundary layer profile extraction. The vertical axis in the shown plot corresponds to the thick red line shown at angle ϕ where the velocity is sampled.	42
4.11	Schematic representation of the wake profile analysis carried out. The mean velocity profile (u_{mean}) is shown in red and the velocity fluctuation profile (u') is shown in green. The two maximum fluctuation points mark the upper and lower boundary of the wake.	43
4.12	The process of the calculation of the wake width shown for cylinder 6 at $Re = 1.5 \cdot 10^5$. The black circles mark the calculated location of the cylinder profile in the measurement domain, freestream flow is in the positive x-direction.	44
4.13	The profile of the standard deviation of the streamwise velocity normalised with the freestream velocity at $x = 100$ mm. The red horizontal lines mark the locations of the wake boundary calculated from the maximum turbulence intensity.	45
5.1	The coefficient of drag plotted against Reynolds number for a bare cylinder.	48
5.2	Boundary layer flow of the bare cylinder at different Reynolds numbers within the tested regime. Laminar separation is seen in all of the flow figures.	49
5.3	Boundary layer profiles for the bare cylinder shown at $V = 5$ m/s, 10 m/s, 15 m/s and 20 m/s. Each sub-figure shows the profiles for 4 different azimuthal position.	50
5.4	The effect of polka dot height as seen in the drag coefficient of the cylinders. Here, polka-dot diameter is constant for spacing of (a) 1.5 diameters and (b) 2.5 diameters.	52

5.5	Boundary layer profiles of series A ($S/d = 1.5$) cylinders 10 ($k = 1\text{mm}$), 9 ($k = 1.5\text{mm}$) and 11 ($k = 2.2\text{mm}$) at three different azimuthal locations. $Re \approx 0.9 \cdot 10^5$.	54
5.6	The mean boundary layer flow for cylinder 12 at $Re = 0.9 \cdot 10^5$. The flow is separated from $\phi = 60^\circ$.	55
5.7	The mean boundary layer flow for cylinder 12 at $Re = 0.9 \cdot 10^5$. The flow is attached immediately after the polka-dot but is separated thereafter.	56
5.8	Boundary layer velocity profiles of series B cylinders at $\phi = 70^\circ$. $Re \approx 0.9 \cdot 10^5$.	57
5.9	Drag data presented for Series C cylinders. Here, polka-dot diameter is varied for a constant height ($k = 1.5\text{ mm}$) and spacing ($S/d = 1.5$).	58
5.10	Boundary layer images of cylinder 5 before and after the drag crisis is triggered by the polka-dot.	60
5.11	Comparison of the shape factor of the series C cylinders 3 and 5 in the range $70^\circ < \phi < 80^\circ$. The shape factor is also plotted for the bare cylinder boundary layer for reference.	61
5.12	Comparison of the boundary layer profiles of cylinder 3 ($k = 1\text{ mm}$), cylinder 5 ($k = 3\text{ mm}$) and the bare cylinder at $\phi = 75^\circ$.	62
5.13	Comparison of the drag plots of the different pairs of cylinders with identical polka-dot dimensions but different polka-dot spacing. In each plot, the drag curves for the cylinder with the zigzag strip and the bare cylinder are also provided.	63
5.14	$C_{d,\min}$ plotted for different polka-dot heights for series A and B cylinders.	64
5.15	Shape factor plotted for cylinders 6 ($S/d = 2.5$) and 10 ($S/d = 1.5$). $k = 1\text{mm}$, $d = 1.5\text{mm}$.	65
5.16	Shape factor plotted for cylinders 2 ($S/d = 2.5$) and 9 ($S/d = 1.5$). $k = 1.5\text{mm}$, $d = 1.5\text{mm}$.	65
5.17	The averages streamwise wake velocities of the bare cylinder ($C_d = 1.1$) and cylinder 5 ($C_d = 0.7$). The bare cylinder has a visually wider wake that extends further downstream.	66
5.18	The streamwise wake flow standard deviation of the bare cylinder ($C_d = 1.1$) and cylinder 5 ($C_d = 0.7$). The bare cylinder has a visually wider wake that extends further downstream.	67
5.19	C_d plotted against the wake width sampled 0.82 diameters downstream of the cylinder trailing edge. $r^2 = 0.91$	68
5.20	The mean streamwise wake velocity plots of cylinder 10 ($k = 1\text{ mm}$, $d = 1.5\text{ mm}$, $S/d = 1.5$).	69
5.21	The standard deviation of streamwise wake velocity of cylinder 10 ($k = 1\text{ mm}$, $d = 1.5\text{ mm}$, $S/d = 1.5$).	70
5.22	The wake profile for cylinder 10 ($k = 1\text{mm}$, $d = 1.5\text{mm}$, $S/d = 1.5$) as it varies throughout the measurement regime.	71
5.23	C_d plotted against Reynolds numbers for cylinder 10. The range of the Reynolds numbers matches that of Figure 5.22.	71
6.1	The drag curve of a bare cylinder (obtained from Timmer and Veldhuis [33]) plotted together with that of cylinder 10. While the bare cylinder sees a levelling-off of the C_d at $C_{d,\min}$, the polka-dot equipped cylinder sees a further decline in its C_d .	74
A.1	Bare cylinder (cylinder 1).	84
A.2	Cylinder 2. $d = 1.5\text{ mm}$, $k = 1.5\text{ mm}$, $S/d = 2.5$.	85
A.3	Cylinder 3. $d = 1\text{ mm}$, $k = 1.5\text{ mm}$, $S/d = 1.5$.	86
A.4	Cylinder 4. $d = 2.2\text{ mm}$, $k = 1.5\text{ mm}$, $S/d = 1.5$.	87
A.5	Cylinder 5. $d = 2.2\text{ mm}$, $k = 3\text{ mm}$, $S/d = 1.5$.	88
A.6	Cylinder 6. $d = 1.5\text{ mm}$, $k = 1\text{ mm}$, $S/d = 2.5$.	89
A.7	Cylinder 7. $d = 1.5\text{ mm}$, $k = 2.2\text{ mm}$, $S/d = 2.5$.	90
A.8	Cylinder 8. $d = 1.5\text{ mm}$, $k = 3\text{ mm}$, $S/d = 2.5$.	91
A.9	Cylinder 9. $d = 1.5\text{ mm}$, $k = 1.5\text{ mm}$, $S/d = 1.5$.	92
A.10	Cylinder 10. $d = 1.5\text{ mm}$, $k = 1\text{ mm}$, $S/d = 2.5$.	93
A.11	Cylinder 11. $d = 1.5\text{ mm}$, $k = 2.2\text{ mm}$, $S/d = 1.5$.	94

A.12 Cylinder 12. $d = 1.5$ mm, $k = 3$ mm, $S/d = 1.5$	95
---	----

1

Introduction

In human-powered racing sports such as ice-skating, skiing or cycling, aerodynamic drag is the primary driver of the total resistance force on an athlete [8]. Through the optimisation of athlete posture, motion and surface aerodynamics, the aerodynamic drag on the athlete can be reduced. This study focuses on the flow on the surface of the athlete's suit and techniques used to reduce drag by altering the surface characteristics. The typical technique used is to artificially trip the boundary layer on the athlete's body such that flow separation is delayed. An example of this implementation is that presented by Timmer and Veldhuis of the use of zigzag strips on ice-skater skin suits [33]. Similarly, this research focuses on using cylindrical discrete roughness elements (polka-dots) in order to trip the flow and delay separation on the limbs of ice-skaters. A representation of such a model is depicted in Figure 1.1. The polka-dots are applied in an array along the longitudinal length of the cylinder.

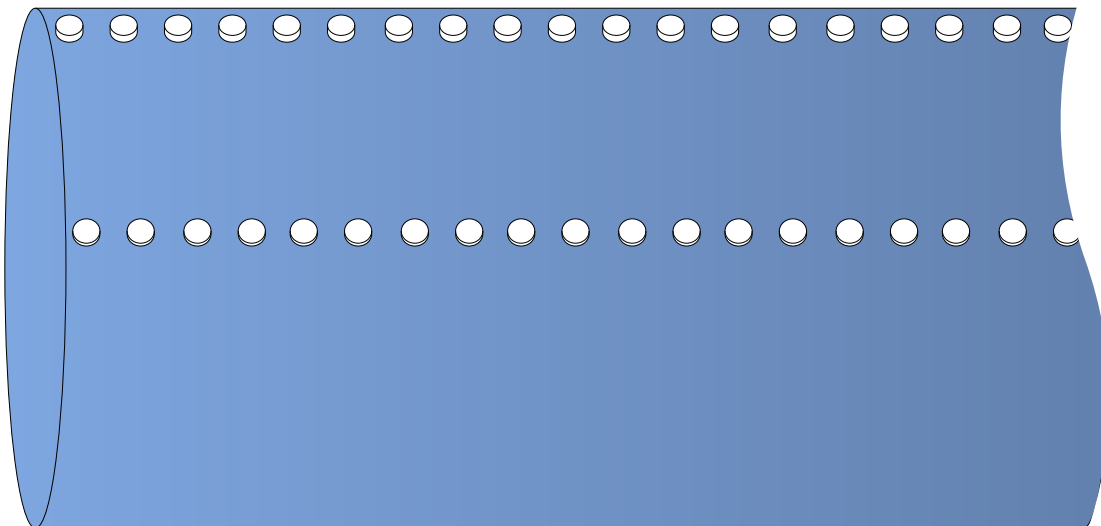


Figure 1.1: A cylinder model fitted with polka-dots as was used in this research.

Polka-dots present an alternative to zigzag strips in terms of manufacturability for they have a relatively simple geometry. While polka-dots have previously been assessed for their tripping potential, there is a pronounced lack of literature on the effect a large pressure gradient, such as that found in the flow around a cylinder, has on their tripping performance. For this research, the geometry used is a cylinder on which different configurations of polka-dots are applied and their aerodynamic performance assessed. The use of polka-dots as tripping elements finds value not only in sports aerodynamics but also in other fields where drag reduction of bluff bodies and passive flow control

is of interest. Examples include civil engineering as presented by Demartino and Ricciardelli [10], wind energy as presented by Zheng et al. [38] and aviation as presented by Lyon et al. [16].

This research aims to assess the use of polka-dots as discrete roughness elements to reduce cylinder drag within a specifically identified regime of interest. The regime focused upon is the typical flow regime the limb of an ice-skater sees. The main aim of the research is to increase the existing knowledge base regarding polka-dot and discrete roughness tripping within large pressure gradients. In specific, an attempt to characterise the effect of polka-dot geometry and spacing is made.

For this research, 11 different polka-dot geometries were assessed experimentally. Within the 11 configurations, the polka-dot height, diameter and spacing were systematically varied so as to isolate the effect of each parameter as much as possible. Additionally, the same measurements were carried out for a bare cylinder without any tripping elements and also a cylinder with a zigzag strip applied to it. The research was carried out at the W-Tunnel in TU Delft's High Speed Laboratory. Balance measurements and Particle Image Velocimetry (PIV) were used to gain an insight into the effect of the polka-dots. A balance was used to measure the drag force, from which the coefficient of drag was calculated. Using PIV, the boundary layer and wake flows were imaged. These were used to obtain boundary layer shape factor and wake topology respectively.

Chapter 2 first presents the background for the research. It includes an overview of the importance of drag reduction in sports aerodynamics. Following this, a concise review of cylinder aerodynamics is put forth, presenting the characteristics of the drag force acting on the cylinder in different Reynolds number regimes. The regime of interest is also presented here along with a comprehensive analysis of drag reduction techniques in order to motivate the choice of discrete roughness elements. The tripping mechanism and present literature regarding polka-dot and discrete roughness tripping are also presented here. Lastly, the research questions are also presented here. Following this, Chapter 3 introduces PIV and its applications in analysing fluid flow characteristics. It covers the principles of PIV, image acquisition, and data processing techniques relevant to the research.

Chapter 4 presents the specific experimental setup used in this research. Details about the cylinder models and their manufacturing are provided. The wind-tunnel setup along with the balance and PIV setup is presented here. Finally, the data processing that is carried out is explained and justified. Chapter 5 presents an analysis of the results. The effect of polka-dot height, diameter and spacing are presented through the use of drag figures, boundary layer characteristic data and wake topology. Based on this, Chapter 6 presents the conclusions drawn from the results in the context of the research questions. Based on these results, recommendations are also made for further research into polka-dot flow tripping and relevant applications to sports aerodynamics.

2

Cylinder Aerodynamics & Drag Reduction

This chapter provides a comprehensive overview of the background and theoretical foundations relevant to the research. It sets the stage for the subsequent chapters by discussing key concepts and theories that form a basis for the research. The chapter begins by exploring the field of sports aerodynamics in Section 2.1, examining the importance of optimising the aerodynamic performance of sports equipment.

Section 2.2 delves into the study of cylinder flow, which is essential for understanding the flow around athletes' bodies. This section discusses the flow patterns and phenomena associated with cylindrical shapes and their implications in terms of drag.

Furthermore, Section 2.3 addresses drag reduction theory, presenting the practical implications of different techniques. It then delves into the theory surrounding roughness induced transition and how it leads to a reduction in the drag.

Finally, section 2.4 formulates the research questions that guide this research. These research questions encapsulate the objectives of the research project and provide a clear direction for the subsequent chapters. The methods and results presented in Chapter 4 and Chapter 5 respectively refer back to these research questions.

By comprehensively examining the background and theoretical underpinnings in this chapter, a solid foundation is established for the subsequent research and analysis presented in the following chapters.

2.1. Sports Aerodynamics

In sports where the aim is to minimise the time required to cover a given distance, optimising the net propulsive force on the athlete is crucial. This net force can be broken down into the difference between the applied propulsive force and the resistance force against motion. In the context of ice-skating, the primary resistance factor is aerodynamic drag [19].

This can be illustrated by referring to Figure 2.1, where Timmer and Veldhuis [33] demonstrate the significant improvement in the men's 5000 m speed-skating world record. The most notable improvement occurred in 1998 at Nagano when Gianni Romme utilised a suit fitted with zigzag strips to reduce his body's drag. Additionally, the second and third largest improvements (achieved by Stensjemmet and Baranov respectively) took place at Medeo, Kazakhstan, located at an altitude of 1961 m above sea level. It is worth noting that the zigzag strips reduce the drag coefficient C_D (the mechanism of which is explained in Section 2.3), while the higher altitude results in a lower

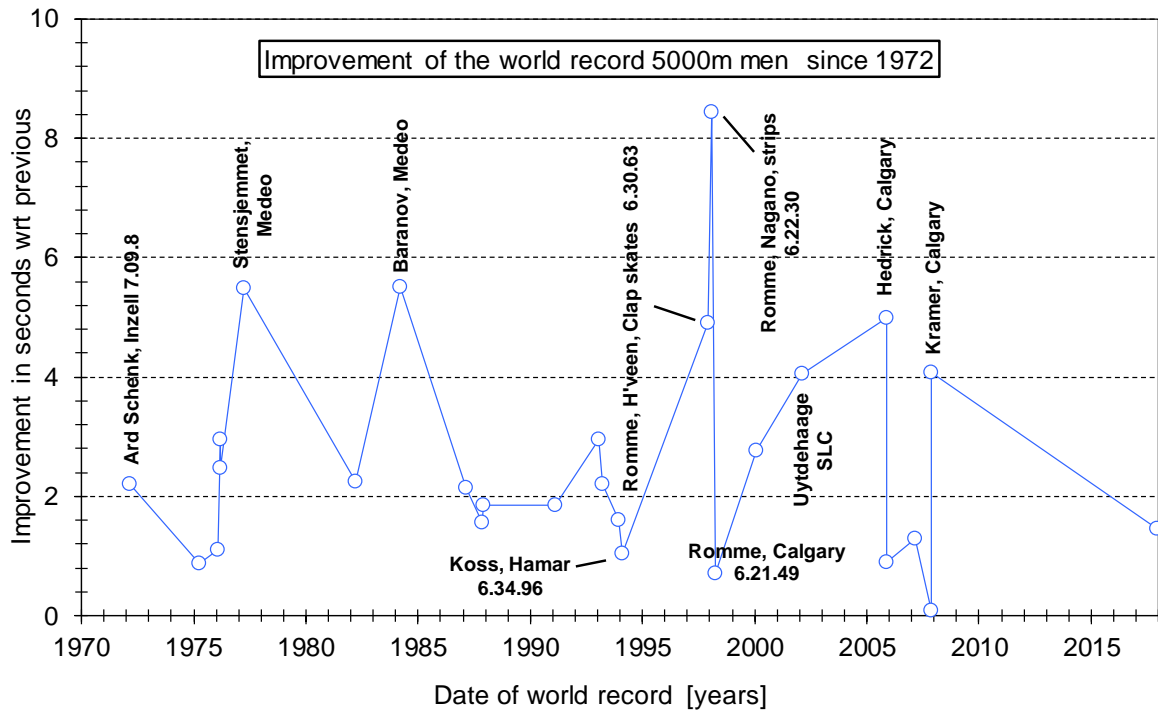


Figure 2.1: The incremental improvement in the world record time for the 5000m men's speed-skating event between 1972 and 2018.

air density ρ . Both of these factors contribute to reducing the total drag force acting on the athlete.

A more universal look at the ways to affect the drag acting on the athlete is presented in Table 2.1. For example, based on the research of Kyle and Brownlie [9] it was found that the increase in the frontal area of an athlete caused by loose clothes can increase the drag of an athlete by up to 40% at the same free stream velocity. Along similar lines, an optimisation of cyclist seating position carried out by Schaffarczyk et al. [26] showed almost a factor 2 difference in drag coefficient between the best and worst postures of cyclists. This translated to a time gained of roughly 1 hour over a 180 km Ironman cycling course at a given power output.

The focus of this research is the effect on the total drag of the garment surface aerodynamic characteristics. It zooms into the flow of air around the arms and legs of the skaters. In order to simplify the research, the athlete's limbs are modelled as cylinders. This allows for a large amount of research existing in other fields such as civil engineering to be applied while still emulating the high pressure gradients that the true geometry experiences. This simplification is also made by Brownlie in multiple works based on results by Konopov et al. that prove the similarity in the flow between athlete limbs and circular cylinders [8][7][15]. The following section provides an overview of relevant cylinder aerodynamics that forms a theoretical basis to study drag reduction techniques.

Table 2.1: Parameters that athlete drag is a function of (ρ , V , C_D and A) and how they can be controlled by changes made by the athlete and in the athlete's garment.

Athlete & Their Motion		Garment
ρ	No effect within incompressible range	No effect
V	Controllable but not of interest	No effect
C_D	Technique, posture	Surface aerodynamic characteristics
A	Technique, posture	Tight fit

2.2. Cylinder Flow

In this research, a ‘cylinder’ or ‘circular cylinder’ (used interchangeably) is defined as a prism with circular cross section. Furthermore, all cylinders in this research are ‘right circular cylinders’, i.e., the longitudinal axis of the cylinder is exactly perpendicular to the plane of the cross section.

Two coordinate systems are used in this report as shown in Figure 2.2. The first is the Cartesian ($x - y$) system. The x axis is the direction of free stream flow, therefore drag is measured in the positive x direction. The second system is the cylindrical ($r - \phi$) system. As shown, the green point A in Figure 2.2 has coordinates ϕ and r . ϕ is measured clockwise from the cylinder’s extremum in the negative x direction. Since in all cases the free-stream flow will be in the x direction, the stagnation point will also coincide with $\phi = 0$. Both systems share the same z axis which points out of the plane of the page from the centre of the cylinder.

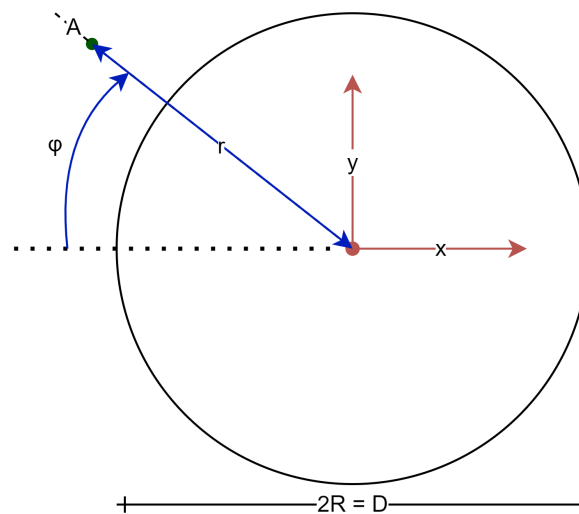


Figure 2.2: The two coordinate systems used in this report (Cartesian marked in red and cylindrical marked in blue).

Table 2.2: Flow regimes of a right circular cylinder presented with the respective Reynolds number ranges. It is important to note that these numbers can vary depending upon free stream turbulence, surface roughness and vibrations in the flow.

Regime	Minimum Re	Maximum Re
Viscous	0	150
Subcritical	150	$2 - 3 \cdot 10^5$
Critical	$2 - 3 \cdot 10^5$	$3 \cdot 10^6$
Supercritical	$3 \cdot 10^6$	10^7
Transcritical	10^7	-

The different regimes of flow around a cylinder are separated based upon Reynolds number. The Reynolds number represents the ratio of influence of the inertial forces on the flow to the viscous forces. Its formulation for a circular cylinder is presented in Equation (2.1) where U_∞ is the free stream flow velocity, D the sectional diameter and ν the kinematic viscosity of the fluid.

This document will use the canonically used regime names which are presented in table 2.2 along with their Reynolds number ranges. Each of the regimes is further explained in this

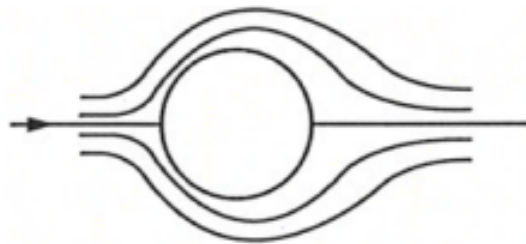
section. The information regarding the cylinder regimes and flow features are collated from the work of Roshko [24] and the seminal book of Zdravkovich [37].

$$Re = \frac{U_\infty D}{\nu} \quad (2.1)$$

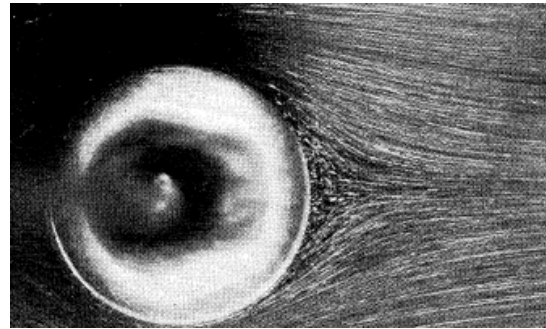
2.2.1. Viscous Flow Regime

This flow regime pertains to very low Reynolds numbers where viscous forces have much greater influence over the flow dynamics than the inertial forces. The flow therefore stays laminar in the whole regime. This high viscosity regime can be subdivided into further subregimes.

Below $Re = 5$, flow remains completely attached and never separates as illustrated in Figure 2.3. With increasing Reynolds number, a separation region is created behind the cylinder but the flow is still steady, i.e., at a given physical location the flow parameters remains unchanged in time. In the separation region, 2 eddies are formed on the leeward side of the cylinder. This flow state is shown in Figure 2.4. At approximately $Re = 30$ to 40, the eddies begin to propagate downstream from the cylinder. The well known von Karman vortex street is formed in this regime as seen in the smoke flow visualisation in Figure 2.5. It is to be noted in this subregime the flow around the cylinder and in the wake is still fully laminar. With increasing Reynolds number, the shedding frequency increases. Only at approximately $Re = 150$ to 300 the flow sees transition to turbulence. This transition is experienced within the released eddies due to the mixing in the flow and the fact that the velocity at this stage is high enough such that the viscous forces are not able to dampen all the disturbances in the shed vortices.

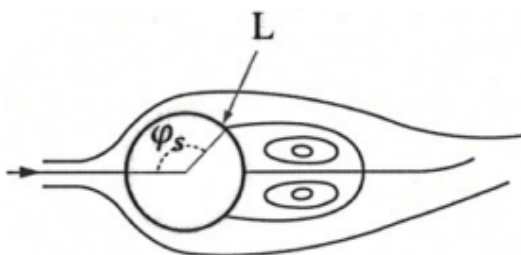


(a) Sketch of a cylinder in attached viscous flow regime adopted from van Moll [18].



(b) Image of a cylinder in smoke at $Re = 26$ adopted from Taneda [31].

Figure 2.3: A sketch and smoke flow-visualisation image of a cylinder in the creeping viscous regime where no flow separation is seen.



(a) Sketch of a cylinder in separated symmetric viscous flow regime adopted from van Moll [18]. The letter 'L' marks the location of laminar separation.



(b) Image of a cylinder in smoke at $Re = 118$ adopted from Taneda [31].

Figure 2.4: A sketch and smoke flow-visualisation image of a cylinder in the separated symmetric viscous flow regime. Here, flow is separated, but still fully laminar, symmetrical and steady.

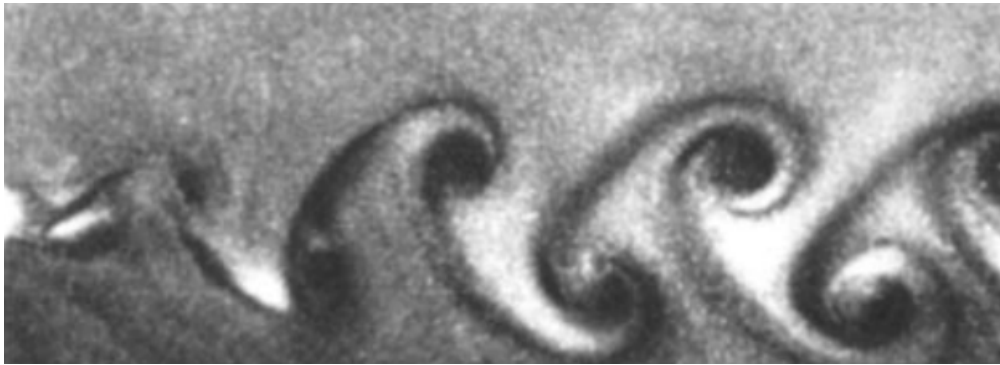


Figure 2.5: A fully laminar von Karman vortex street formed in the wake of a cylinder at $Re = 150$ adopted from Williamson [36].

2.2.2. Subcritical Flow

The subcritical regime ranges from $Re = 300$ to approximately $Re = 2 - 3 \cdot 10^5$. The lower limit corresponds to first transition to turbulence in the wake. As the Reynolds number is further increased, the transition point moves upstream in the wake until it reaches the separation point. With further increase in Reynolds number, the laminar separation point moves upstream along the circular profile and even reaches the windward side of the cylinder ($\phi < 90^\circ$). Throughout the subcritical flow regime the flow about the cylinder is fully laminar and only undergoes transition in the wake. The upper limit of the subcritical regime, depending upon certain geometrical and flow factors (explained further in Section 2.2.3) can range from $2 \cdot 10^5$ to $3 \cdot 10^5$. This is termed the *critical Reynolds number* (Re_{crit}) and is the lowest Reynolds number at which turbulent flow is seen by the boundary layer of the cylinder.

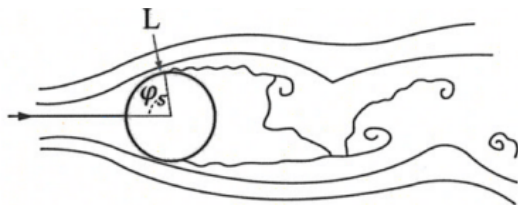
In the regime classification of Zdravkovich, the subcritical flow includes the region termed TrW (transition in wake) and the region termed TrSL (transition in shear layer). The following sub-regimes are classified:

- TrW1 ($180 - 200 < Re < 220 - 250$): Lower transition regime
- TrW2 ($220 - 250 < Re < 350 - 400$): Upper transition regime.
- TrSL1 ($350 - 400 < Re < 1 - 2 \cdot 10^3$): Development of transition waves.
- TrSL2 ($1 - 2 \cdot 10^3 < Re < 2 - 4 \cdot 10^4$): Development of transition eddies.
- TrSL3 ($2 - 4 \cdot 10^4 < Re < 1 - 2 \cdot 10^5$): Burst to turbulence.

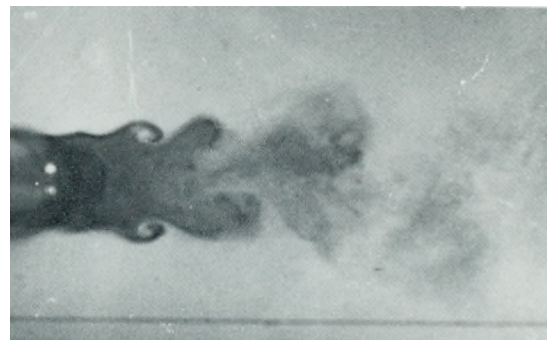
The difference between TrW and TrSL is that the location of the onset of turbulent flow is in the mixing of the shed vortices in TrW while on the other hand, in TrSL, the transition to turbulence is seen in the detached boundary layer which forms a shear layer with the separated flow region. TrW is seen in Figure 2.6 where the von Karman vortex street breaks into turbulence as it propagates downstream (towards the top right), while TrSL is seen in Figure 2.7 where the detached shear layer is what undergoes transition.



Figure 2.6: Satellite image of clouds visualising the shed vortices from a volcano (bottom left) acting as a disturbance in atmospheric flow¹. As the shed vortices propagate to the top right of the frame, the flow breaks into full turbulence, corresponding to the 'TrW' (transition in wake) state of flow as termed by Zdravkovic [37].



(a) A sketch of a cylinder in late stage subcritical flow. Point 'L' marks that the boundary layer is laminar when it detaches but the squiggly line indicates that the flow is turbulent immediately after detaching. Adopted from van Moll [18].



(b) Image of a cylinder in TrSL flow at $Re = 2 \cdot 10^3$ adopted from Gerrard and Lighthill [14].

Figure 2.7: A sketch and an image of different substages of the the subcritical regime. Figure 2.7a corresponds to TrSL3 where the flow is immediately turbulent after laminar separation while Figure 2.7b corresponds to TrSL2 where the laminar wake develops and propagates before Kelvin-Helmholtz eddies (termed disturbance eddies by Zdravkovich) are seen in the shear layer interface.

2.2.3. Critical Flow

The critical flow regime is bounded at the lower end by the aforementioned critical Reynolds number. Critical flow pertains to the regime in which the transition is seen in the boundary layer on the

¹Retrieved from: Bob Cahalan/NASA, USGS.

cylinder. Due to the strong pressure gradient, the boundary layer undergoes laminar separation, thereafter transitions and reattaches. This causes a sudden narrowing of the wake and also a reduction in drag due to greatly delayed separation. Furthermore, von Doenhoff and Braslow report that in this regime and higher Reynolds numbers, increasing the Reynolds number increases the number of turbulent bursts in the wake [34].

Depending upon factors such as the free stream turbulence and the surface roughness, Re_{crit} could lie anywhere between the approximate range of $2 - 3 \cdot 10^5$. Roshko reports the value to be $2 \cdot 10^5$ [24] while Skeide et al. report the value to be $3 \cdot 10^5$ [28]. With increasing free stream turbulence, and increasing surface roughness the general trend is a decreasing value of Re_{crit} . While this is generally true, it is reported by Rizzetta and Visbal that a small enough roughness element can actually arrest or discourage the development of the Tollmein-Schlichting instabilities that lead to transition further downstream [21].

Similar to the subcritical regime, Zdravkovich terms this regime and all regimes with greater Re to be 'TrBL' (transition in boundary layer). The following subregimes of TrBL lie in the critical flow region:

- TrBL0 (between transition point reaching boundary layer and separation bubble forming): Precritical regime. This is a transitional subregime between subcritical and critical only identified in the work of Zdravkovich.
- TrBL1 ($3 - 3.4 \cdot 10^5 < Re < 3.8 - 4 \cdot 10^5 k$): Re range where only one side of the cylinder forms a laminar separation bubble as seen in Figure 2.8. The wake is then asymmetrical and a side force (y-direction) coefficient of about 1.2 is generated [37].
- TrBL2 ($3.8 - 4 \cdot 10^5 k < Re < 0.5 - 1 \cdot 10^6$): Second separation bubble forms as seen in Figure 2.9, causing the wake to return to an a state of symmetry in the averaged flow field, and the time averaged side force coefficient also drops back to zero.

The coefficient of drag is seen to drop rapidly after the critical Reynolds number. This phenomenon is termed the *drag crisis*. The drag coefficient falls from about 1.25 to 0.2. This was first experimentally recorded and reported by Gustave Eiffel at his wind tunnel situated at the base of a tower named after himself [11].

Zdravkovich highlights the region in which there is only one side of the symmetric profile which experiences the separation bubble. This is likely due to the fact that in his work, the side force was also measured and this asymmetric development can only be measured this way. Therefore others (Roshko and Skeide et al.) do not report/highlight this phenomenon separately [37][24][28].

2.2.4. Supercritical Flow

The supercritical flow regime lower bound corresponds with the Reynolds number at which the laminar separation bubble disappears and the boundary layer on the cylinder transitions to turbulent without laminar separation as seen in Figure 2.10. Zdravkovich terms this regime TrBL3 (transition within boundary layer 3).

2.2.5. Transcritical Flow

Transcritical flow refers to the regime where the flow over the cylinder is already turbulent at the leading stagnation point of the cylinder. This occurs at high Reynolds numbers and is characterised by a fully turbulent boundary layer and increasingly early turbulent separation. Zdravkovich, in his naming system, terms this regime TrBL4: full turbulence.

It is to be noted that the naming of this regime is greatly contested and varies from publication to publication. The term 'transcritical' was coined by Roshko [24]. Often 'transcritical' and 'supercritical' are interchanged for the meanings in Latin to correspond to their Reynolds number ranges relative to the critical Reynolds number as in work by Szechenyi [30]. Sarpkaya et al. [25] term

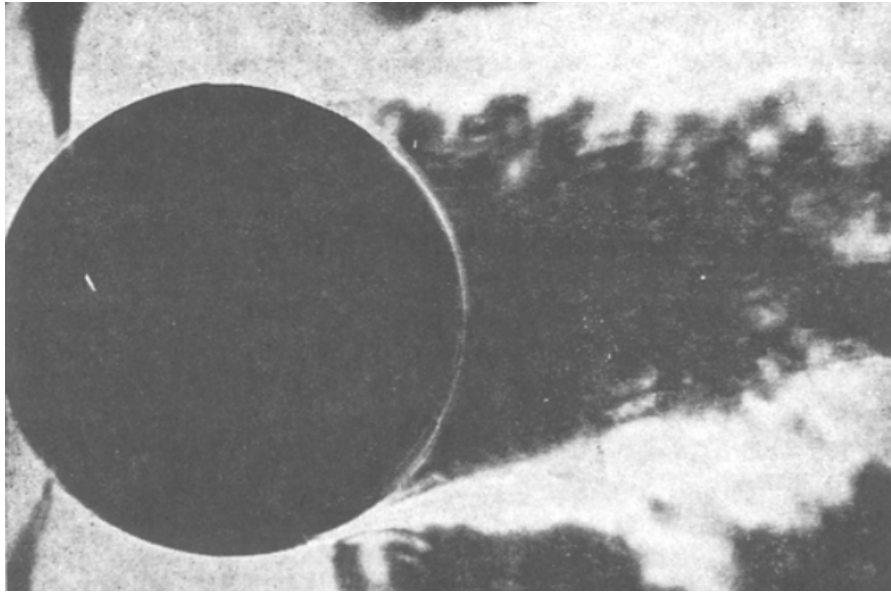
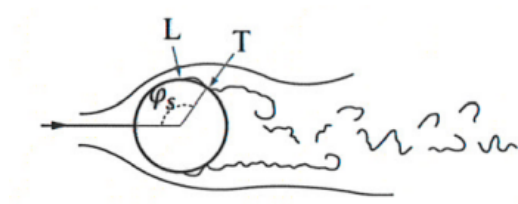
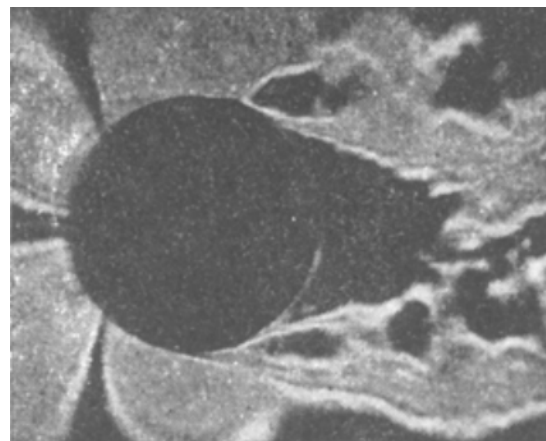


Figure 2.8: Flow visualisation showing one side of with a successful transition and reattachment of flow and the other undergoing laminar separation. As a result, the wake is asymmetrical and there is a large difference in separation location on each side. Since there is a net deflection of the airflow in the positive-y direction, there will be a non-zero sideforce measured in the negative-y direction. Adopted from Bozhkov et al. [5]



(a) Sketch of critical flow around a cylinder. Point 'L' and 'T' mark the location of laminar and turbulent separation respectively. Adopted from van Moll [18].



(b) Flow visualisation of the wake of a cylinder in critical flow. Adopted from Bozhkov et al. [5].

Figure 2.9: A sketch and image of a cylinder in critical flow. The boundary layer transitions to turbulent and the separation is turbulent.

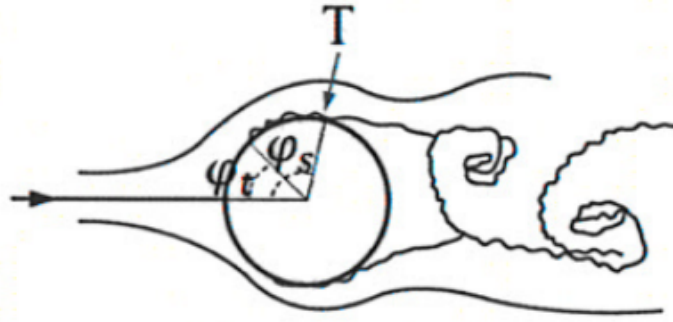


Figure 2.10: Sketch adopted from van Moll [18] of a cylinder in supercritical flow. The boundary layer transitions to turbulent without forming a laminar separation bubble (at the angular location marked ϕ_t).

the regime ‘post-super-critical’ [37]. While it is important to acknowledge the variance in reported names for this regime, consistency in naming is important. In this research, the term ‘transcritical’ coined by Zdravkovich will be used to refer to this regime.

2.2.6. Regime of Interest

Based on the flow differences between the regimes presented in Section 2.2.1 through Section 2.2.5, it is noted that depending on the regime, the flow can have largely varying characteristics. This is exemplified by the drag coefficient (C_d) measured as a function of Reynolds number by Roshko [24] and Wieselbergers [35] presented in Figure 2.11. The drag coefficient of a cylinder is defined as shown in Equation 2.2 [24]. The area $l \cdot D$ used to normalise the force is the frontal projected area of the cylinder. The high drag in the viscous regime, the plateau in the subcritical regime, the drag crisis triggered at Re_{crit} and the subsequent slow (supercritical) and then rapid (transcritical) drag rise is seen in the plot. It is therefore important to ascertain which regime is of interest.

$$C_d = \frac{F_D}{\frac{1}{2}\rho U_\infty^2 D l} \quad (2.2)$$

Consulting the work of Timmer and Veldhuis, the typical range of Reynolds numbers experienced at the calf and ankles of speed-skaters are obtained [33]. These figures are presented in Table 2.3. These values are based on an analysis that considers only the average speed of a skater with added and subtracted relative limb velocity during a skater’s motion. Based upon this, the regime of interest is defined as $0.6 \cdot 10^5 < Re < 1.18 \cdot 10^5$.

Table 2.3: Ranges of Reynolds numbers experienced at the ankle and calf of male speed-skaters based on the average speed of world record times in December 1997. Adapted from Timmer and Veldhuis [33].

Leg Location	Distance (m)	Re_{av}	$\pm \Delta Re$	$\pm \Delta Re$ (%)
Calf	1500	$1.18 \cdot 10^5$	$0.22 \cdot 10^5$	19
Ankle	1500	$0.65 \cdot 10^5$	$0.19 \cdot 10^5$	29
Calf	5000	$1.09 \cdot 10^5$	$0.22 \cdot 10^5$	20
Ankle	5000	$0.60 \cdot 10^5$	$0.19 \cdot 10^5$	31

Drag in the Regime of Interest

The drag coefficient presented in Figure 2.11 is presented again in Figure 2.12 with an added annotation of the regime of interest. The regime of interest lies fully in the subcritical region where the coefficient of drag is nearly constant just above a value of 1.2. The critical flow regime lies at a

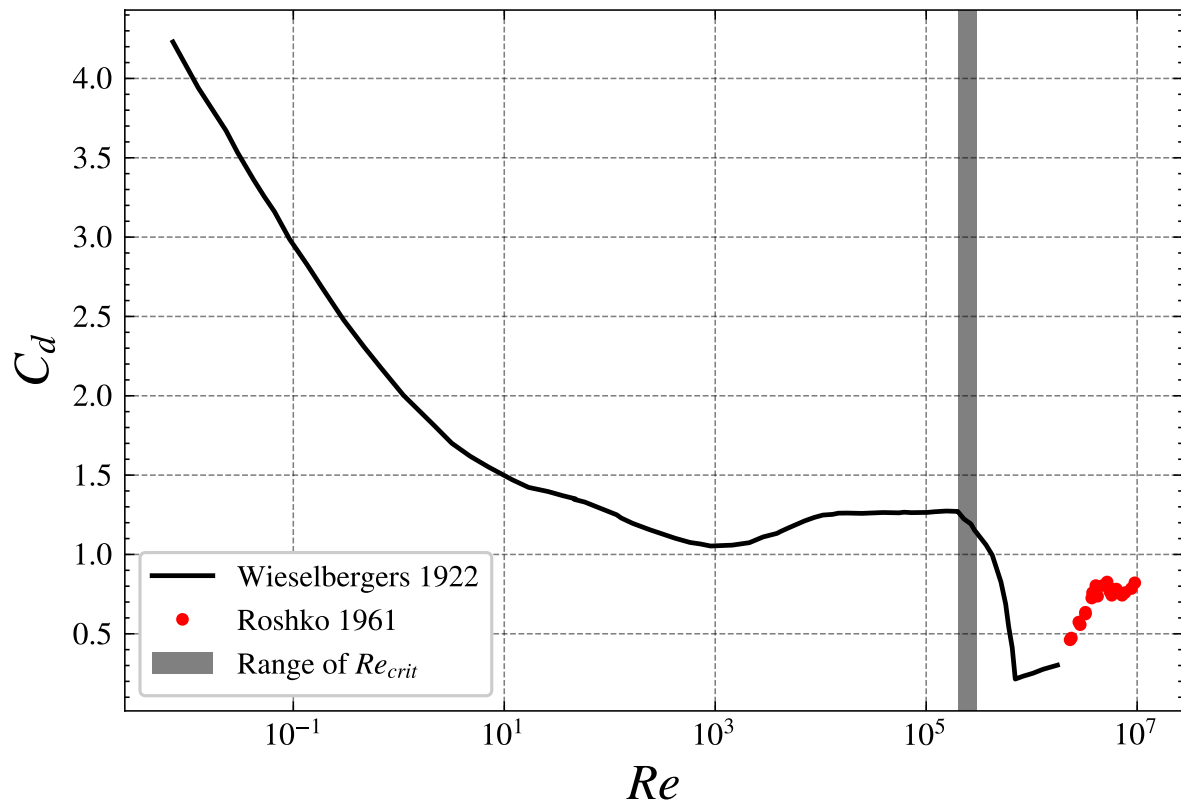


Figure 2.11: Cylinder drag coefficient plotted against Reynolds number [24] [35].

range of Reynolds numbers that is greater than the regime of interest by about 10^5 . This indicates that if the drag crisis can be triggered at a value that lies within or just before the regime of interest, the drag in the regime can be drastically reduced. More details regarding this are presented in Section 2.3

Proportion of Friction Drag

Dividing the total drag on a cylinder into its viscous (frictional) and pressure components is useful in order to find the component with the greatest potential for reduction. Consulting the work of Achenbach [1] and Thom [32], it is found that the friction drag makes up a proportion of the total drag of less than 3% in any of the relevant regimes. This is plotted in Figure 2.13 where the friction drag was calculated by subtracting the pressure drag obtained from the measured pressure coefficient from the total balance-measured drag. In the regime of interest especially, the friction drag represents less than about 2% of the total drag. Naturally, this leads to the conclusion that pressure drag presents the greatest proportion of the drag of a cylinder especially in the regime of interest.

Role of Pressure Distribution

Since the pressure drag makes up the majority of the drag by far, it is important to understand how the pressure distribution changes from regime to regime. For this the coefficient of pressure (C_p) is used and its formulation is presented in Equation (2.3). In the potential solution of cylinder flow, the pressure distribution about the cylinder is expressed as shown in Equation (2.4) as a function of ϕ [2].

$$C_p = \frac{p - p_\infty}{\frac{1}{2}\rho U_\infty^2} \quad (2.3)$$

$$(C_p)_{potential} = 1 - 4 * \sin^2(\phi) \quad (2.4)$$

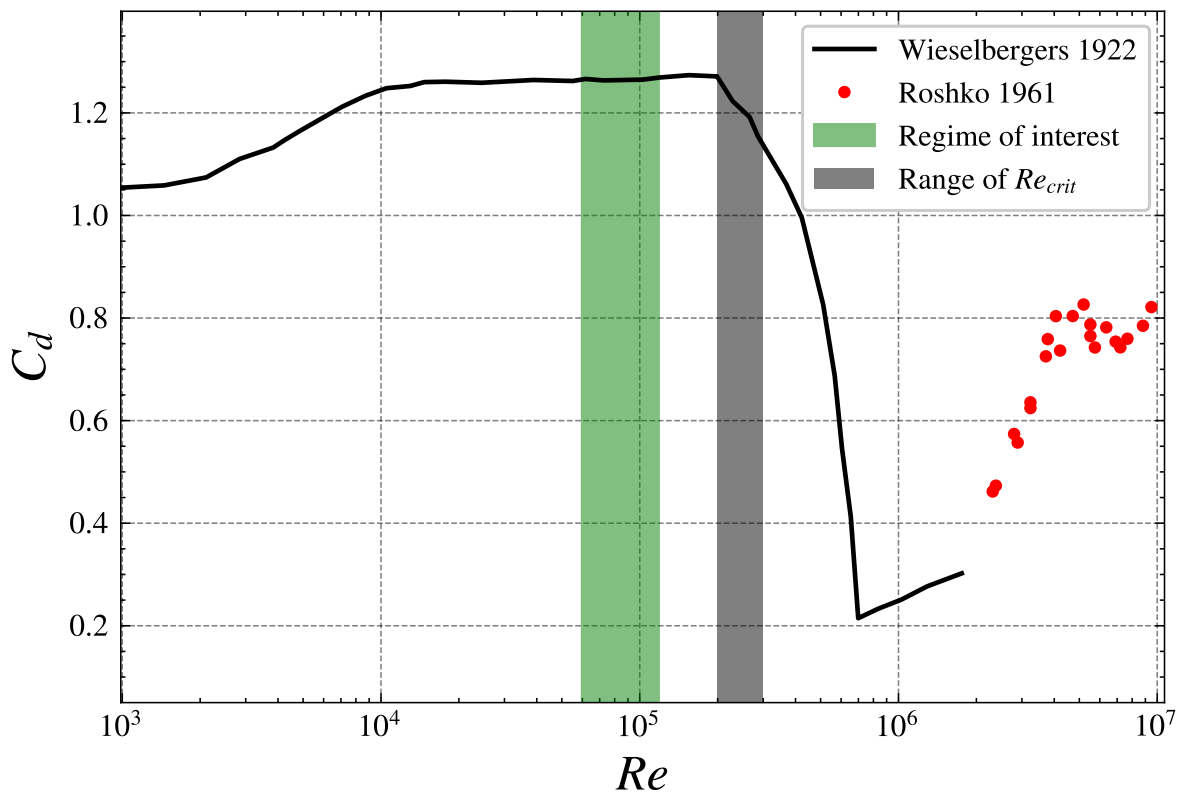


Figure 2.12: The drag coefficient varying with Reynolds number around the regime of interest.

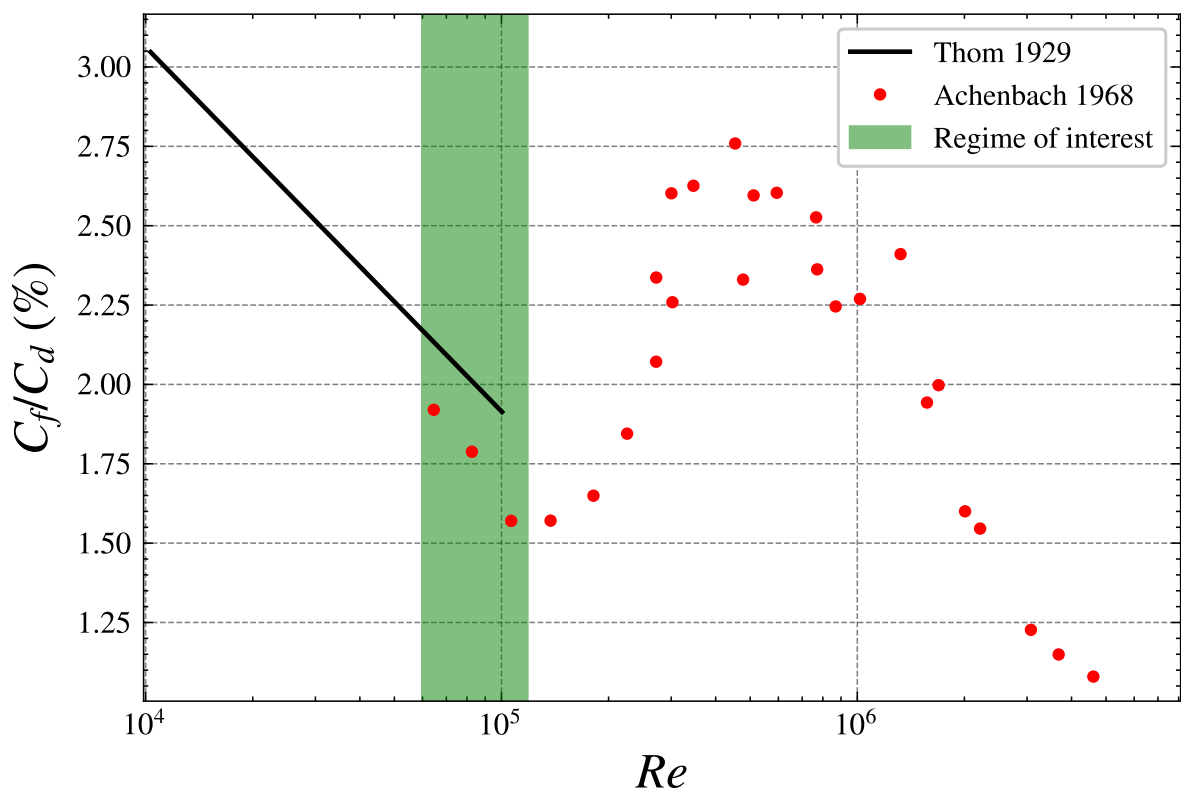


Figure 2.13: The friction drag expressed as a proportion of total drag over a range of Reynolds numbers [32] [1].

Distributions of the pressure coefficient about a cylinder are presented in Figure 2.14. Firstly, it is seen that all three experimentally obtained traces differ from the potential solution due to the lack of consideration of viscosity and boundary layer formation in the potential solution. Therefore, the suction peak is also much greater (more negative value for C_p) in the theoretical case. The experimental traces follow each other closely and rapidly veer off where the boundary layer nears separation. Furthermore, in the critical flow plot, the laminar separation bubble is seen at about $\phi = 100^\circ$. Flow separation is seen at 80° , 110° and 125° for the subcritical, critical and supercritical flow respectively. The pressure remains constant after separation. This value is termed the base pressure coefficient ($C_{p,b}$), and this is the pressure that the surface of the cylinder experiences after separation.

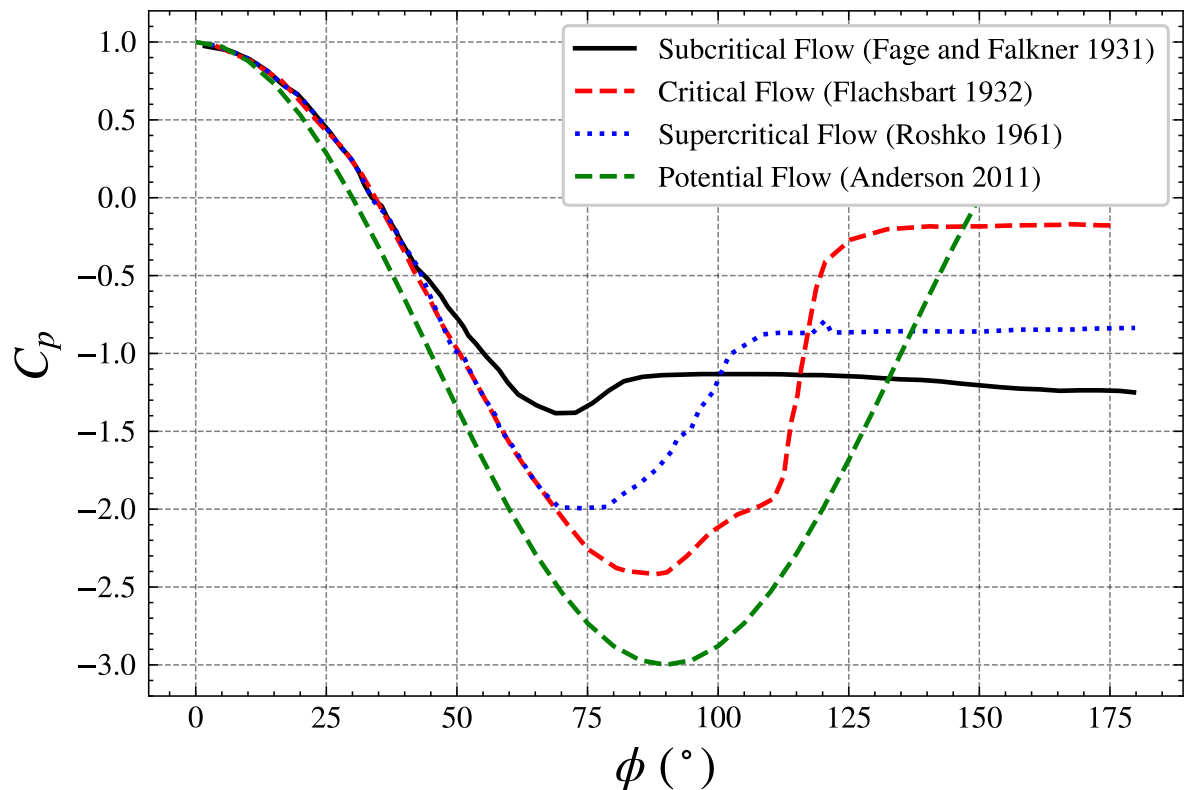


Figure 2.14: Pressure distribution about a cylinder in the subcritical ($Re = 1.1 \cdot 10^5$), critical ($Re = 6.7 \cdot 10^5$), supercritical ($Re = 8.5 \cdot 10^6$) flow regimes [12][13][24]. The potential flow solution is also presented here for reference.[2]

In the potential flow distribution, the pressure on the leeward side of the cylinder ($\phi > 90^\circ$) sees a pressure recovery where the value of C_p rises back to the stagnation value of 1. If the flow separates, the pressure does not fully recover and the net resisting force on the cylinder due to this lower base pressure value is the pressure drag. Therefore, the greater the base pressure coefficient the lower the pressure drag. Figure 2.15 shows the base pressure coefficient as it varies with the Reynolds number. The drag crisis is also seen here as a rapid drop in the *negative* base pressure coefficient. The fact that this $\sim 90\%$ drop in negative base pressure coincides with the $\sim 80\%$ drop in drag coefficient further reinforces the fact that the drag crisis is a pressure driven phenomenon. The transition to turbulence does indeed cause an increased friction drag due to the greater near-wall velocity gradient but this increase is negligible in comparison with the large drop in pressure drag.

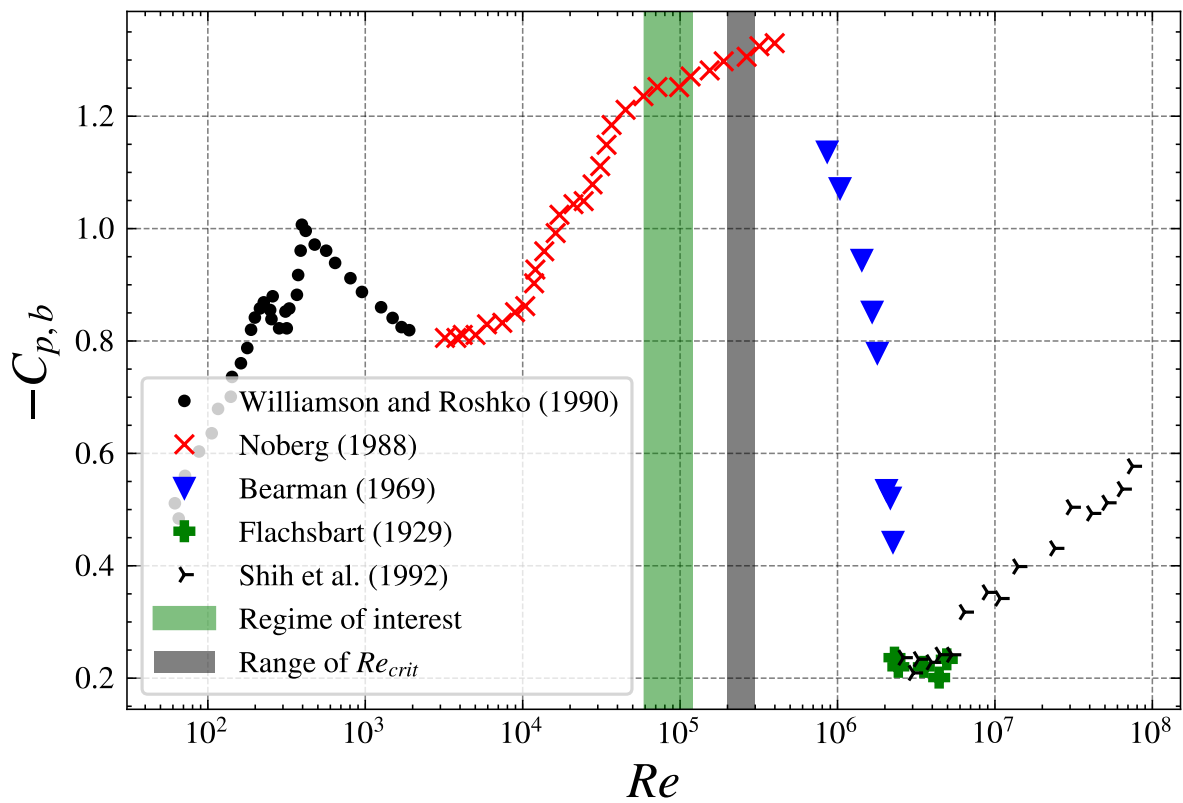


Figure 2.15: The negative pressure coefficient obtained experimentally and plotted against Reynolds number [12] [13] [24].

2.3. Approaches to Drag Reduction

In order to reduce the drag on a cylinder, based on conclusions drawn in the preceding section, the aim should be to reduce the pressure drag. To be specific, the mechanism of a 'natural' drag crisis should be emulated at the desired Reynolds number. This is shown in Figure 2.16 in the form of 'affecting the flow'. This is divided further into actively and passively affecting the flow. Active flow control is not considered due to its impracticality in application to skin-suits.

In order to emulate a drag crisis in the flow, the turbulent transition in the boundary layer needs to artificially take place. To this end, the flow is *tripped* in order to energise the boundary layer, delay separation, reduce wake width and increase the base pressure. This leads to a reduction in drag. As seen in Figure 2.16, the two applicable ways to trip the flow are discrete and distributed roughness. This research looks into discrete roughness, namely cylinders of constant diameter protruding out of the surface. These elements will also be referred to as polka-dots. Additionally, as indicated in the diagram, the research will not consider directional effects on the cylinder drag due to polka-dot induced drag reduction.

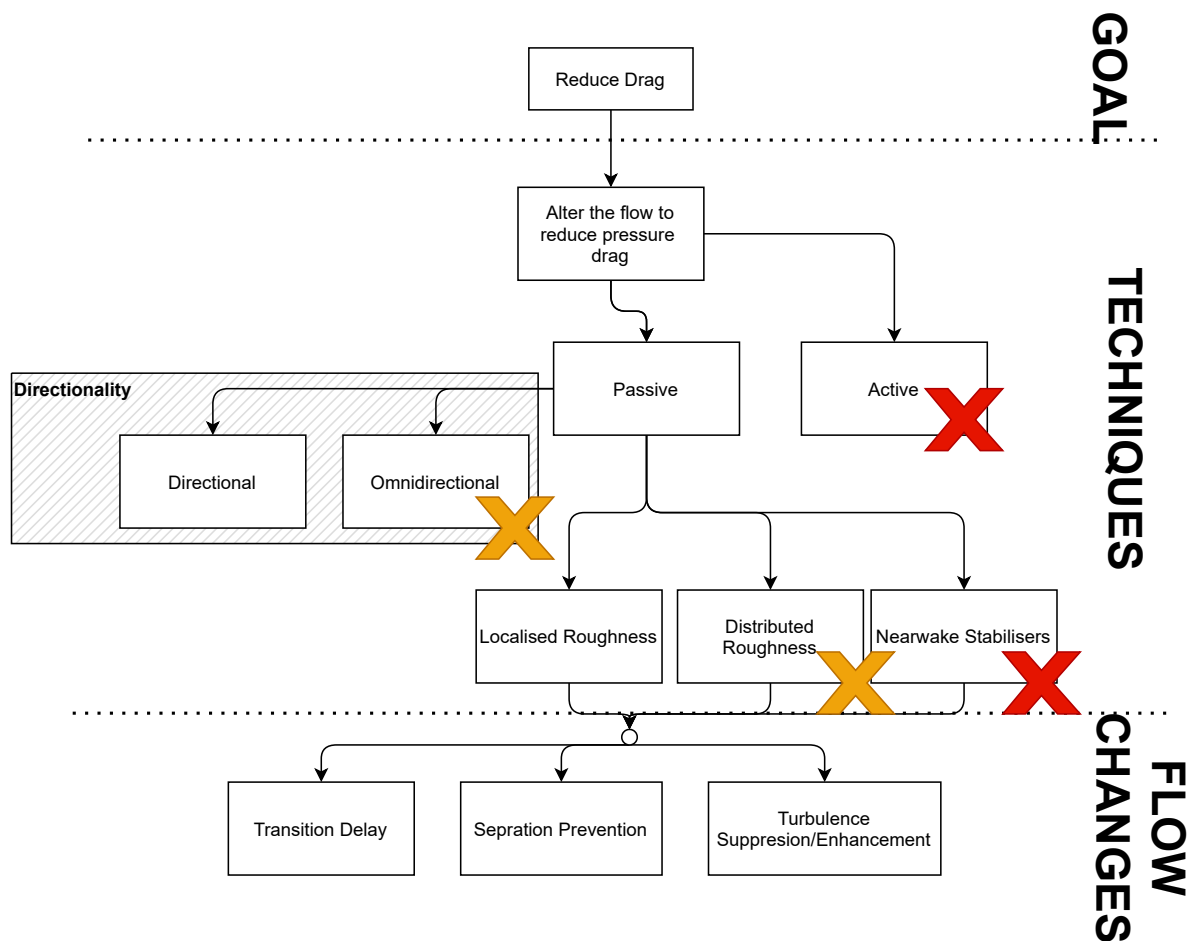


Figure 2.16: Flowchart highlighting the techniques used for and the consequential flow changes that arise from reducing the drag of a cylinder. The red crosses signify branches that are impractical or impossible for implementation on skin-suits and the yellow crosses signify the branches that are not considered in this research.

2.3.1. Tripping Mechanism and Its Effect

The goal of tripping the flow is to introduce energy into the boundary layer close to the wall such that it is more resistant to strong adverse pressure gradients. This is usually done by introducing disturbances to the flow to an extent that the inherent viscosity of the flow cannot dampen them. As explained with the use of Figure 2.16, discrete roughness elements will be considered in this research. A few examples of discrete roughness elements are presented in Figure 2.17. This research delves into 'cylindrical vortex generators' and the dimensions and configurations considered are explained in detail in Chapter 4.

The selection of discrete roughness elements is crucial as they directly influence the transition process. By strategically placing these roughness elements, specific flow patterns can be induced. This allows for controlled disruption of the laminar flow, initiating the transition to turbulence. The examples shown in Figure 2.17 demonstrate different configurations that have been employed in previous studies to trip the flow.

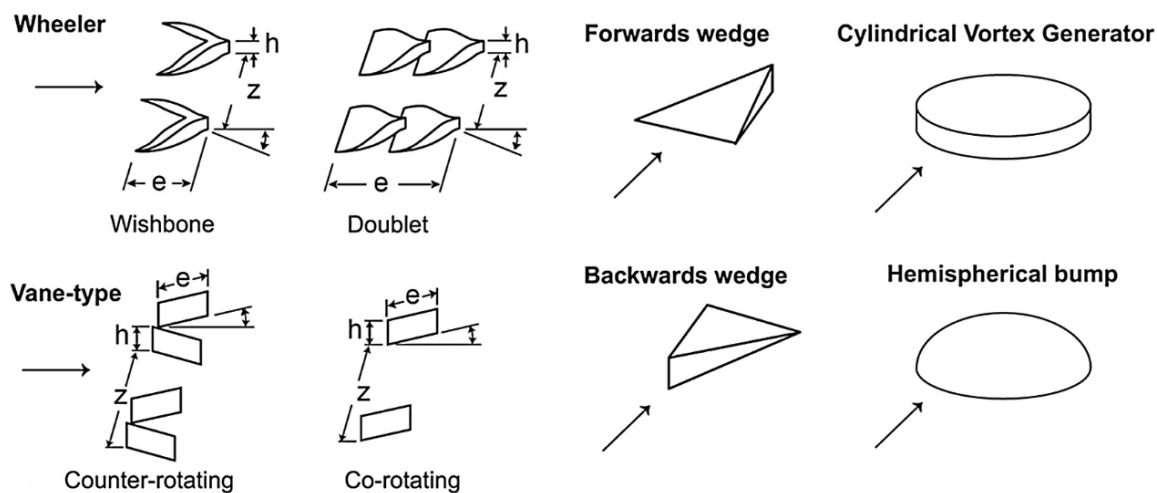


Figure 2.17: Examples of discrete roughness elements to trip the flow adopted from Demartino and Ricciardelli.[10]

Figure 2.18 presents the DNS solution of a flow that is tripped using the element shown in the bottom left of the image. The tripping process is divided into four different stages:

- **Stage one** involves the propagation of vorticity in the three directions due to the velocity deficit behind the roughness element.
- **Stage two** involves the spanwise (z -oriented) vortices twisting to form horseshoes with downstream pointing legs.
- **Stage three** involves the stretching (increased helicity) of the horseshoe-shaped vortices in the flow direction.
- Finally, **stage four** involves the generation of turbulent wedges which then grow to engulf the flow of the whole channel in turbulent flow.

It is worthy to note that while Figure 2.18 presents all the stages of the transition to turbulence, it might not be that case that the flow must reach stage IV for the separation to be delayed. It is theoretically possible that a streamwise vortex is able to introduce enough energy into the flow and prevent the boundary layer from separating.

The effect of tripping the flow from laminar to turbulent is that the drag crisis is triggered at a lower Reynolds number. This new Reynolds number is now the Re_{crit} and the minimum achieved drag coefficient is termed $C_{d,min}$. It is expected that the $C_{d,min}$ in a configuration with tripping elements is greater than that of a bare cylinder. This is due to the fact that in the drag crisis of a smooth

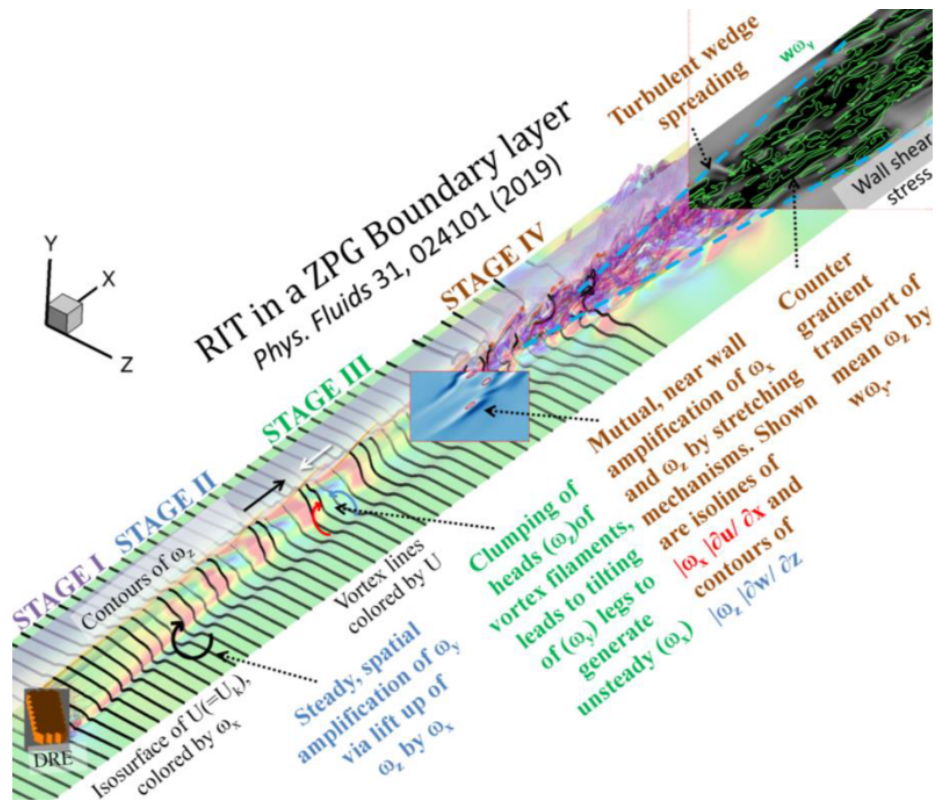


Figure 2.18: The mechanisms in the four stages of roughness induced transition visualised through a DNS carried out by Suryanarayanan et al.[29]

cylinder, the flow reaches turbulence only when the laminar boundary layer naturally reaches an instability. On the other hand, in the roughness induced drag crisis, a larger proportion of the cylinder surface sees turbulent flow. Given the fact that turbulent flow corresponds to a greater surface shear, the cylinder with a roughness induced drag crisis will have greater friction drag and therefore a greater value for $C_{d,min}$ [8]. Additionally, the lower the Re_{crit} , the greater the value of $C_{d,min}$. Therefore, the design of an effective tripping configuration leads to a requiring a balance between minimising the $C_{d,min}$ while having an apt value for Re_{crit} given the regime of operation.

2.3.2. Tripping Potential of an Element

To measure the tripping potential of a certain roughness element, the *roughness height based Reynolds number* is used. Its formulation is presented in Equation (2.5) where where k is the height of the roughness element, u_k is the flow velocity at height k from the wall, and ν is the canonically defined kinematic fluid viscosity.

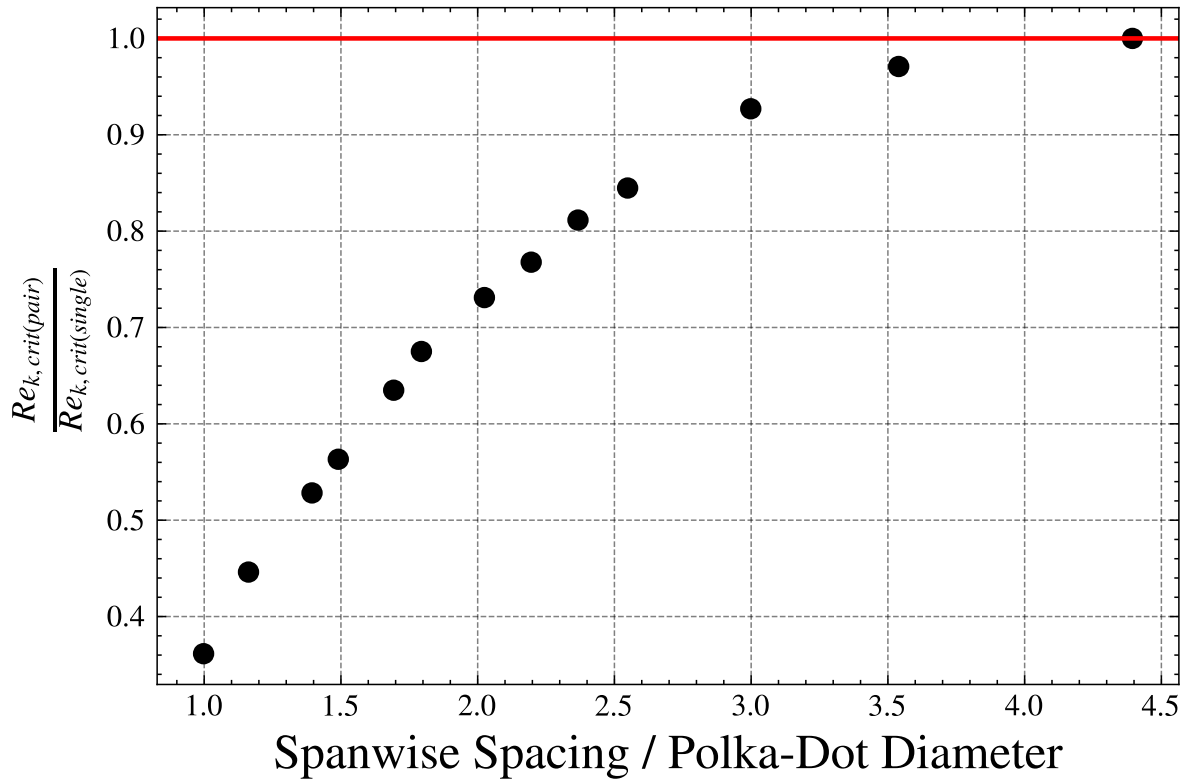
$Re_{k,crit}$ or the *critical roughness height based Reynolds number* is the minimum value of Re_k for which the polka dot induces turbulence in the flow. Below this value of Re_k , at this scale of the flow, the viscosity overpowers the induced undulations and acts to smooth out the disturbances in the flow. In general, it is seen that for a given width, a taller polka-dot has a greater $Re_{k,crit}$ [34]. This does not necessarily mean that a shorter and wider polka dot is more effective since firstly the height is a part of the formulation for Re_k and at a lower height in the boundary layer, the value of u_k is also smaller. For a discrete roughness element with aspect ratio 1, von Doenhoff and Braslow [34] measured the value of $Re_{k,crit}$ to be in the range of 600-900. Furthermore, for a zigzag strip of thickness 0.35 mm, the value is predicted to be 200 by van Rooij and Timmer [23]

$$Re_k = \frac{k \cdot u_k}{\nu} \quad (2.5)$$

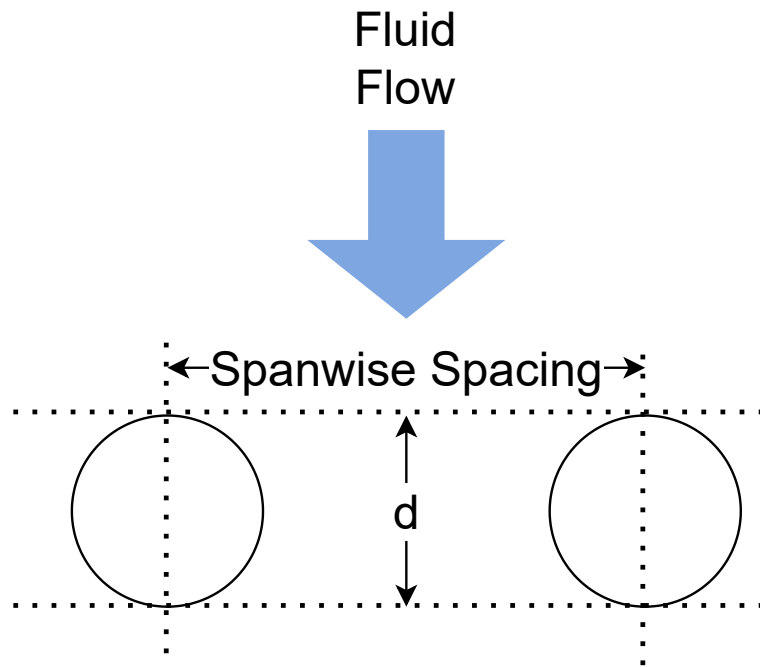
While the same trend of $Re_{k, \text{crit}}$ with polka dot geometry is seen in differing pressure gradients, the same cannot be said about the evolution of the polka-dot wake in the boundary layer. Based on the DNS of Suryanarayanan et al., it is seen that a pressure gradient has an influential impact on the development of turbulence. In general, an adverse pressure gradient amplifies the stages of turbulence growth as the artificial tripping combines with the pressure-gradient-driven boundary layer growth, while a favourable pressure gradient slows it down and can even arrest tripping altogether [29]. This is especially of note since cylinders see steep pressure gradients as seen in Figure 2.14.

Another point of note is the effect that tripping elements have on each other. This research will consider tripping elements that are placed in spanwise arrays placed along the cylinder surface longitudinally, i.e., their arrangement is normal to the flow. An experimental analysis carried out by von Doenhoff and Braslow.[34] showed that a pair of elements that is placed less than 4 diameters apart (measured from the center of the polka-dots) should have a lower $Re_{k, \text{crit}}$ than a single one of those elements. These results are summarised in Figure 2.19.

It should be noted that these results may not be directly applicable to this research. Firstly, this analysis involves no pressure gradient since it looks at tripping over a flat plate. Secondly, this tripping array only consists of two elements, such that each of the elements only has one complementing element on one side. Having elements on each side might affect the tripping differently.



(a) Experimental results showing the change in $Re_{k,crit}$ with specific spacing.



(b) The measurement used in this report and by von Doenhoff and Braslow. of the spanwise spacing of the polka-dots.

Figure 2.19: The experimental study carried out by von Doenhoff and Braslow regarding the effect of spanwise spacing on tripping potential.

2.4. Research Questions

Prior to any experimental work, an extensive literature study was carried out. This chapter served as a summary of this survey and presents the most relevant findings. As a result of the survey, a number of gaps in literature were identified which resulted in the formulation of the research questions that governed the design of the experimental campaign. This section presents both the gaps identified and the research questions formulated.

Gaps in Literature

- Limited information on boundary layer height and profile distribution of cylinder flows.
- Few findings that characterise values of $Re_{k,crit}$ for different roughness shapes.
- Dearth of information regarding mutual effects of roughness elements (spanwise spacing).
- Few studies assessing the effect of a pressure gradient on flow tripping.

Research Questions

Based upon the gaps identified in literature and the knowledge gained from literature, the main overarching research question is identified:

What is the effect of polka-dot shaped surface roughness elements on the boundary layer, wake flow and drag characteristics of a circular cylinder within the operation regime of an ice-skater's limb?

The following sub-questions are considered:

- What is the effect of the **polka-dot height** on the boundary layer flow, wake flow and drag?
- What is the effect of the **polka-dot width** for a given height on the boundary layer flow, wake flow and drag?
- What is the effect of the **polka-dot spanwise spacing** on the boundary layer flow, wake flow and drag?
- Is there a correlation between the wake width, the total drag, the boundary layer integral quantities and polka-dot geometry?

3

Particle Image Velocimetry

Particle Image Velocimetry (PIV) is an experimental technique used in aerodynamic analysis in order to resolve the velocity field of a domain. Its operation is based on recording the motion of tracer particles in a flow. The process involves capturing images at two different times and thereafter using a statistical approach to calculate the velocity field within the captured regime.

PIV is used in this experimental campaign since it is a non-intrusive and whole-field technique as highlighted by Raffel et al. [20] Furthermore, it allows for both qualitative flow-field analysis based on the visualisation of the velocity field and quantitative analysis based on derived quantities from the obtained velocity field.

The working principle of PIV is presented in Section 3.1, including an overview of a typical setup and the processing fundamentals. Then Section 3.2 presents the two velocimetry processing techniques used in this research. This chapter only serves as an introduction to the measurement technique, specific details about the experimental setup used in this research are presented in Section 4.4.

3.1. Principles of PIV Measurement

PIV is used to estimate the velocity field in the measurement plane through the suspension of seeding particles in the flow, a typical setup is shown in Figure 3.1. These particles are introduced to the flow at a location where the flow is not disturbed. Their density and size is such that they do not affect the flow and that their movement follows that of the flow itself. It is of note that the process highlighted here only allows for the measurement of velocities within the illuminated plane. If particles have out-of-plane velocities and get captured in both of the images, their velocity is projected onto the measurement plane. This should be kept in mind when analysing these results. While it is possible to measure out-of-plane velocities by the use of multiple cameras (stereoscopic PIV) or three dimensional velocimetry in a volumetric region (tomographic PIV), these techniques are not used in this research and the results obtained from planar PIV provide satisfactory insight into the flow features for this research.

Another way to characterise the velocity in a volume is shown in Figure 3.2 as used by Brown [6]. Here, the location of the laser sheet is adjustable. This allows one to make 'quasi-3D' measurements by making 2D measurements at different positions of the measurement plane.

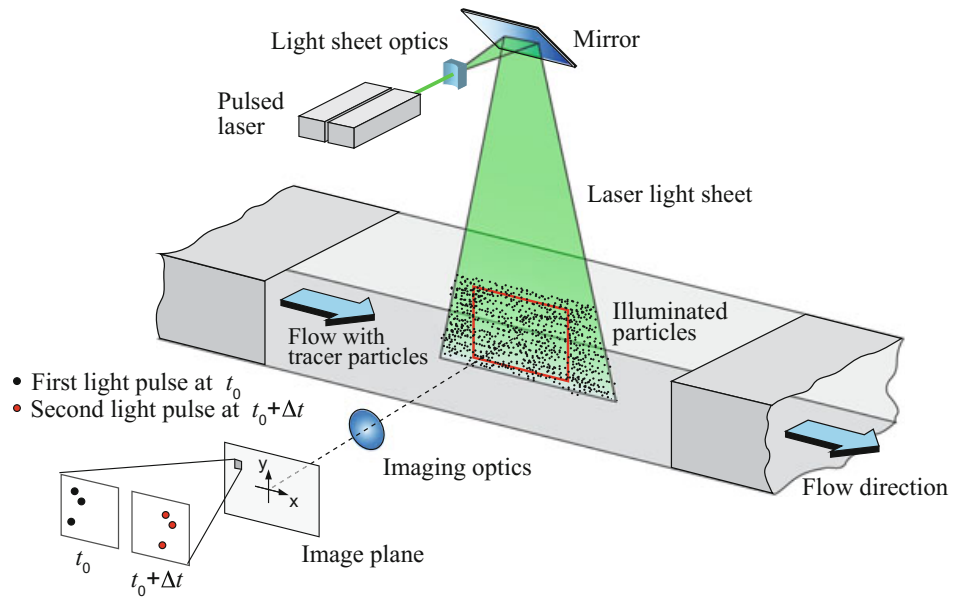


Figure 3.1: A typical PIV setup. Adopted from Raffel et al.[20]

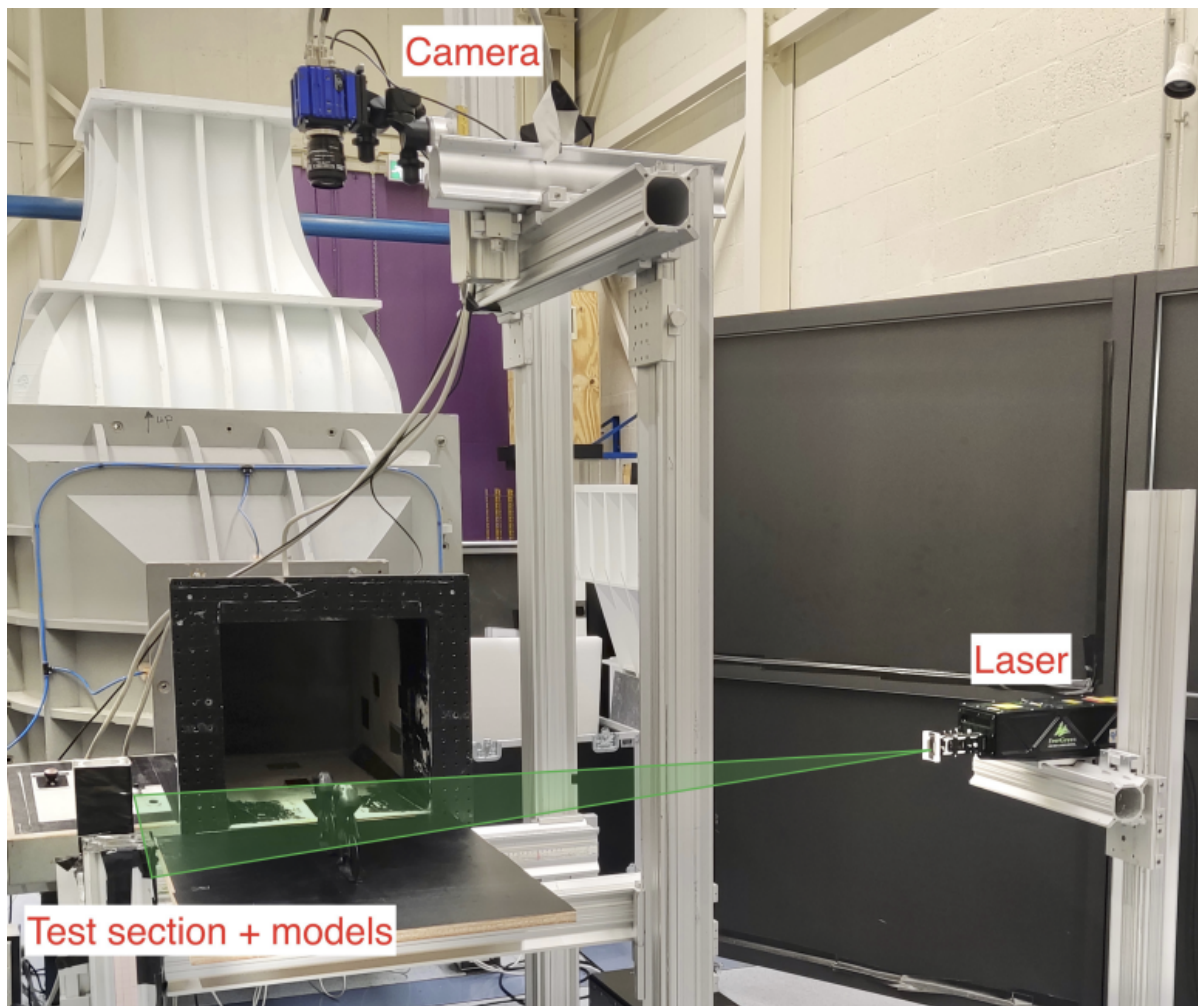


Figure 3.2: The PIV as used by Brown for assessing cyclist wake aerodynamics. Adopted from Brown [6].

The area of interest is illuminated twice with the means of a laser light sheet. The time between the two successive illuminations of the measurement region is dictated by the size of the particles, the velocities, and the imaging optics setup. The images are divided into interrogation windows which are then cross correlated between the two images to determine the displacement of the particles in each window. An example of these interrogation windows is shown in Figure 3.3, the displacement is calculated based on overlaying the window at t_2 on the window at t_1 with different spacial offsets and thereafter calculating the cross correlation. The tracer particle displacement in the interrogation window is then computed from the cross-correlation using a peak-finding algorithm. The velocity is calculated by dividing this displacement vector with the time between the pulses.

In order for the displacement in the images to be mapped to dimensions in the space (number of pixels per millimetre), an image is first taken with an object of known dimension and then the true dimensions are matched with the number of pixels they represent in the images. This calibration process precedes all measurement. This calibration is also repeated after any of the optical setup or the location of the laser sheet moves.

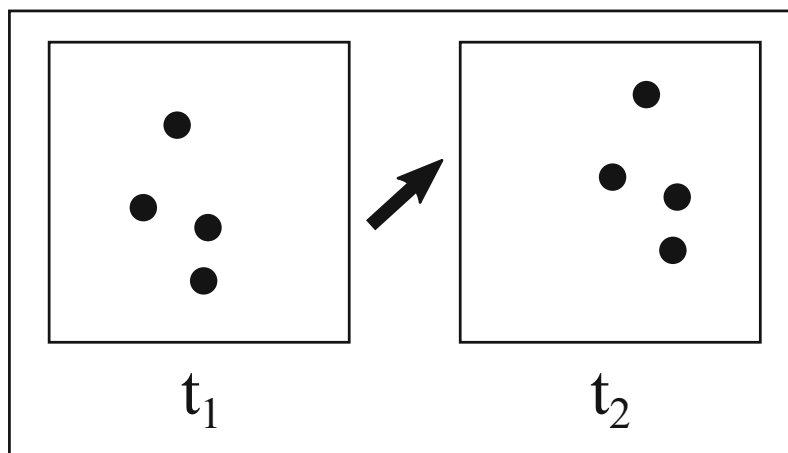


Figure 3.3: An interrogation window shown from two subsequent PIV images. The first frame is captured at time t_1 and the second at time t_2 . The inferred fluid velocity in this window is shown with the arrow in the middle.

3.2. PIV Processing Techniques

In this research, two methods of velocimetry were used. They differ in the order of operations executed in going from the set of image pairs to the final computed velocity field. The order of operation of both the methods is shown in Figure 3.5. The blue blocks represent the image pairs, the yellow blocks represent the calculated cross-correlation field based on the images and the black arrows represent the velocity vectors. The symbols \bar{R} and \bar{V} represent the averaged correlation function and averaged velocity vector respectively.

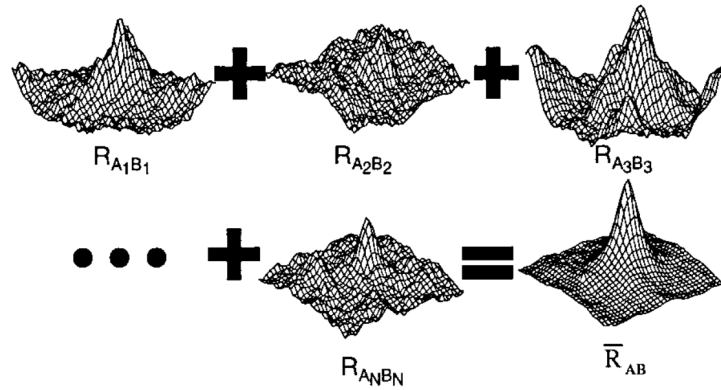


Figure 3.4: A visualisation of the averaging of the correlation as presented by Meinhart et al. [17]

In the **averaged velocity method**, the peak correlation is obtained for each image pair to find the velocity field in each pair as shown in Figure 3.5a. Following this, the ensemble statistics are applied on this image set in order to obtain the mean velocity field. Here, the standard deviation of the velocity field is also obtained through the ensemble statistics.

On the other hand, in the **correlation averaging method**, the correlation of all of the image pairs are summed and averaged as shown in Figure 3.5b. Following this, the velocity field is calculated for the averaged correlation function. Due to the averaging being carried out on the correlation instead of the velocity field, only the mean velocity field is output without the possibility of extracting the velocity fluctuation. The correlation averaging method tends to have a greater signal to noise ratio and fewer outliers. There is usually ‘significant amount of noise’ in the instantaneous correlation functions which is ‘substantially less’ after the averaging of the correlation according to Meinhart et al. who carried out a comparison between the two methods. The averaging of the correlation is shown in Figure 3.4 where the averaged correlation function has a much more pronounced peak in comparison to the ensemble members.

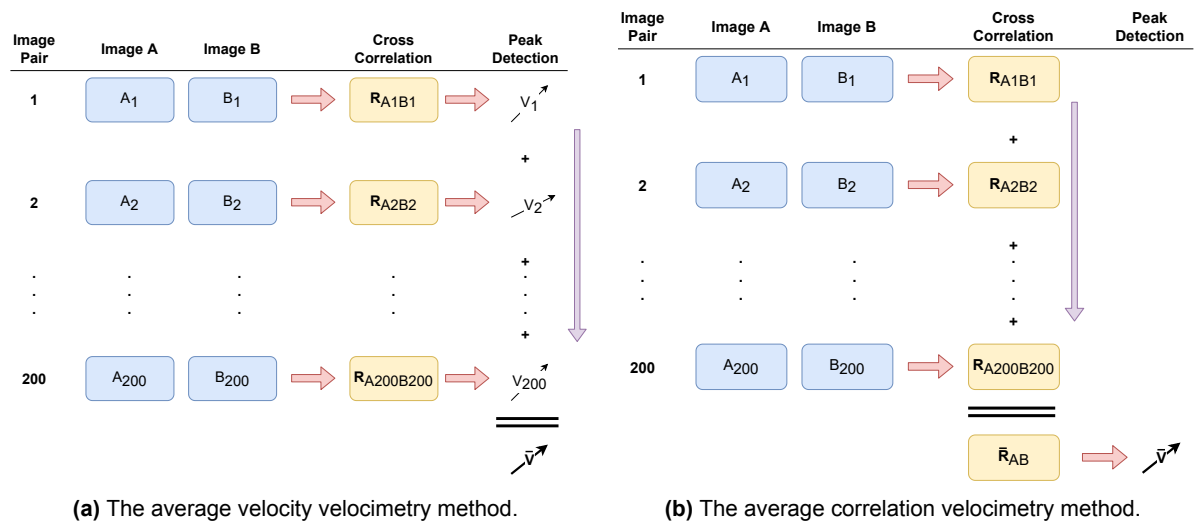


Figure 3.5: A pictorial representation of the order of computation and averaging carried out in the (a) average velocity method and (b) average correlation method. The number of image pairs is shown to be 200 since all PIV runs used an ensemble of 200 image pairs.

Further details of the PIV setup used in this research, and specifics of the processing techniques used are presented in Section 4.4.

4

Experimental Setup

In this chapter, the experimental setup used for conducting the research is described in detail. The experimental setup encompasses various components, including the cylinder models, wind tunnel, balance measurements, Particle Image Velocimetry (PIV) setup, and data reduction techniques. Each component plays a crucial role in the experimental investigation conducted to address the research questions presented in the previous chapter.

First, Section 4.1 presents the dimensions and characteristics of the test models used in the experiments. These cylinder models are designed based on the research questions and objectives established in the preceding chapter. The section provides a comprehensive overview of the various parameters and configurations of the cylinder models, which serve as the focal point for the subsequent experiments.

Following the cylinder models, Section 4.2 discusses the specifications and features of the wind tunnel utilised in the experimental setup. This section outlines the dimensions of the wind tunnel, the airflow characteristics, and the considerations or modifications made to ensure accurate and reliable testing conditions.

Section 4.3 focuses on the measurement apparatus used to quantify the forces acting on the cylinder models. Detailed information regarding the balance setup and data acquisition techniques are presented in this section. These measurements are essential for analysing the aerodynamic behaviour of the cylinder models under different flow conditions.

Moving forward, Section 4.4 describes the Particle Image Velocimetry setup employed to investigate the flow patterns and velocity fields around the cylinder models. This section discusses the PIV technique, the optical arrangement, and the image acquisition parameters necessary to capture the flow characteristics accurately. The obtained velocity field data from the PIV analysis aid in providing insightful analysis regarding the boundary layer and wake flow.

Section 4.5 covers the techniques used to process the collected data. This section is further divided into subsections, namely *Balance Data* and *PIV Data*, which explain the specific methodologies employed for reducing and interpreting the respective datasets. This section takes the reader through the process from obtaining the data from the hardware to the plots and figures presented in Chapter 5.

Overall, this chapter provides a comprehensive overview of the experimental setup, including the cylinder models, wind tunnel, balance measurements, PIV setup, and data reduction techniques. The subsequent chapters will utilise the data obtained from this experimental setup to analyse and interpret the results, ultimately addressing the research questions and objectives.

Table 4.1: Parameters and their symbols used to parameterise the polka-dot configurations.

Symbol	Meaning
k	Polka-dot height
d	Polka-dot diameter
AR	Polka-dot aspect ratio (k/d)
S	Polka-dot (centre-to-centre spanwise) spacing
S/d	Diameter normalised spacing

4.1. Cylinder Models

On the basis of the research questions framed and presented in Section 2.4, 11 roughness configurations were designed for experimental consideration. These cylinders are presented here. First the cylinder geometries are presented in Section 4.1.1. Four different series of cylinders are presented here along with their relation to the research questions. Section 4.1.2 then presents the manufacturing and final product of the cylinder that were used for PIV and force balance measurements.

4.1.1. Cylinder Geometry

The effects of three geometrical parameters are to be considered as mentioned in the research questions. Each of these are assigned to a cylinder series as shown below. The variation in height for a given diameter is represented in two series which correspond to different spanwise spacings. As a result, combinations of configurations from series A & B form series D.

- Polka-dot **height** for a fixed diameter and spacing: Series A (lower spacing) & B (larger spacing)
- Polka-dot **diameter** for a fixed height and fixed ratio of spacing to diameter: Series C
- Polka-dot **spanwise spacing** for a given height and diameter: Series D

For all cylinders a fixed location of $\phi = 60^\circ$ was used to place the roughness arrays. The arrays were placed both clockwise and counter-clockwise from the stagnation point ($\phi = 0^\circ$) such that the cylinders were symmetric with the wind-tunnel centre line. In addition to the cylinders presented above, a cylinder with a zigzag strip applied at $\phi = 60^\circ$ was also used. The thickness of the zigzag strip was 0.93mm with a tip-to-tip spacing of 12mm.

The cylinder diameter was selected on the basis of two rules. The first being: minimising the cylinder size so as to minimise solid blockage in the wind tunnel (smaller is better). The second: maximise the resolution of the boundary layer as captured in the PIV images (for a given optical setup, larger diameter is better). As shown, both these rules drive the cylinder diameter in opposite directions.

A diameter of 9 cm is used in this experimental campaign. According to the solutions to the Prandtl boundary layer equations computed by Zdravkovich, the ratio of boundary layer height to cylinder diameter ($\frac{\delta}{D}$) at $\phi = 60^\circ$ for $Re = 10^5$ is approximately 0.02. Thus, for a cylinder of $D = 9$ cm, $\delta \approx 2$ mm. The symbols used to parameterise the polka-dot configurations are summarised in Table 4.1. The same parameters are shown diagrammatically Figure 4.1, where the polka-dot diameter d , height k and spacing S are marked.

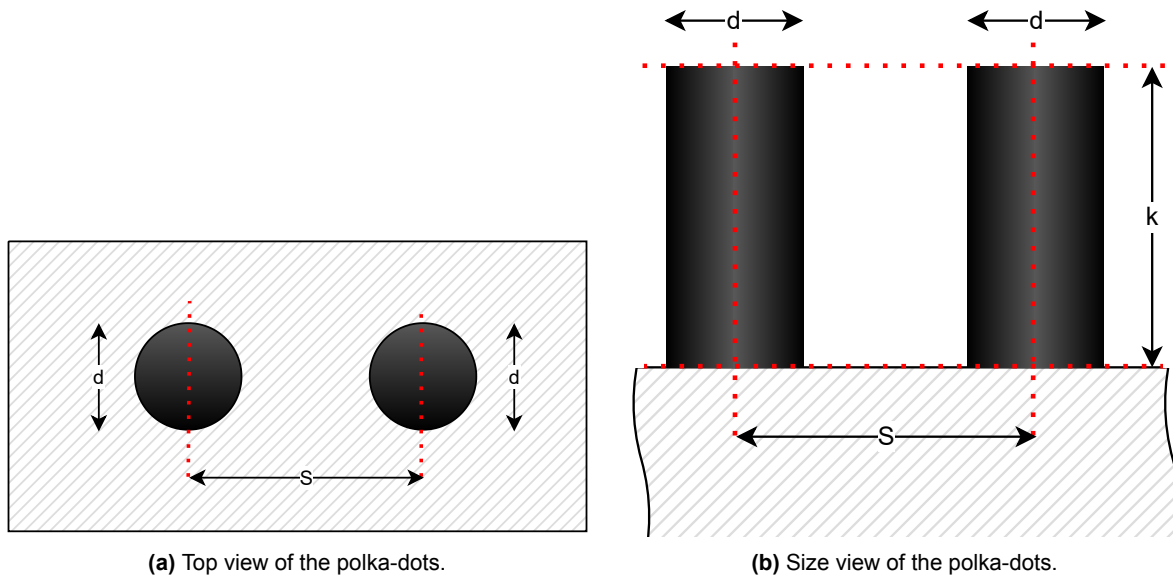


Figure 4.1: An explanation of the polka-dot dimensions d , k , and S . Two polka-dots out of an array are shown here. The hatched area represents the cylinder surface.

Varying Polka-Dot Height

Series A and B are used to measure the effect of the polka-dot height. In both series, the diameter of the polka-dots is kept constant and the values of k are 1, 1.5, 2.2 and 3 mm. The values for S/d for series A and B are 1.5 ($S = 2.25\text{mm}$) and 2.5 ($S = 3.75\text{mm}$) respectively. All configurations from series A and B are presented in Table 4.2.

Based on the Prandtl boundary layer equations, the calculations of Zdravkovich show that the boundary layer at $\phi = 60^\circ$ can vary is approximately 1.8-2.5 mm thick in the regime of interest [37]. As a result, the polka-dot heights are selected such that they vary from being immersed completely in the boundary layer to being larger than the boundary layer depending upon the Reynolds number. More details regarding the Reynolds number range of the experiment are presented in Section 4.2.

Table 4.2: The dimensions of polka-dot configurations in series A and B cylinders where the polka-dot height is varied as signified by the grey column.

Cyl. Nr.	k (mm)	d (mm)	AR	S/d	S (mm)	Series
9	1.5	1.5	1	1.5	2.25	A
10	1	1.5	0.68	1.5	2.25	A
11	2.2	1.5	1.47	1.5	2.25	A
12	3	1.5	2	1.5	2.25	A
2	1.5	1.5	1	2.5	3.75	B
6	1	1.5	0.68	2.5	3.75	B
7	2.2	1.5	1.47	2.5	3.75	B
8	3	1.5	2	2.5	3.75	B

Varying Polka-Dot Diameter

Series C is used to vary the diameter of the polka dots as shown in Table 4.3. The height of the polka dots is kept constant at the baseline value $k = 1.5$ mm. As a result of this, the aspect ratio varies. Since the height is kept constant, the polka dots from all four cylinders should see the same fluid velocity and therefore the same Re_k . As a result, the effect of the shape (AR) is isolated for the same Re_k . The normalised spacing is kept constant to the baseline value of 1.5

based on the findings of von Doenhoff and Braslow that $Re_{k,crit}$ of an array of polka-dots varies with the normalised spacing as presented in Figure 2.19a [34].

Table 4.3: The dimensions of polka-dot configurations in series C cylinders. The column highlighted in grey signifies that within this series, only the diameter (and therefore the aspect ratio too) is varied.

Cyl. Nr.	k (mm)	d (mm)	AR	S/d	S (mm)	Series
9	1.5	1.5	1	1.5	2.25	C
3	1.5	1	1.5	1.5	1.5	C
4	1.5	2.2	0.68	1.5	3.3	C
5	1.5	3	0.5	1.5	4.5	C

Varying Polka-Dot Spacing

Series A & B are identical except the normalised spacing. Together, for the sake of simplicity, they are referred to as series D. The values for the normalised spacing are 1.5 and 2.5 respectively. Based on the findings of von Doenhoff and Braslow, presented in Figure 2.19a, $Re_{k,crit}$ should be 65% lower in series A polka-dot arrays as compared to series B polka-dot arrays. While this does not mean necessarily that the $Re_{k,crit}$ is also proportionally lower for the drag crisis due the non-linearity in the effects of flow tripping on the pressure distribution as presented in Section 2.2, a lower value of $Re_{k,crit}$ was expected to be seen in the drag trace.

Table 4.4: The dimensions of polka-dot configurations in series D cylinders. The pairs of rows highlighted together correspond to the configurations where the individual polka-dots have identical height and aspect ratio such that the only change between them is the spacing as signified by the grey column.

Cyl. Nr.	k (mm)	d (mm)	AR	S/d	S (mm)	Series
2	1.5	1.5	1	2.5	3.75	D
9	1.5	1.5	1	1.5	2.25	D
6	1	1.5	0.7	2.5	3.75	D
10	1	1.5	0.68	1.5	2.25	D
7	2.2	1.5	1.47	2.5	3.75	D
11	2.2	1.5	1.47	1.5	2.25	D
8	3	1.5	2	2.5	3.75	D
12	3	1.5	2	1.5	2.25	D

4.1.2. Manufacturing of Wind Tunnel Models

This subsection presents the materials and methods used for the manufacturing of the cylinders from experimental campaign. In order to minimise the time required to switch between configurations and also to minimise the usage of materials, a single PVC pipe was used as the cylinder and sleeves were manufactured that could slide onto and off the cylinder. The sleeves were manufactured from paper and the corresponding polka-dot patterns were 3D printed upon them.

In order to maximise the quality of the PIV images, the reflection of the light from the laser pulses was minimised. To this end, the use of black paper is necessary. 120 gsm A3 sized photopaper was used on which a plain black layer was applied using a laser printer. The black printed photopaper was also tested to be satisfactory for the subsequent 3D printing.

The two rows of polka-dots were modelled on the paper using a fused filament (FDM) made from *poly(lactic acid)* (PLA). The 3D printing filament was also black in order to minimise the reflection of light during the PIV measurements. As discussed in Section 4.1.1, the location of the polka-dot arrays was fixed at $\phi = \pm 60^\circ$. This comes up to a circumferential distance of 83.78 mm between

the two rows of polka-dots. In order for the ease of manufacturing, this number was rounded to 85 mm. A schematic representation of the printed sheets with the marked dimensions is presented in Figure 4.2. One must note that the spacing is defined centre-to-centre as was in Figure 2.19b.

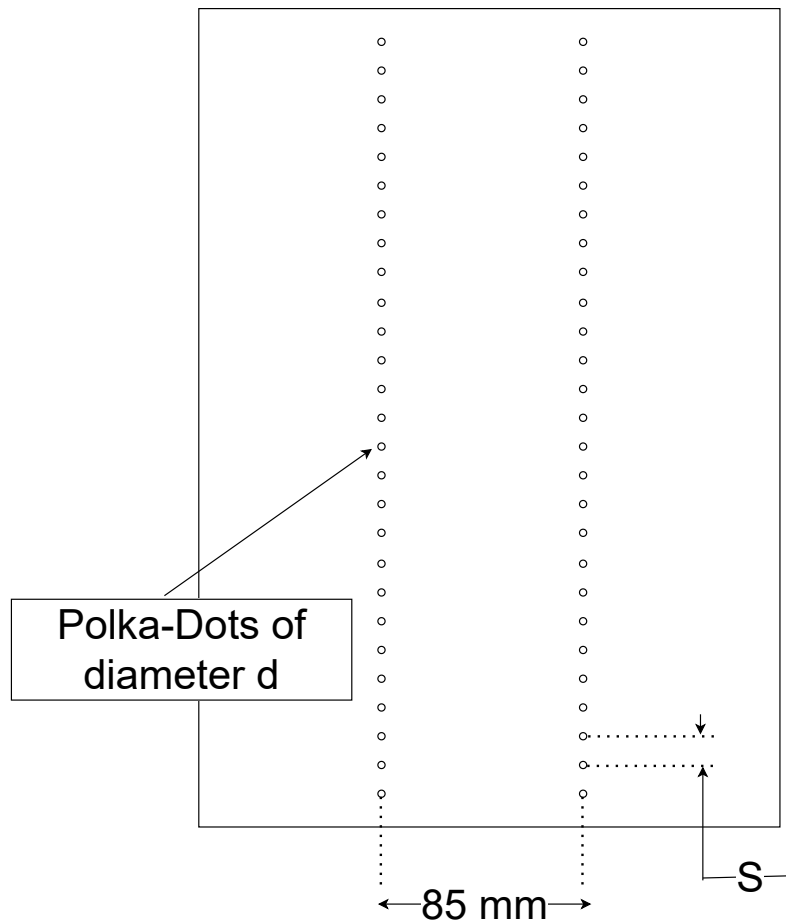


Figure 4.2: A schematic representation of the dimensions of the polka-dot pattern printed on the photo-paper before being wrapped over the cylinders.

Finally, the sleeves are wrapped around the PVC pipe and the loose edges are taped together. These wrapped cylindrical sleeves are shown in Figure 4.3. Care was taken to make sure that the tape and the free edge of the sheet is at an azimuthal position of $\phi > 150^\circ$ such that it is in the base region. It is confirmed by Skeide et al. that the surface characteristics in the base region have no effect on the flow outside the base region [28]. Furthermore, tape and other flow-disturbing artefacts of the fastening were close enough to the surface that they did not interfere with the wake either.



Figure 4.3: The cylinders sleeves after being taped into the a round shape to fit over the PVC pipe base.

4.2. Wind Tunnel

Both the balance measurements and the PIV measurements were carried out at the W-Tunnel at the High Speed Laboratory (HSL) at TU Delft shown in Figure 4.4. It is an open circuit tunnel situated at sea-level that allows different maximum velocities depending upon which tunnel exit is used. For this research, the 40 cm by 40 cm square exit section was used. With this setup, the wind tunnel is capable of reaching exit velocities of up to 30 m/s. Practically, a maximum velocity of 25 m/s was used for the balance measurements and 20 m/s for the PIV measurements due to the strong buffeting seen in the cylinder and balance mounting at greater velocities. The minimum velocity at which measurements were made was 5 m/s due to instability in the flow below this velocity. As a result the Reynolds number range investigated is: $2.5 \cdot 10^4 < Re < 1.26 \cdot 10^5$. This is contextualised in Figure 4.5, where it is seen that the measurement region encompasses the regime of interest (which was identified in Section 2.2.6) completely.

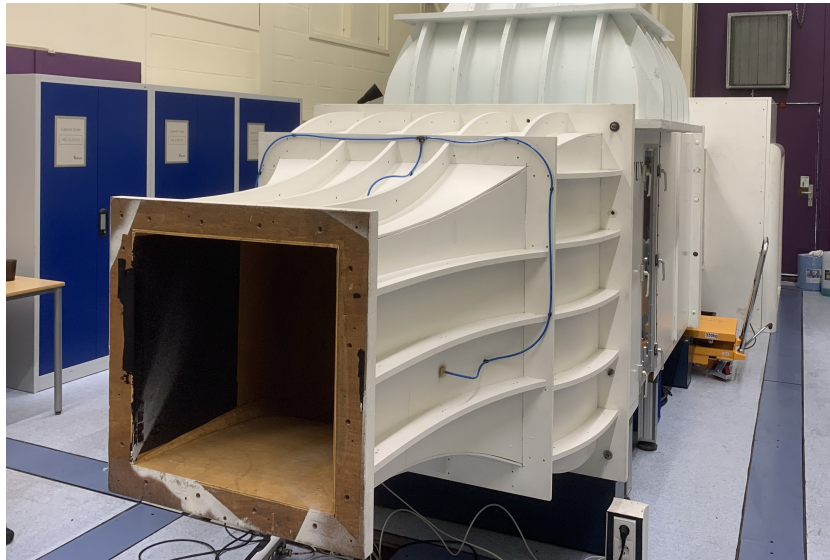


Figure 4.4: The W-Tunnel at the TU Delft HSL.

As is also visualised, in the regime measured, the drag coefficient for a bare cylinder is expected to be effectively constant at a subcritical value above 1.2. This is validated in the balance results presented in Chapter 5.

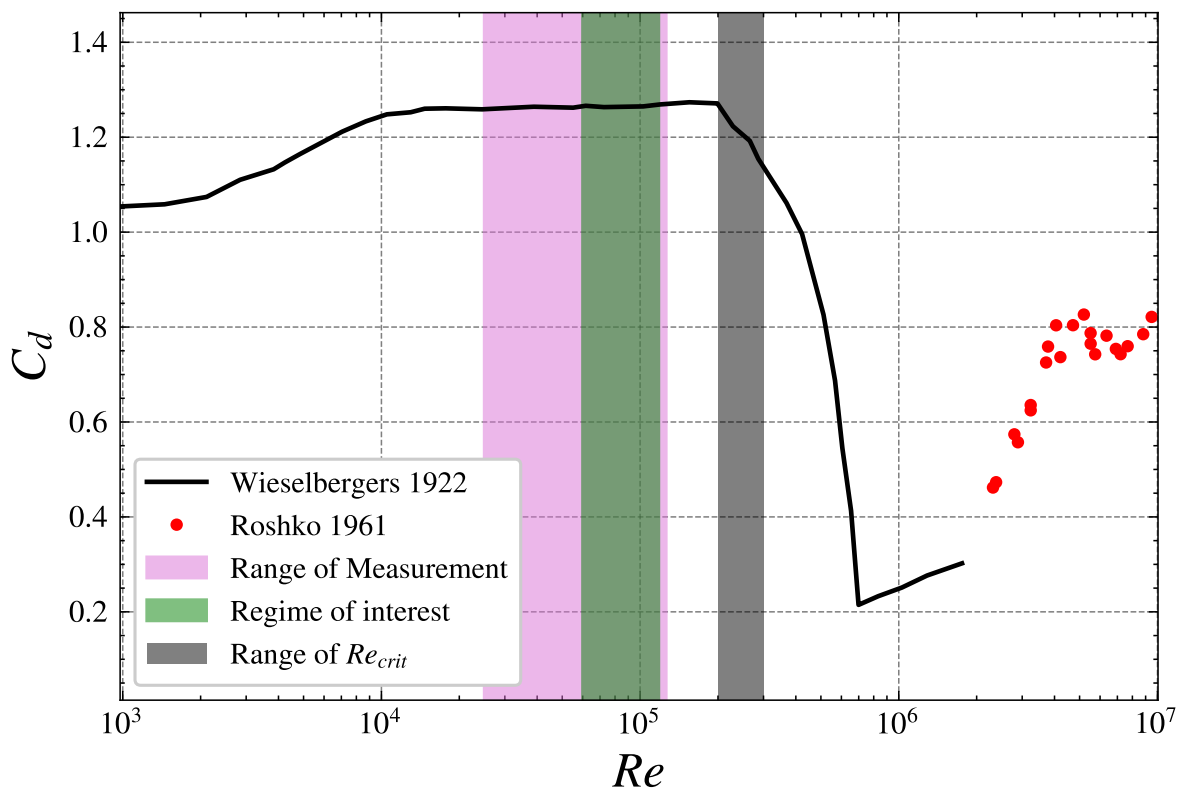


Figure 4.5: The drag curve of a cylinder presented with the regime of interest as shown in Section 2.2.6, and the Reynolds number attained in the experimental campaign.

The wind tunnel was controlled using the tunnel RPM and, among others, the flow velocity in the exit, the flow density and the static pressure were logged.

Blockage Correction

The tunnel was used in the open section configuration. Given that the aforementioned blockage is relatively high at 22.5%, it is of importance to calculate the blockage factor associated with this tunnel and model geometry. The blockage factor ε is a measure of the increase or decrease in actual flow velocity from the free stream velocity due to the jet boundary's effects on the flow. The corrected velocity V_{corr} is calculated using the expression as shown Equation (4.1).

$$V_{corr} = V_{unc}(1 + \varepsilon) \quad (4.1)$$

As a whole the total blockage ε is a sum of the solid body blockage ε_{sb} and the wake blockage ε_{wb} as shown in Equation (4.2). The solid blockage is the blockage caused by the model itself due to the space it takes up causing the streamline to have to bend around it and the wake blockage corrects for the cross-sectional area occupied by the cylinder wake. According to Barlow et al., since the jet is free to expand in an open jet wind tunnel, the blockage effects are 'small but not zero' [3]. More specifically, they define the wake blockage to be negligible. The solid blockage, as shown in Equation (4.3), is actually negative, meaning that the cylinder model being present actually slows down the flow. Here, since the boundary condition at the stream boundary stipulates a 0 pressure gradient rather than a no wall penetration condition, the streamlines are allowed to expand freely. The constant λ_{2D} depends on the fineness ratio of the profile in the tunnel and for a cylinder it takes the value 1 as obtained from Barlow et al. [3] All in all, it is seen that the effective value of the blockage factor is relatively low. Moreover, the blockage factor is independent of velocity since the wake blockage is negligible. All the calculations of Reynolds number and drag coefficient use the corrected velocities based upon this blockage factor.

$$\varepsilon = \varepsilon_{sb} + \varepsilon_{wb} \quad (4.2)$$

$$\varepsilon_{sb} = \frac{\Delta V}{V_{unc}} = -\frac{\pi^2}{24} \lambda_{2D} \frac{t^2}{h^2} \quad (4.3)$$

$$\varepsilon_{sb} = -\frac{\pi^2}{24} \cdot 1 \cdot \frac{9^2}{40^2} \quad (4.4)$$

$$\varepsilon_{sb} = \varepsilon = -0.021 \quad (4.5)$$

$$\varepsilon_{wb} \approx 0 \quad (4.6)$$

4.3. Balance Measurements

One of the measurements made were the measurement of the drag of the cylinder at different Reynolds numbers. These measurements were carried out using a force balance. This section presents the physical details of this setup, the details of the balance, and the methodology of acquisition.

4.3.1. Physical Attachment

A 2-axis force balance was used for the load measurements. The cylinder was securely attached to the force balance using a mounting fixture. The fixture consisted of a rigid support structure made of aluminium, specifically designed to hold the cylinder in place during the experiments. The cylinder was positioned vertically, with its longitudinal axis aligned normal to the ground.

To ensure stability and minimise any unwanted vibrations, the cylinder was carefully aligned and centred within the mounting fixture. The attachment points were securely fastened using appropriate clamping mechanisms, ensuring a firm and rigid connection between the cylinder and the force balance. This setup allowed for accurate measurement of the forces acting on the cylinder during the drag measurement activities.

The PVC pipe which was used as a mount for the sleeves was fixed onto a wooden block which allowed for its attachment to the balance. It was attached to the balance with a frame that positioned the cylinder at the correct height into the flow. Figure 4.6 provides a visual representation of the experimental setup, showcasing the cylinder attached to the force balance using the mounting fixture.

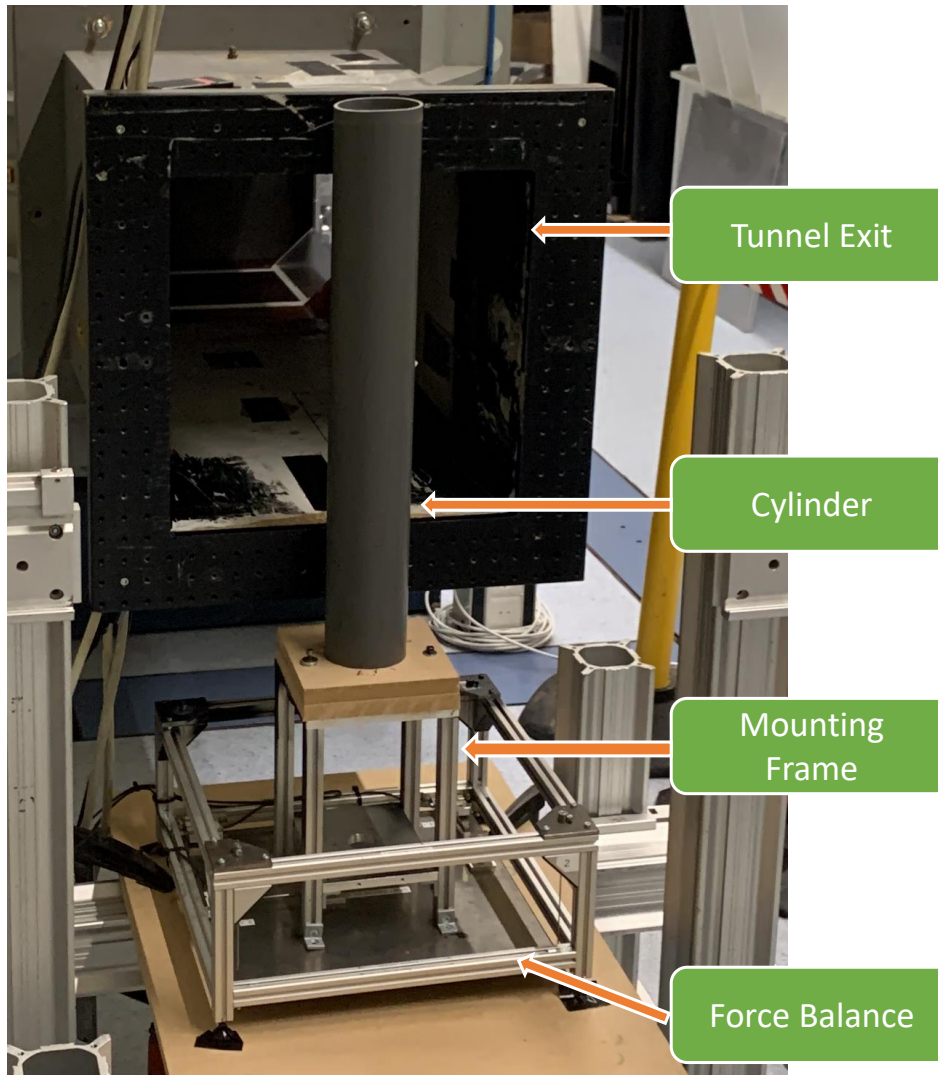


Figure 4.6: Experimental setup showing the cylinder attached to the force balance using the mounting fixture.

4.3.2. Balance Details

The force balance employed for the measurements had a high precision and sensitivity. It was equipped with three load cells: two in the flow direction (x-direction) and one in the flow normal direction (y-direction). No load measurements were made in the cylinder longitudinal axis (z-direction). The load cells were S-shaped load cells (type: KD40s) with maximum range of ± 50 N with a maximum error of $\leq 0.1\%$ ¹. Therefore the balance was limited to a maximum load of 100 N in the drag direction and 50 N in the flow normal direction; both far outside the expected load regime.

¹Force Sensor KD40s https://www.me-systeme.de/product-pdf?product_id=1734&lang=en

The acquisition rate of the force balance was set to 25 kHz. The Strouhal number of a cylinder tends to remain around 0.2 except in the drag crisis where the value may reach 0.5 as reported by Bearman [4]. These correspond to a maximum oscillation frequency of less than 200 Hz and a maximum oscillation time (corresponding to the lowest frequency oscillation) of less than 1 s. Therefore the chosen sampling frequency of 25 kHz was deemed satisfactory and the measurements were recorded for 15 s each time. The whole measurement, acquisition and recording system was controlled using a LabView module designed for the specific balance used. Furthermore, the balance underwent re-calibration prior to the start of the experimental campaign.

The recorded data from the force balance, including the force values in the three load cells, were saved in TDMS files where each load cell represents one channel. The average load value was also separately written to file by the balance interface.

4.3.3. Measurement Methodology

During the experiments, the following workflow was used in the balance measurements:

- The tunnel was set to 0 RPM and the tunnel details were logged along with one measurement duration of the balance. This measurement is henceforth referred to as the 'zero measurement'
- Measurements were carried out at each velocity
 - The RPM of the tunnel was set to the desired value
 - After the desired RPM (and therefore flow velocity) was attained, and the flow had become stationary, the tunnel logger and the load logger were run simultaneously
 - *Balance measurements were carried out over 15 seconds*
 - The next RPM was set or the tunnel-drive was stopped if it was the last measurement

Each cylinder underwent a sweep of the following velocities: 5, 10, 15, 20 & 25 m/s. After all cylinders were measured, the measurements were repeated. In the second series of measurement readings were also recorded at 7.5 and 12.5 m/s for cylinders where it was seen from the first series of measurement that there were large gradients in the load.

4.4. Particle Image Velocimetry

PIV was used in the experimental campaign in order to gain a flowfield level understanding of the effect that polka-dots have on cylinder flow. While Chapter 3 presented a brief background regarding PIV and processing algorithms, this section presents the specific setup and analysis techniques used in this research. Two different PIV setups were used in this research, one to image the boundary layer and another to image the wake. These are numbered 1 and 2 respectively. Each of them have slightly different characteristics and due to their differing goals, their data processing also took different paths. The specifics of the setup, such as the optical details, the acquisition system and the illumination are presented in Section 4.4.1. This is followed by Section 4.4.2 where the data processing steps carried out are presented.

4.4.1. PIV Setup

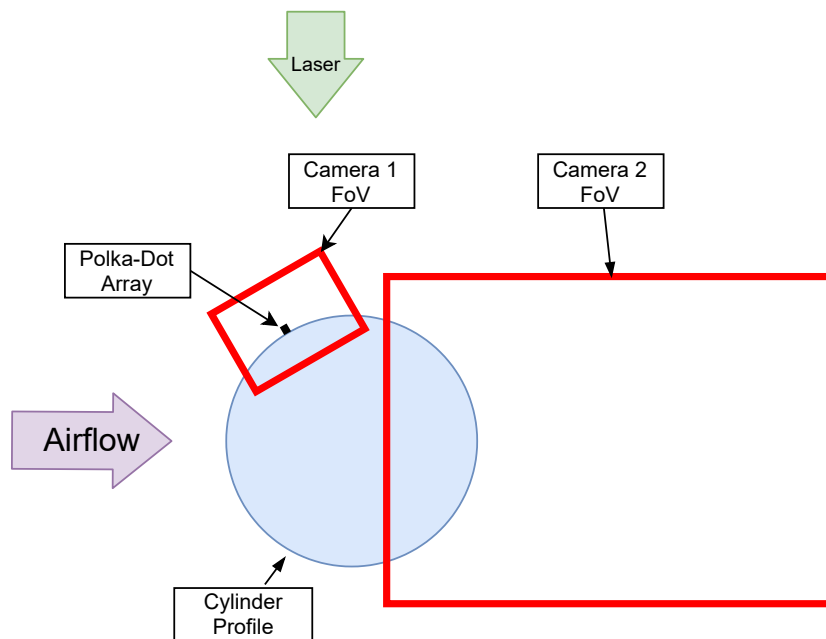


Figure 4.7: A schematic representation of the PIV setup showing the cylinder in the flow and the two fields of view present (not to scale).

Figure 4.7 schematically shows the two fields of view that were used to measure the flowfield in the two regions of interest. The goal of FoV 1 is to record the boundary layer tripping, and boundary layer quantities such as the thicknesses and the profile. The goal of FoV 2 is to capture the flow in the wake and enable the calculation of the wake-width at different downstream stations. The names and basic specifications of the cameras, the laser, the timing unit and the software are presented in Table 4.5.

Table 4.5: Specification of the equipment and software used in the PIV setup.

Camera	LaVision Imager sCMOS
Sensor Size (px x px)	2560 x 2160
Sensor Size (mm x mm)	16.6 x 14.0
Pixel Size (μm x μm)	6.5 x 6.5
Laser	Quantel Evergreen 200 I
Laser Wavelength (nm)	532
Pulse Energy (mJ)	200
Timing Unit	LaVision PTU X
Processing & Capturing Software	DaVis 8

FoV 1 captures the cylinder surface. It is positioned close to the cylinder itself in order to minimise the obscuring of the measurement plane by the foreshortening of the cylinder edge closest to the camera. FoV 2 is positioned symmetrically along the tunnel axis in the wake of the cylinder. It measures the base region of the cylinder and upto a distance of about 2 diameters downstream of the trailing edge of the cylinder. More specific parameters of each FoV is presented in Table 4.6.

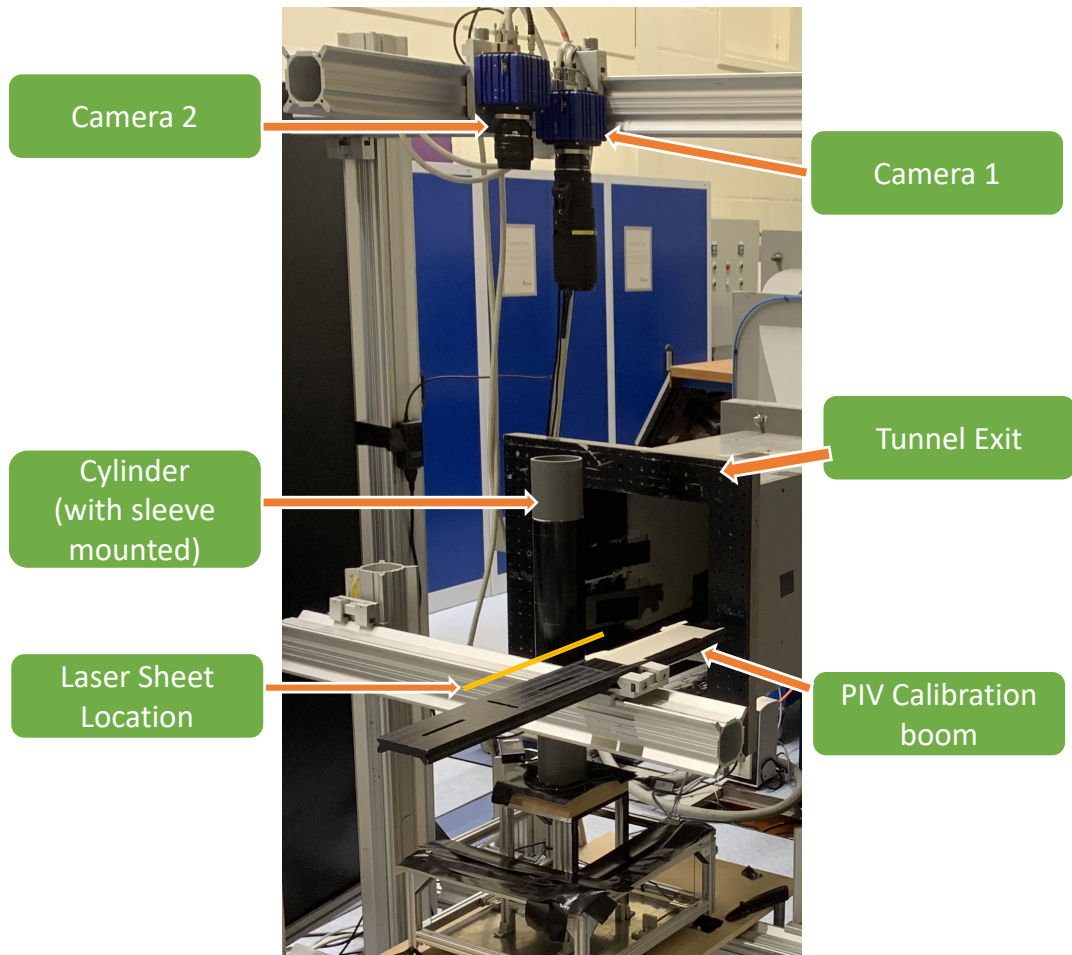


Figure 4.8: A picture of the two PIV cameras positioned relative to the cylinder. The calibration boom is only used during the capturing of images for scaling. When the PIV measurements are carried out, the calibration boom is removed altogether.

Table 4.6: The optical and laser related variables of each of the PIV setups.

Parameter	Camera 1	Camera 2
Lens Focal Length (mm)	200	35
Sensor size (px x px)	2560 x 2160	2560 x 2160
Pixel Size (μm)	6.5	6.5
Field of View (cm x cm)	4.3 x 3.6	25 x 21
Magnification Factor	0.39	0.067
Digital Image Magnification (px/mm)	59.5	10.2
F-Stop	8	16
Number of image pairs in ensemble	200	200
Pulse Separation @ 5 m/s (ms)	35	200
Pulse Separation @ 10 m/s (ms)	17.5	100
Pulse Separation @ 15 m/s (ms)	12	67
Pulse Separation @ 20 m/s (ms)	9	50
Laser Sheet Thickness (mm)	2	2

4.4.2. PIV Processing

This subsection outlines the processing steps carried out within the *DaVis 8* software. This starts with the capturing of the images and ends with the velocity field being output in a data file. The steps for images in FoV 1 are different to those used in FoV 2.

Field of View 1

FoV, as shown in Figure 4.7, is relatively further zoomed into the setup. Additionally, due to the cantilever fastening of the cylinder and the cyclic nature of the loads a cylinder experiences, vibrations were observed in the cylinder. A result of this is that the cylinder position changed between the images captured by camera 1. Therefore, the images from camera 1 were first shift-corrected.

- Capturing of 200 image pairs with pulse separation time as stipulated in Table 4.6.
- Shift correction of all image pairs.
- Masking of cylinder surface.
- Sum of Correlation PIV (correlation average method).
- Output of averaged velocity field.

Field of View 2

- Capturing of 200 image pairs with pulse separation time as stipulated in Table 4.6.
- Masking of cylinder and regions obscured from the laser.
- PIV cross-correlation of each image pair to obtain velocity field.
- Statistical Averaging of velocity field.
- Output of average and standard deviation of velocity field.

For the boundary layer analysis, a high resolution of the velocity vectors is needed in order to resolve the profile close to the wall. The correlation averaging method allows stable computation at smaller interrogation window sizes due to the greater signal-to-noise ratio and therefore it is used for the boundary layer analysis. For the wake analysis, the resolution is satisfactory from the velocity averaging method and therefore owing to the advantage of obtaining the velocity fluctuation, the velocity averaging was used.

4.5. Data Reduction

This section presents the data processing that was carried out from the output received from the LabView software for the balance results and DaVis 8 for the PIV results. It outlines the steps and results received. These results are used in Chapter 5 to draw conclusions regarding the flow field and to structure an answer to the research questions. The data reduction for the balance data in order to receive drag values is presented in Section 4.5.1 and the processing of the PIV data is presented in Section 4.5.2.

4.5.1. Balance Data

The data obtained from the balance software is the average load in each of the three load cells of the balance for the 15s measurement time. Additionally, the recorded velocity and density from the wind tunnel logger were utilised. The process follows the path: subtraction of 0 reading, blockage correction, and finally calculation of the Reynolds number & drag coefficient.

As mentioned in Section 4.3.3, for each cylinder, a 'zero reading' is taken for the balance with the tunnel drive turned off. This value is first subtracted from all the load values. The total drag value is obtained by summing the load values in the two load cells that measure the load in the x-direction. The recorded velocity values are then corrected for the tunnel blockage using Equation (4.7). The value -0.021 comes from the solid blockage factor calculated in Section 4.2 based on the model and tunnel geometry.

Finally the drag force is non-dimensionalised to the drag coefficient using equation Equation (4.9). Here $D = 0.09\text{ m}$ and $l = 0.4\text{ m}$ based on the cylinder dimensions. Additionally, the Reynolds number is calculated using Equation (4.8). The kinematic viscosity ν is $1.46 \cdot 10^{-5}\text{ m}^2/\text{s}$ which is the ISA value at sea level (the wind tunnel is located at sea level).

$$V_{corr} = V_{unc}(1 + \varepsilon) = V_{unc}(1 - 0.021) \quad (4.7)$$

$$Re = \frac{V_{corr}D}{\nu} \quad (4.8)$$

$$C_d = \frac{F_D}{\frac{1}{2}\rho V_{corr}^2 Dl} \quad (4.9)$$

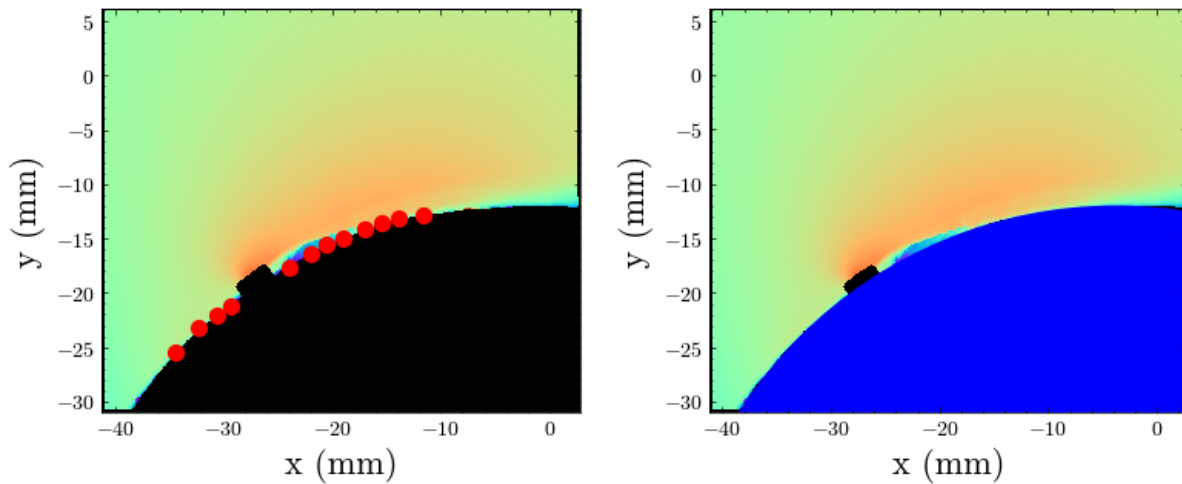
4.5.2. PIV Data

As before, the PIV data is divided between the boundary layer data and the wake data. First the data reduction for the boundary layer data is presented followed by the same for the the wake data.

Boundary Layer PIV Data

The goal of the boundary layer field of view is to obtain the boundary layer profiles at different azimuth locations and also integral boundary layer quantities from these profiles. From the velocity fields, first the cylinder centre was detected. For this, 10-15 points along the mask boundary were selected manually as shown with the red dots in Figure 4.9a. From this, the least squares solution for a circle was calculated, which was used as an estimation method of the centre of the cylinder profile at the PIV measurement plane, which is overlaid in blue in Figure 4.9b. As was shown in Figure 2.2, the coordinate system used is also centred at this point. Following this, the velocity profiles at given angular locations were extracted. This was done by linearly interpolating the PIV velocity field at the angular positions selected. The profile is extracted from 5% of the radius within to 5% outside the cylinder surface as shown in Figure 4.10. As shown in Figure 4.10, it is also seen that after the velocity in the boundary layer attains a value of U_e (the maximum velocity in the profile), it tapers off as distance from wall is increased as it tends towards the free stream velocity.

As a result, the maximum velocity is used as the external driving velocity U_e .



(a) The manually selected points for a least squares fit of a circle.

(b) The circle estimated through a least squared fit on the manually selected points is shown in blue.

Figure 4.9: The estimation of the cylinder profile location in FoV 1 for cylinder 5 ($k = 1.5$ mm, $d = 3$ mm). In both subfigures, the plotted quantity is the velocity magnitude, but a colorbar is not shown as this quantity is not of interest here.

From the boundary layer profile, the following quantities are calculated: 95% thickness (δ_{95}), displacement thickness (δ^*), momentum thickness (θ), and the shape factor (H).

The displacement thickness is a measure of the imaginary distance by which the solid boundary would need to be displaced to accommodate the same mass flow rate as the actual boundary layer, assuming undisturbed flow outside the boundary layer. A low displacement thickness implies that the boundary layer is thin and close to the solid surface. This indicates that there is little disturbance to the flow outside the boundary layer, with most of the flow occurring near the surface. In contrast, a high displacement thickness suggests a thicker boundary layer and greater displacement of fluid away from the surface. This indicates increased disturbance to the flow outside the boundary layer, with a significant portion of the flow occurring further away from the surface. The expression used is presented in Equation (4.11). Here, u_r represents the velocity tangential to the cylinder profile at a given azimuth.

The momentum thickness characterises the reduction in momentum flux across the boundary layer and quantifies the thickness of a hypothetical boundary layer with the same momentum flux as the actual boundary layer. A low momentum thickness signifies a boundary layer with a streamlined velocity profile and less momentum redistribution. This implies a more orderly flow, typically associated with laminar boundary layers. Conversely, a high momentum thickness indicates a boundary layer with a more rounded or blunt velocity profile and greater momentum redistribution. This signifies increased mixing and turbulence, often observed in turbulent boundary layers. Its formulation is presented in Equation (4.12).

The shape factor, defined as the ratio of the displacement thickness to the momentum thickness, provides information about the shape of the velocity profile within the boundary layer. A high shape factor indicates a streamlined velocity profile with a relatively larger displacement thickness compared to the momentum thickness. This suggests a more laminar flow regime with less turbulence and orderly fluid motion. In contrast, a low shape factor implies a more rounded or blunt velocity profile, where the momentum thickness is relatively larger compared to the displacement thickness. This signifies a more turbulent flow regime with greater levels of mixing and turbulence. For laminar boundary layers, a value of approximately 2.6 is expected and a value of 1.4 is expected

for a boundary layer has transitioned to turbulence. Due to the adverse pressure gradient, as the boundary layer develops and grows more concave, the value of shape factor for both the laminar and turbulent state is expected to grow [27]. Its formulation is presented in Equation (4.13).

For all the integral quantities, the integration was carried out using the in built composite trapezoidal integration function of NumPy.² These quantities are then used to compare the performance of different roughness configurations and their effect on the boundary layer.

$$\delta_{95} = 0.95 \cdot U_e \quad (4.10)$$

$$\theta = \int_R^{\delta_{95}} \left(1 - \frac{u_t(r)}{U_e}\right) \left(\frac{u_t(r)}{U_e}\right) dr \quad (4.12)$$

$$\delta^* = \int_R^{\delta_{95}} \left(1 - \frac{u_t(r)}{U_e}\right) dr \quad (4.11)$$

$$H = \frac{\delta^*}{\theta} \quad (4.13)$$

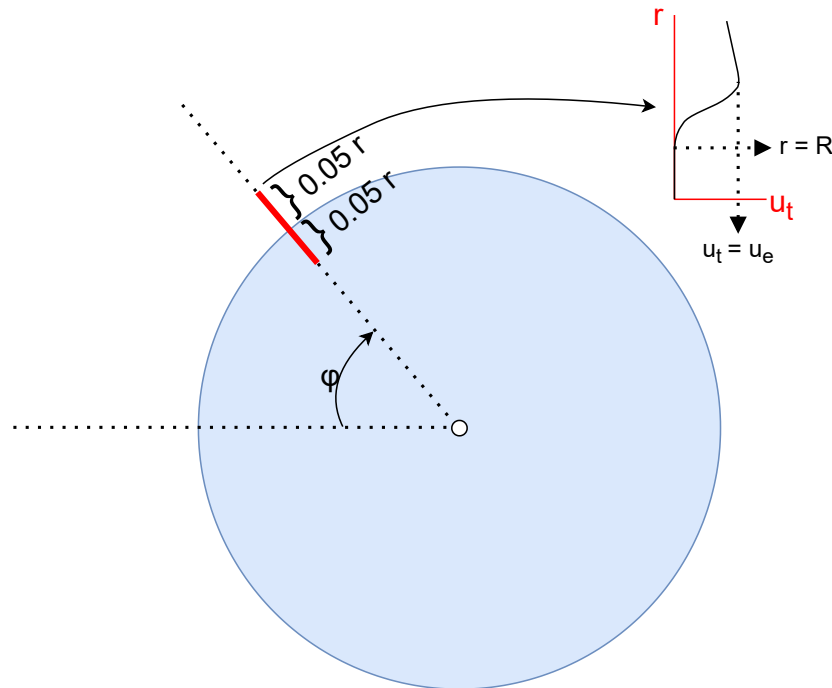


Figure 4.10: A schematic overview of the boundary layer profile extraction. The vertical axis in the shown plot corresponds to the thick red line shown at angle ϕ where the velocity is sampled.

Wake PIV Data

The PIV imagery of the wake flow was used to extract the velocity profile and thereafter obtain the wake width for each cylinder and velocity combination. The standard deviation of the wake velocity is first extracted at a given location downstream of the cylinder, as shown in Figure 4.11. The standard deviation represents the velocity fluctuation and therefore the turbulence intensity in the flow at that location. The wake extreme points are then defined as the location of maximum turbulence intensity, (marked in Figure 4.11 with a black **x**) the same techniques used by Rodríguez et al. [22]

²NumPy composite trapezoidal integration User Guide: <https://numpy.org/doc/stable/reference/generated/numpy.trapz.html>

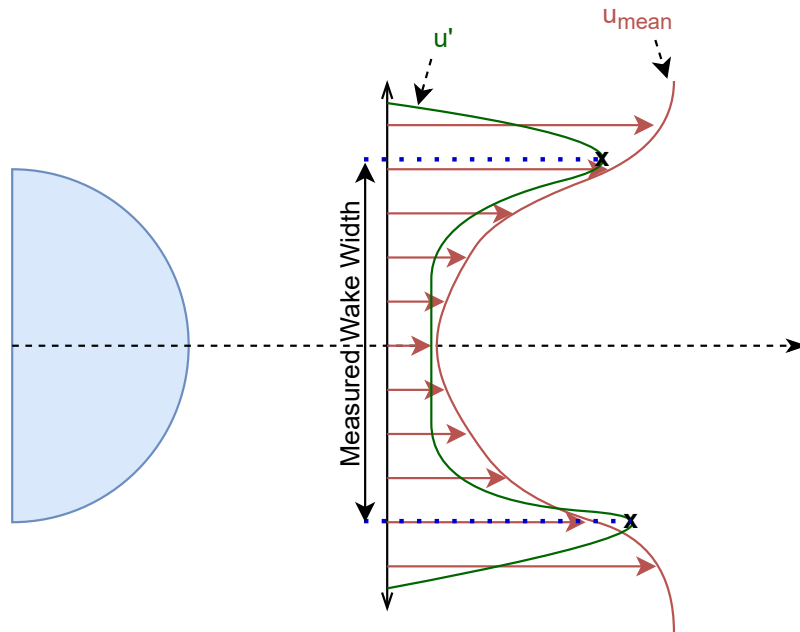
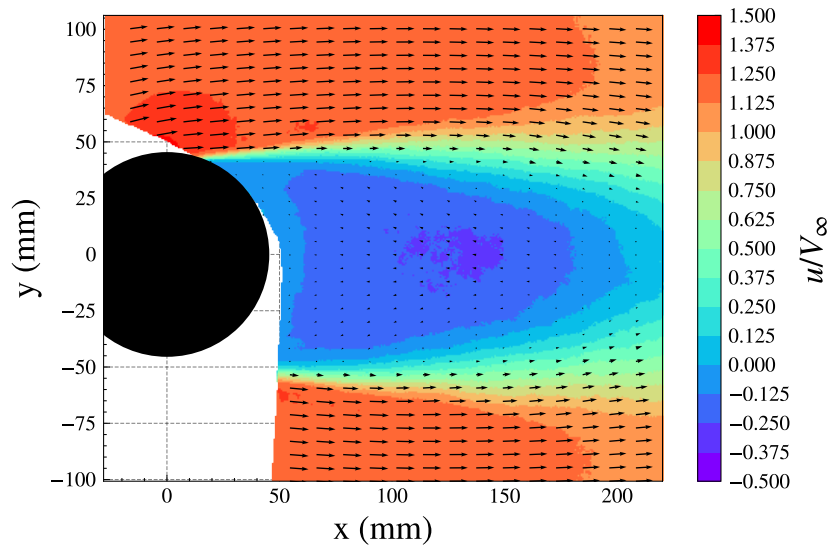
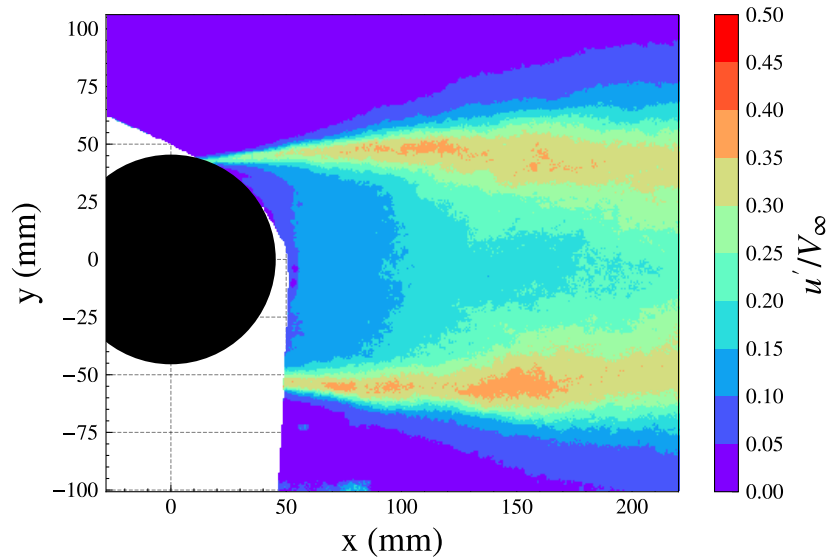


Figure 4.11: Schematic representation of the wake profile analysis carried out. The mean velocity profile (u_{mean}) is shown in red and the velocity fluctuation profile (u') is shown in green. The two maximum fluctuation points mark the upper and lower boundary of the wake.

While the schematic diagram shows a smooth fluctuation curve, the true fluctuation curve includes noise. This is exemplified in Figure 4.12 which shows the mean flow and the standard deviation of the wake of cylinder 6. Specifically Figure 4.12b exemplifies the noisy data seen in the standard deviation of the flow velocity.



(a) The average wake flow.



(b) The standard deviation of the wake flow.

Figure 4.12: The process of the calculation of the wake width shown for cylinder 6 at $Re = 1.5 \cdot 10^5$. The black circles mark the calculated location of the cylinder profile in the measurement domain, freestream flow is in the positive x-direction.

The wake profile of the standard deviation of the velocity from Figure 4.12b is extracted at $x = 100$ mm and presented in Figure 4.13. In order to reliably select the two peaks, the profile was divided into the upper and lower half and the maximum was located thereafter for each profile. This ensured that the opposite sides of the wake were located by the algorithm rather than two points coinciding with one side of the wake. The located peak intensity locations are marked in Figure 4.13 with red horizontal lines. This splitting of the profile involved the assumption that the wake develops mostly symmetrically. As is presented in Section 5.3, the wake widths were all measured to be greater than the diameter of the cylinder (90mm) which verifies the correct working of this precautionary method.

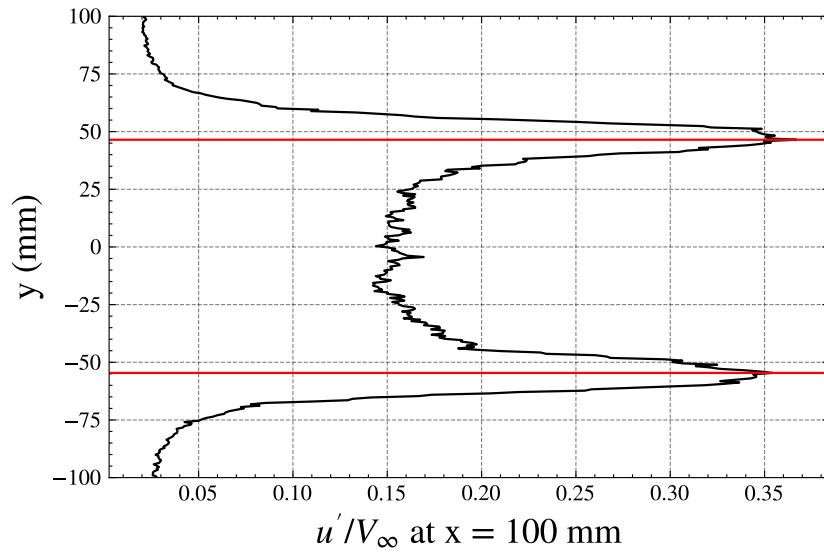


Figure 4.13: The profile of the standard deviation of the streamwise velocity normalised with the freestream velocity at $x = 100$ mm. The red horizontal lines mark the locations of the wake boundary calculated from the maximum turbulence intensity.

5

Results

In this chapter, the findings of the research are presented and critically discussed. The aim of the research was to find the effect of polka-dots on cylinder flow, compare it to existing techniques and assess the changes in the flow with changes in the polka-dot geometry. The analysis was carried out experimentally, simulating the flow in a wind-tunnel, measuring the drag using a balance and imaging the flow using PIV. 11 different polka-dot patterns were assessed, wherein the size and spacing were varied. The load on the cylinder was measured and the boundary layer & wake velocities were measured using PIV. From this the drag coefficient, wake width and boundary layer integral quantities were computed. Along with this, the bare cylinder and a cylinder with a zigzag strip applied was also measured using the same techniques.

In order to contextualise the effect of the polka-dot arrays, Section 5.1 first presents the results from the analysis carried out upon the bare cylinder. It also presents the experimentally obtained boundary layer profiles of the cylinder. Following this, the effect of the polka-dot elements is analysed in Section 5.2. The different geometries tested are compared amongst each other, with the bare cylinder and the zigzag strip. Finally, in Section 5.3, information that can be gained from obtaining the wake width of the cylinders is examined.

These results are critically examined with the literature discussed in Chapter 2 in mind to answer the research questions posed in Section 2.4. The insight gained and the drawbacks of the methods are both used to deliver a conclusion and recommendations for further research in Chapter 6.

While some of the flow-field visualisations are shown in this chapter to present results and highlight different in flow characteristics, for the sake of clarity, not all of the measurements are shown. As they still provide greater insight to the different effects each polka-dot configuration has on the cylinder flow, the boundary layer flow images are presented in Appendix A.

5.1. Bare Cylinder Results

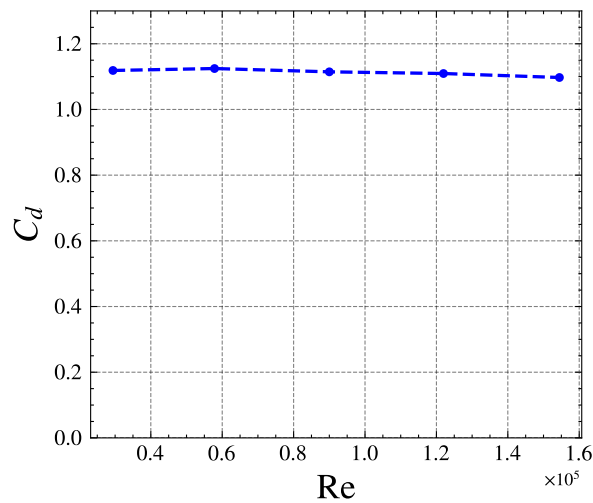


Figure 5.1: The coefficient of drag plotted against Reynolds number for a bare cylinder.

The coefficient of drag of the bare cylinder as obtained experimentally is plotted in Figure 5.1. The value is nearly constant at about 1.1. The data obtained from Wieselbergers (Figure 4.5), on the other hand, indicates the drag coefficient to be at a value of about 1.25 in the regime in which this research was carried out. The experimental setup of Wieselbergers' research used endplates on the edges of the cylinder and cylinders with slenderness ratio of at least 280 in order to simulate a 2D cylinder as well as possible, i.e., to minimise the tip effects caused by the cylinder ends [35].

In this research on the other hand, as seen in Figure 4.6, the top of the cylinder extends about 10 cm out of the tunnel exit jet. The cylinder was placed as close as possible to the tunnel exit keeping this in mind. Additionally, since the length of the cylinder model was 60 cm, the fineness ratio of the model was about 6.67. This is far lower than the value used by Wieselbergers. The drag coefficient is therefore lower owing to the tip effect of the cylinder and this is seen in the discrepancy between the the data obtained from Wieselbergers' research and the data presented in Figure 5.1.

Even given the caveat presented above, the differences seen in the flow features of the different roughness configurations was enough to characterise the effects of the polka-dots on the flow and drag. Furthermore, the constant value of the drag coefficient in Figure 5.1 suggest that within the range of measurements, the cylinder is in subcritical flow as expected. This is confirmed by the laminar separation seen in Figure 5.2 for all four Reynolds numbers at which PIV measurements were made.

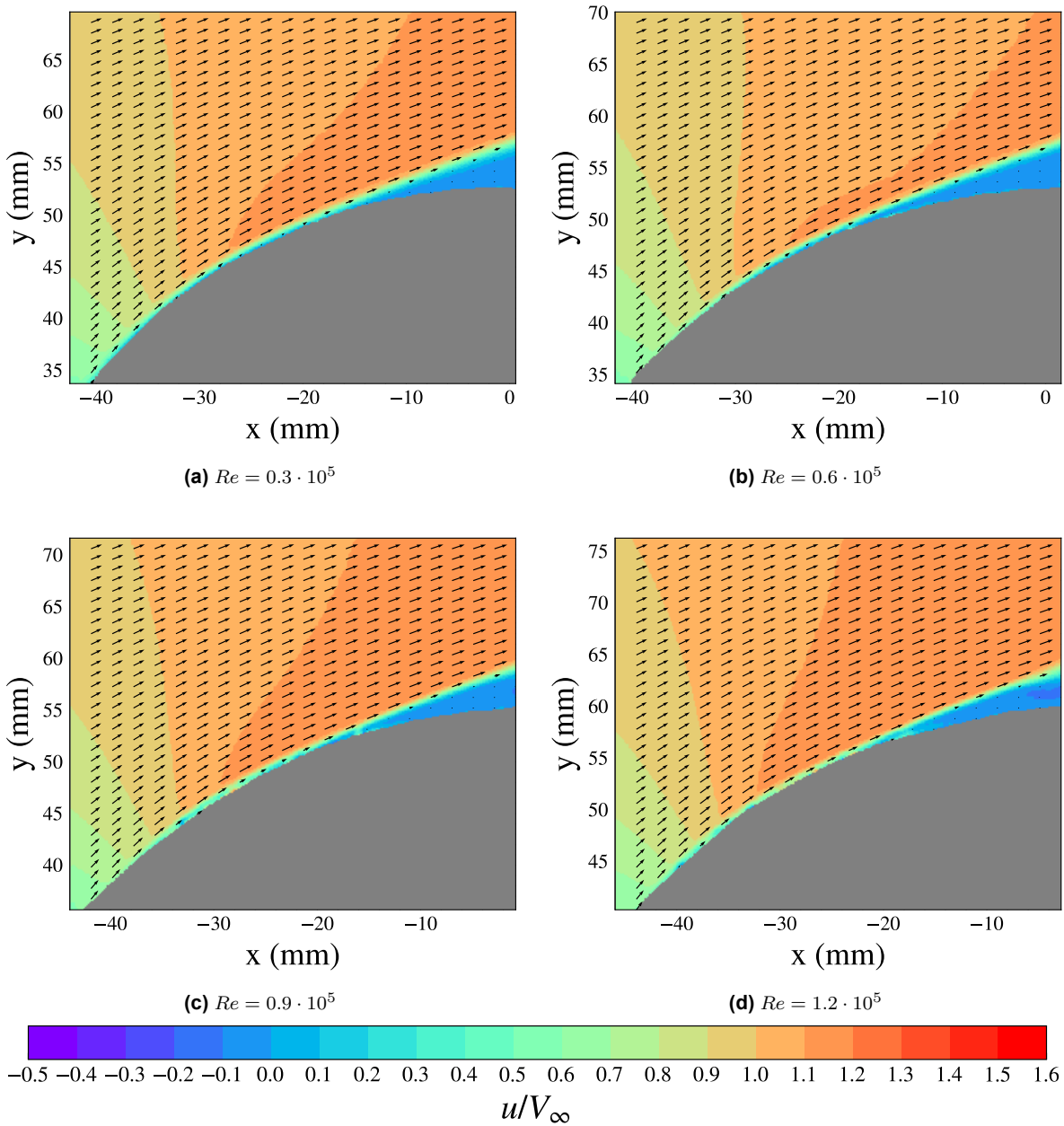


Figure 5.2: Boundary layer flow of the bare cylinder at different Reynolds numbers within the tested regime. Laminar separation is seen in all of the flow figures.

While not trivially visible from a qualitative analysis of Figure 5.2, the bare cylinder sees separation at a lower azimuth with increasing Reynolds number in the regime measured. This is made visible in the comparison plots presented in Figure 5.3 where the boundary layer profiles at $\phi = 50^\circ$, 60° , 70° and 75° are shown for each of the Reynolds numbers where measurements were made. The development of the boundary layer is characterised by an increasing concavity of the profile (decreasing near-wall velocity gradient) with increasing azimuthal position. The changing position of the separation is exemplified by the differences in the boundary layer development in Figure 5.3a ($Re = 0.3 \cdot 10^5$) and Figure 5.3b ($Re = 0.6 \cdot 10^5$). For the lower Reynolds number, the first sign of separation is seen at $\phi = 75^\circ$ whereas at the greater Reynolds number, the same level of convexity is seen at $\phi = 70^\circ$. With increasing Reynolds number, a much greater degree of convexity is seen. For $Re = 0.3 \cdot 10^5$ the profile sees a positive velocity already at a velocity at $y = 0.15$ mm, but with increasing Reynolds, this distance grows and at $Re = 1.2 \cdot 10^5$ the nearest-to-wall location at which positive velocity is seen is $y = 0.8$ mm.

It is also seen that with increasing Reynolds number, larger nonphysical kinks in the lower parts of the boundary layer curves are seen. This is credited to the high levels of vibrations that were seen at the greater free stream tunnel velocities. This is the case especially at $Re = 0.9 \cdot 10^5$ and $Re = 1.2 \cdot 10^5$. While a shift correction was carried out on the captured ensemble of 200 images as presented in Section 4.4.2, the vibrations in this case were deemed to be too large to be completely corrected for. It should also be noted that these vibrations were greatest for the bare cylinder as the drag force was also the greatest for the bare cylinder. Furthermore, despite the kinks seen in the nearest-to-wall parts of the boundary layer profiles, the general shape of the boundary layer can still be characterised and the height be measured.

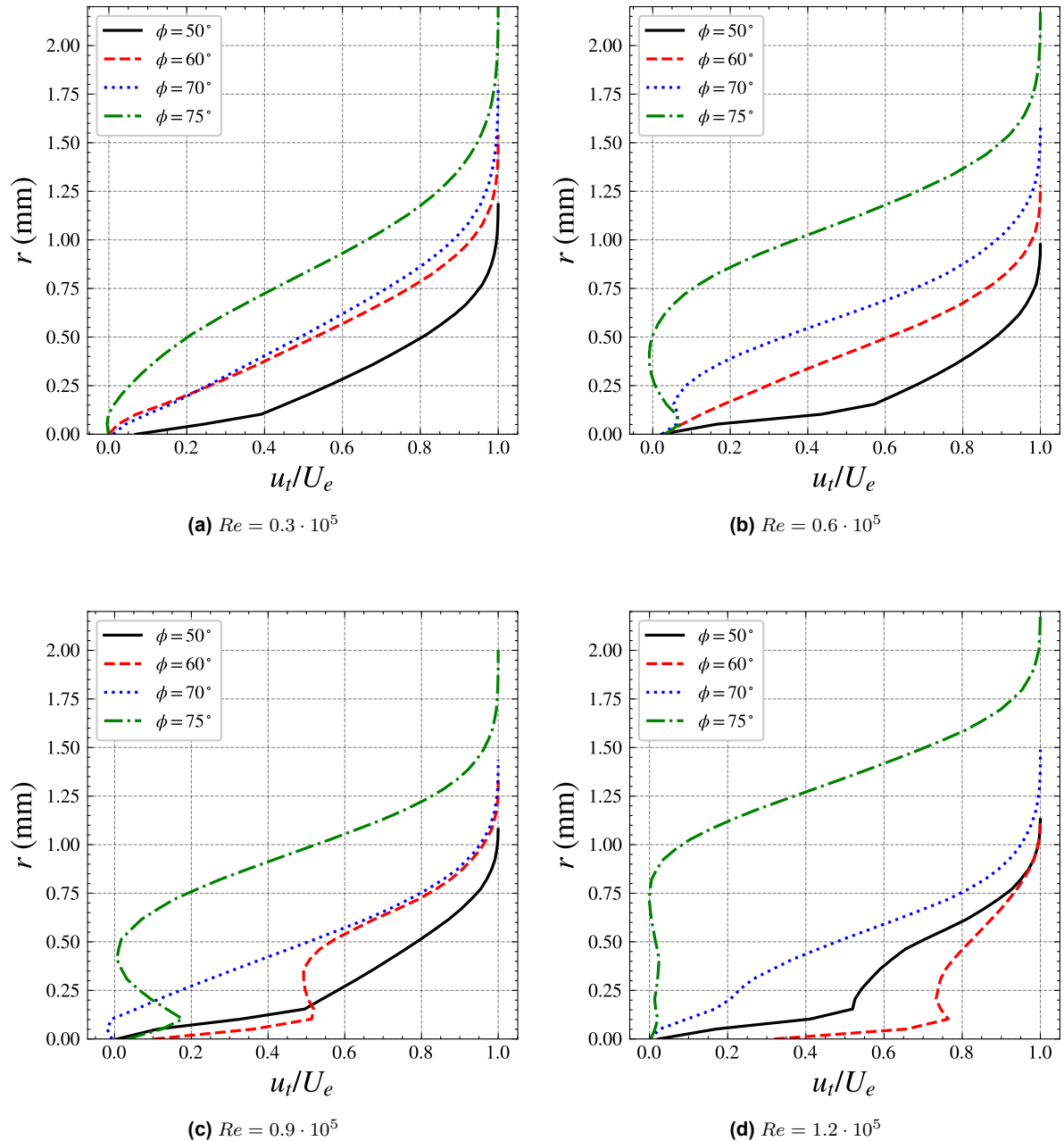


Figure 5.3: Boundary layer profiles for the bare cylinder shown at $V = 5$ m/s, 10 m/s, 15 m/s and 20 m/s. Each sub-figure shows the profiles for 4 different azimuthal position.

5.2. Polka-Dot Analysis

In this section the different configurations of polka-dots are analysed on the basis of the effect they have on the flow around the cylinder. To this end, the PIV data obtained of the boundary layer and the drag data obtained from the balance are used. Section 5.2.1 presents the analysis for the research question pertaining to polka-dot height (series A & B), Section 5.2.2 to polka-dot shape (series C), and Section 5.2.3 to polka-dot spacing (series D).

5.2.1. Effect of Polka-Dot Height

This subsection presents the analysis of the differences between the flow around cylinders where the polka-dot height is varied for a constant polka-dot diameter. Table 4.2 presents all the cylinder configurations used in these series and is repeated below for the reader's convenience.

Series A and B cylinders share the same dimensions for polka-dot diameter ($d = 1.5$ mm) and have the same range of polka-dot heights but series A cylinders have a polka-dot spacing of 1.5 diameters whereas series B cylinders have a spacing of 2.5 diameters.

Table 4.2 (repeated): The dimensions of polka-dot configurations in series A and B cylinders where the polka-dot height is varied.

Cyl. Nr.	k (mm)	d (mm)	AR	S/d	N (mm)	Series
9	1.5	1.5	1	1.5	2.25	A
10	1	1.5	0.68	1.5	2.25	A
11	2.2	1.5	1.47	1.5	2.25	A
12	3	1.5	2	1.5	2.25	A
2	1.5	1.5	1	2.5	3.75	B
6	1	1.5	0.68	2.5	3.75	B
7	2.2	1.5	1.47	2.5	3.75	B
8	3	1.5	2	2.5	3.75	B

The coefficient of drag measured for varying Reynolds numbers in the measurement regime is presented below for series A cylinders in Figure 5.4a and for series B cylinders in Figure 5.4b. Along with this, the drag curves for the bare cylinder and the one with the aforementioned zigzag strip are also shown.

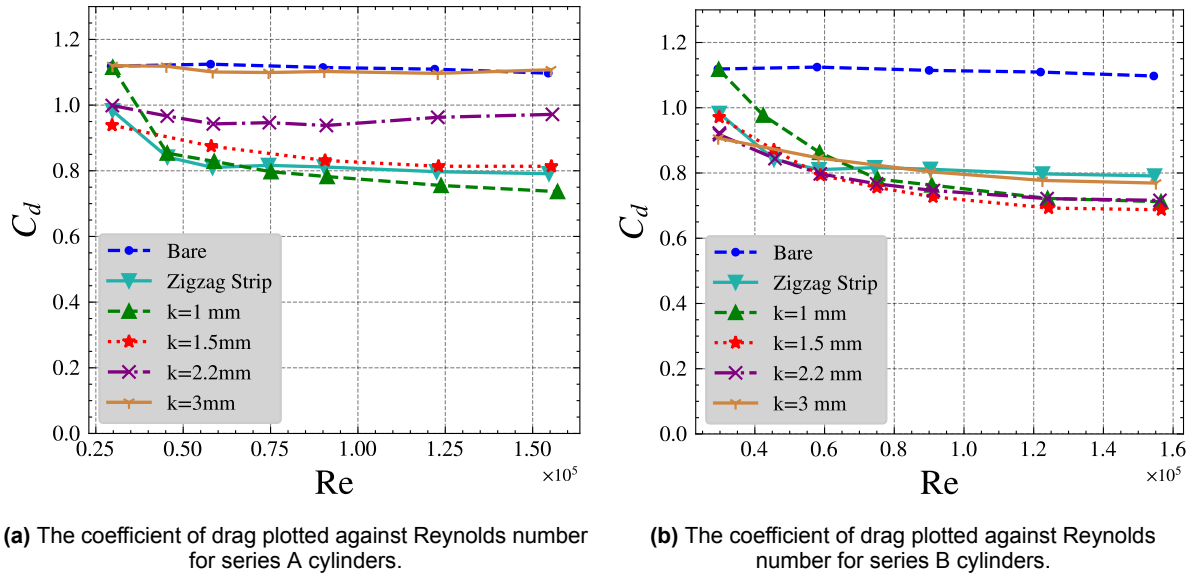


Figure 5.4: The effect of polka dot height as seen in the drag coefficient of the cylinders. Here, polka-dot diameter is constant for spacing of (a) 1.5 diameters and (b) 2.5 diameters.

In the series A ($S/d = 1.5$) cylinders, the shorter the polka-dot the lower the value of the $C_{d,min}$ measured. On the other hand, for series B ($S/d = 2.5$), a less pronounced difference is seen between the $C_{d,min}$ values obtained in the measurement regime. In series B though from $k = 1.5$ mm to $k = 3$ mm a steady increase in $C_{d,min}$ is seen. When considering both series A & B, a general trend of increasing $C_{d,min}$ with polka-dot height is seen.

While the start of the drag crisis for most configurations does not lie within the regime investigated, it is possible to ascertain the relative positions of the Re_{crit} . This is done qualitatively based on the slope of the curve at the lower end of the investigation regime. The steeper the curve, the greater the value for Re_{crit} is likely to be. As is seen for $k = 1$ mm (the green curves), the gradient is the steepest and $Re_{k,crit}$ lies within the investigation regime.

For cylinder 10 (series A, $k = 1$ mm, $d = 1.5$ mm, $S/d = 1.5$) the $Re_{k,crit}$ is measured to be 400 and for cylinder 6 (series B, $k = 1$ mm, $d = 1.5$ mm, $S/d = 2.5$) is measured to be 376. The increase in the spacing by 1 diameter increases the $Re_{k,crit}$ by about 6.4%. This is much lower than the results obtained by von Doenhoff and Braslow which expect a 40% increase as presented in Figure 2.19a [34].

Furthermore, according to the findings of von Doenhoff and Braslow the $Re_{k,crit}$ of a polka-dot element scales with $\frac{1}{(AR)^{0.4}}$. The range of $Re_{k,crit}$ presented by them for a polka-dot with aspect ratio of unity is 600-900. For a singular polka-dot from cylinders 10 and 6 ($AR = \frac{1}{1.5}$), this value is range is calculated to be approximately 705-1060. Then based on the effect of spacing presented by von Doenhoff and Braslow in Figure 2.19a, the range for cylinder 10 should be 400-600 and for cylinder 6 it is calculated to be 600-900. The values 376 and 400 calculated both lie below the corresponding ranges. Two explanations are put forth for this. The first is the strong pressure gradient which could work to amplify instabilities in the flow and reduce the threshold of the Reynolds number required to trip the flow. Based on this, it is expected that with increasing Re (Reynolds number of the cylinder) this $Re_{k,crit}$ reducing effect becomes stronger as the inherent instabilities in the flow become stronger due to the cylinder nearing the TrBL (transition in boundary layer) state. The second reason for this mismatch in value is the fact that the analysis of von Doenhoff and Braslow involved the variation of spacing of two discrete roughness elements while in this research, a large array is considered. Therefore, in the reference literature, one polka-dot's flow was affected by one other polka-dot while in this research it is affected by that of a polka-dot on each side and possibly by the other polka-dots in the array as well. As such, the presence of

a whole array of discrete roughness element is to further reduce the value of $Re_{k,crit}$.

With the method of assessing the gradient of the C_d at the lower end of the measurement regime, it is seen that for both series A and series B, the $k = 1$ mm cylinder has the greatest Re_{crit} , followed by $k = 1.5$ mm, $k = 2.2$ mm. For series B the $k = 3$ mm cylinder also follows this trend, having the least steep gradient, but in series A this is not the case. Cylinder 12 in series A does not see the drag crisis at all and follows a practically identical drag regime as the bare cylinder.

The greater the height of the polka-dot for a given diameter and spacing, the lower the value of Re_{crit} . It must be noted that this does not necessarily mean on a roughness element level that $Re_{k,crit}$ (*roughness height* based critical Reynolds number) increases with height because the effect of shape (aspect ratio) and velocity profile are not isolated here. In fact, within series A and B, the values of k , u_k and the aspect ratio all vary from one configuration to another. Specific details regarding the values of Re_k for both series A & B (including the values at each velocity and polka-dot height) are presented and compared in Section 5.2.1.

Figure 5.5 compares the boundary layer profiles for cylinder 9 ($k = 1.5$ mm), 10 ($k = 1$ mm), and 11 ($k = 2.2$ mm) from series A. A straightforward trend is seen wherein the lower height polka-dot is more effective in energising the near-wall flow. As shown, the plot corresponding to cylinder 10 ($k = 1$ mm) has the sharpest near wall velocity gradient and most convex velocity profile. With increasing polka-dot height the velocity profile becomes increasingly convex. At $\phi = 65^\circ$ all three show some level of energisation. Due to lower effectiveness of the taller polka-dots, the curve corresponding to cylinder 11 ($k = 2.2$ mm) starts to see very low near-wall velocity gradient at $\phi = 65^\circ$. At the same azimuth, the other two curves corresponding to shorter polka-dots still have relatively more energised near-wall velocity profiles. At Between $\phi = 70^\circ$ and $\phi = 75^\circ$, cylinder 11 ($k = 2.2$ mm) sees separation as back-flow appears at the lower section of the boundary layer which is also seen in the flow visualisation in Figure 5.7. Cylinder 12 ($k = 3$ mm) is not included in these plots due to the fact that the flow is separated from the point it interacts with the roughness array as shown in Figure 5.6.

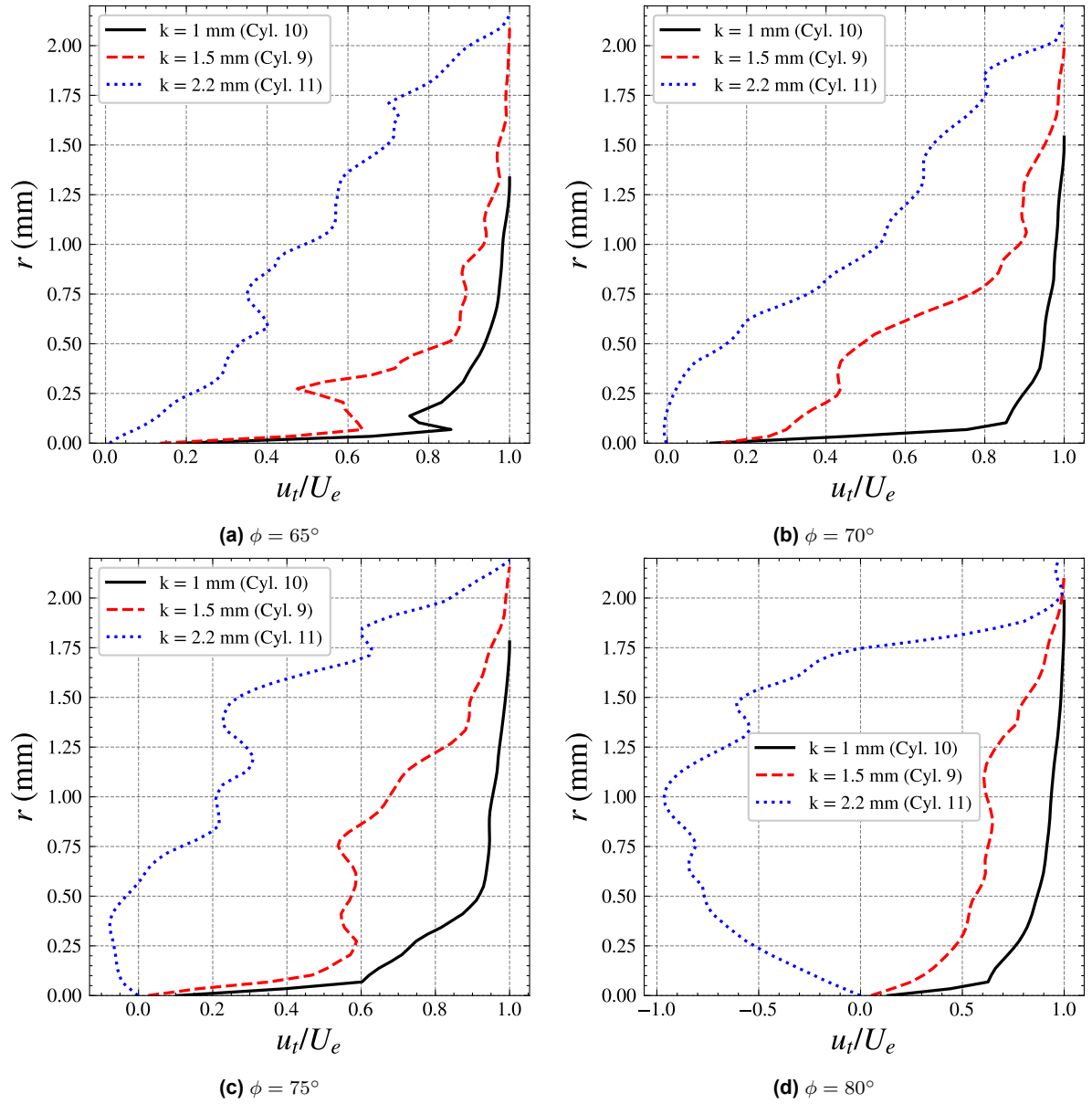


Figure 5.5: Boundary layer profiles of series A (S/d = 1.5) cylinders 10 (k = 1mm), 9 (k = 1.5mm) and 11 (k = 2.2mm) at three different azimuthal locations. $Re \approx 0.9 \cdot 10^5$.

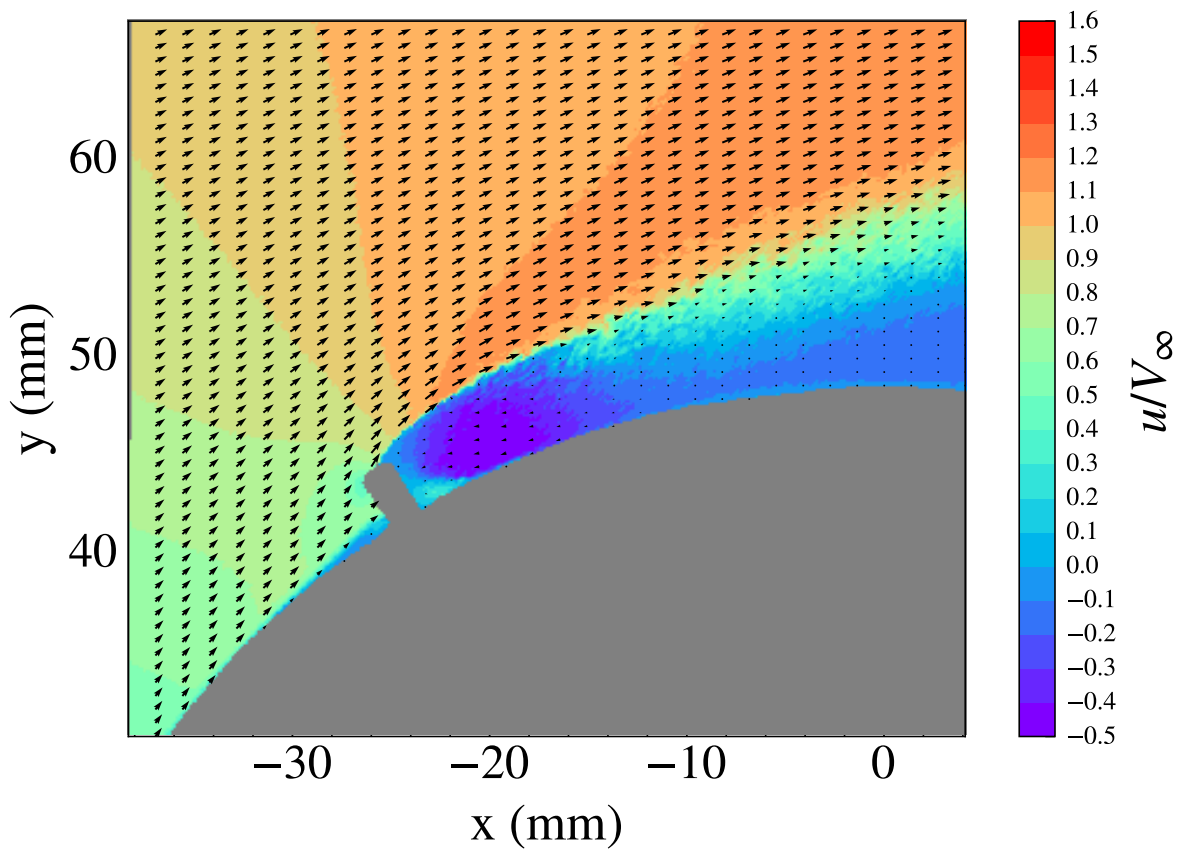


Figure 5.6: The mean boundary layer flow for cylinder 12 at $Re = 0.9 \cdot 10^5$. The flow is separated from $\phi = 60^\circ$

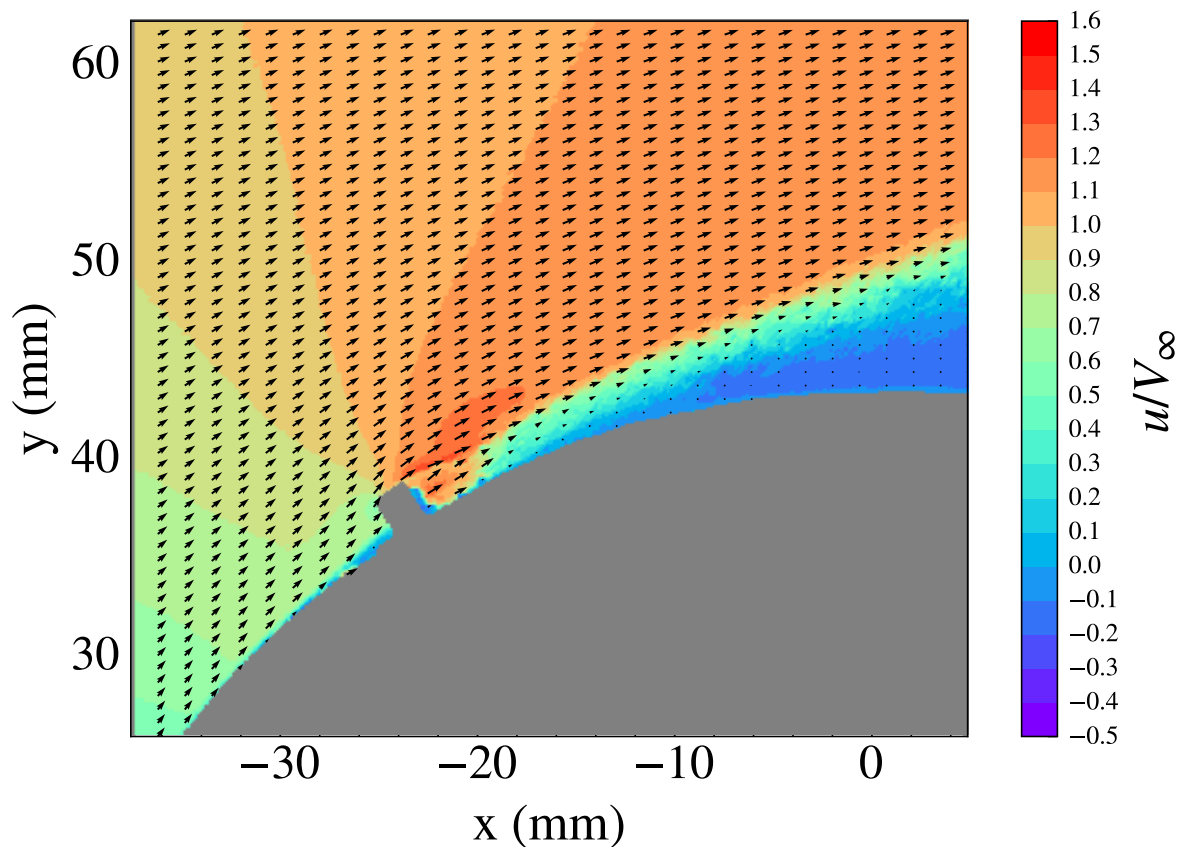


Figure 5.7: The mean boundary layer flow for cylinder 12 at $Re = 0.9 \cdot 10^5$. The flow is attached immediately after the polka-dot but is separated thereafter.

In the case of series B, the trend can be postulated to be similar. Due to the drag coefficient plot being limited by the Reynolds number range measured, information about greater Reynolds numbers is not available. Based on the findings of Brownlie, since cylinder 6 has the greatest Re_{crit} , it should also have the lowest $C_{d,min}$. If that is the case, series B would follow the same trend as series A. Figure 5.8 shows the boundary layer profiles of the 4 series B cylinders at $\phi = 70^\circ$. Similar to series A, it is seen that the shorter the polka-dot, the more convex the velocity profile is observed to be.

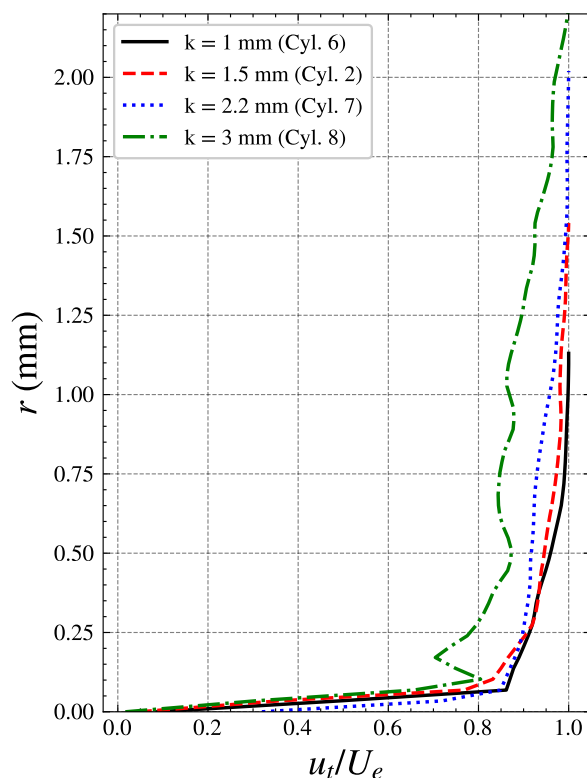


Figure 5.8: Boundary layer velocity profiles of series B cylinders at $\phi = 70^\circ$. $Re \approx 0.9 \cdot 10^5$.

This section focused on the effect of polka-dot height in both series A and series B. In general, smaller polka-dot height was seen to lead to more effective energising of the near-wall section of the boundary layer. This is seen especially in series A but also in series B. Furthermore, Re_{crit} was seen to be greater for smaller values of polka-dot height. Section 5.2.3 focuses further on the results of series A and B from the perspective of polka-dot spacing. It highlight the differences in each corresponding pair of cylinders from series A and B caused by the change in spacing.

5.2.2. Effect of Polka-Dot Aspect Ratio

To assess the effect of polka-dot shape, series C cylinders are compared with one another. Here, the polka-dot height is held constant at 1.5 mm and the polka-dot diameter is varied between 1 mm and 3 mm. Table 4.3 presents the dimensions of all the configurations in series C and is repeated below for the reader's convenience.

Table 4.3 (repeated): The dimensions of polka-dot configurations in series C cylinders.

Cyl. Nr.	k (mm)	d (mm)	AR	S/d	N (mm)
9	1.5	1.5	1	1.5	2.25
3	1.5	1	1.5	1.5	1.5
4	1.5	2.2	0.68	1.5	3.3
5	1.5	3	0.5	1.5	4.5

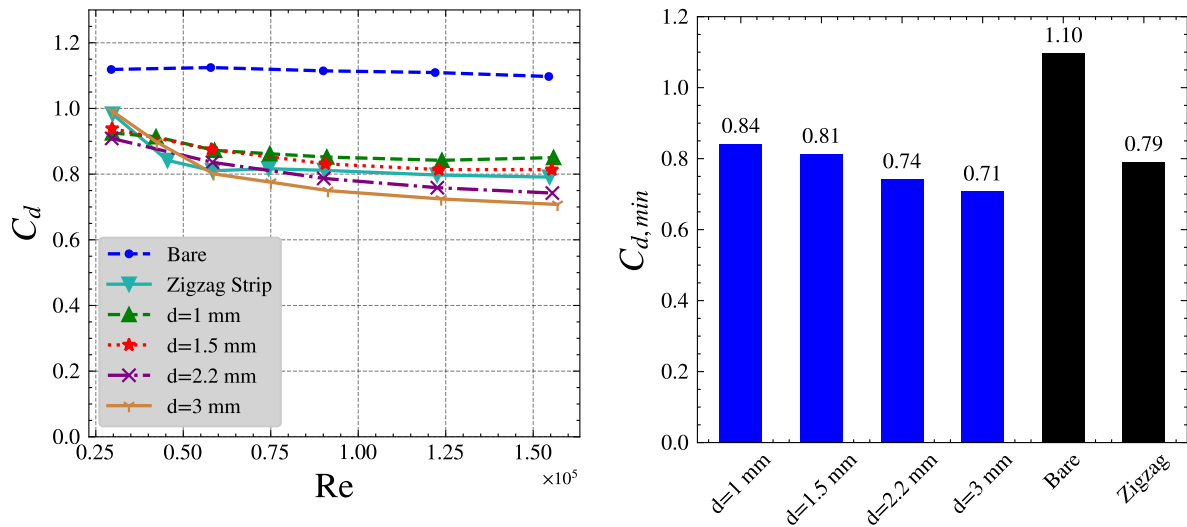
Figure 5.9a presents the drag curves for series C configurations and Figure 5.9b presents the $C_{d,min}$. With increasing diameter, the value of $C_{d,min}$ falls and the value for Re_{crit} rises. The relative positions of Re_{crit} were qualitatively ascertained using the slopes of the drag curves as explained in Section 5.2.1. An almost linear relationship is seen for the $C_{d,min}$ with polka-dot diameter.

In this case, the change in the Re_{crit} can be attested to the changing aspect ratio of the polka-dots and therefore a statement can be made about the $Re_{k,crit}$. Since the polka-dot height is kept constant, the velocity seen by the top of the polka-dots (u_k) is constant and therefore for a given free-stream velocity, the values of Re_k (formulation presented in Equation (2.5)) should also be identical for all the polka-dot configurations in series C. The measured values of Re_k for the series C configurations are presented in Table 5.1. It is seen that despite the polka-dots having the same height, an increase in the value of Re_k is seen with larger diameters for the same free stream velocity. This highlights the difference in the upstream effect of the polka-dot. The polka-dots with larger diameter are seen to accelerate the flow over them to a greater extent.

Regardless of this changing value of Re_k with polka-dot diameter, the effect of polka-dot diameter (and therefore aspect ratio) is isolated here. The polka-dots are submerged in identical flow for every value of Re measured. The changes in Re_k are attested only to the changes in the polka-dot diameter.

Table 5.1: The measured values of Re_k for each of the series C configurations ($k = 1.5$ mm, $S/d = 1.5$) at each measured cylinder Reynolds number.

Cyl.	d (mm)	Re_k	Re_k	Re_k	Re_k
		@ $Re = 0.3 \cdot 10^5$	@ $Re = 0.6 \cdot 10^5$	@ $Re = 0.9 \cdot 10^5$	@ $Re = 1.2 \cdot 10^5$
3	1	622	1233	1903	2547
9	1.5	546	1237	1869	2719
4	2.2	693	1378	2172	3021
5	3	700	1467	2357	3280



(a) The coefficient of drag plotted against Reynolds number for series A cylinders.

(b) The $C_{d,min}$ plotted against polka-dot diameter.

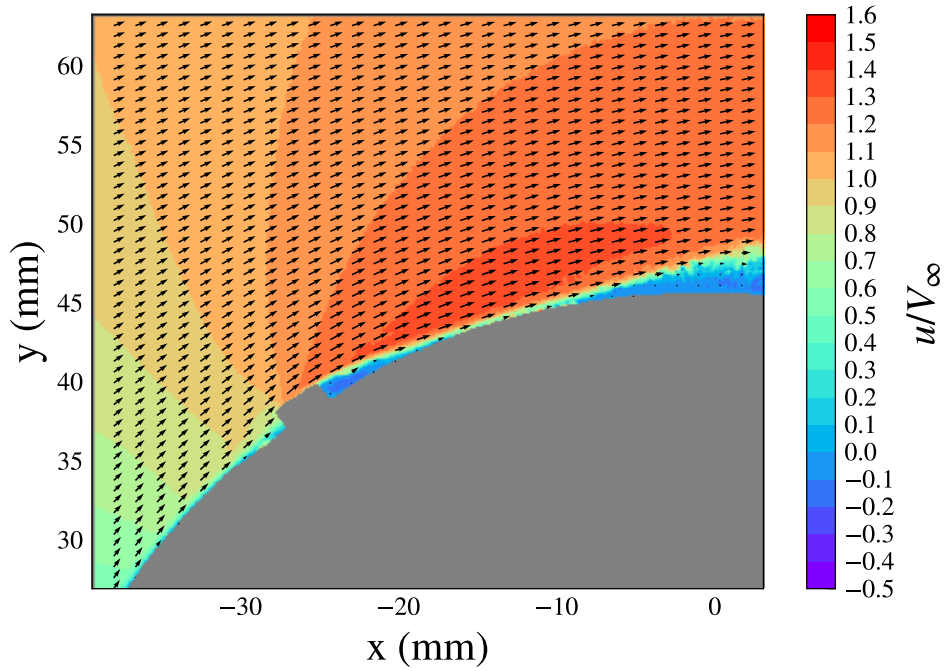
Figure 5.9: Drag data presented for Series C cylinders. Here, polka-dot diameter is varied for a constant height ($k = 1.5$ mm) and spacing ($S/d = 1.5$).

From Figure 5.9 it is seen that a greater diameter polka-dot configuration leads to a greater value of Re_{crit} for the cylinder. Furthermore, from Table 5.1 it is seen that a larger polka-dot diameter further accelerates the flow, increasing the value of Re_k for a given height of polka-dot. This leads to the conclusion that the proportional increase in polka-dot $Re_{k,crit}$ as a result of increasing polka-dot diameter is greater than the proportional increase in the value of Re_{crit} for the cylinder on which polka-dot configuration is applied. Mathematically stated, Equation (5.1) holds true for $d_1 > d_2$ where d represents the polka-dot diameter.

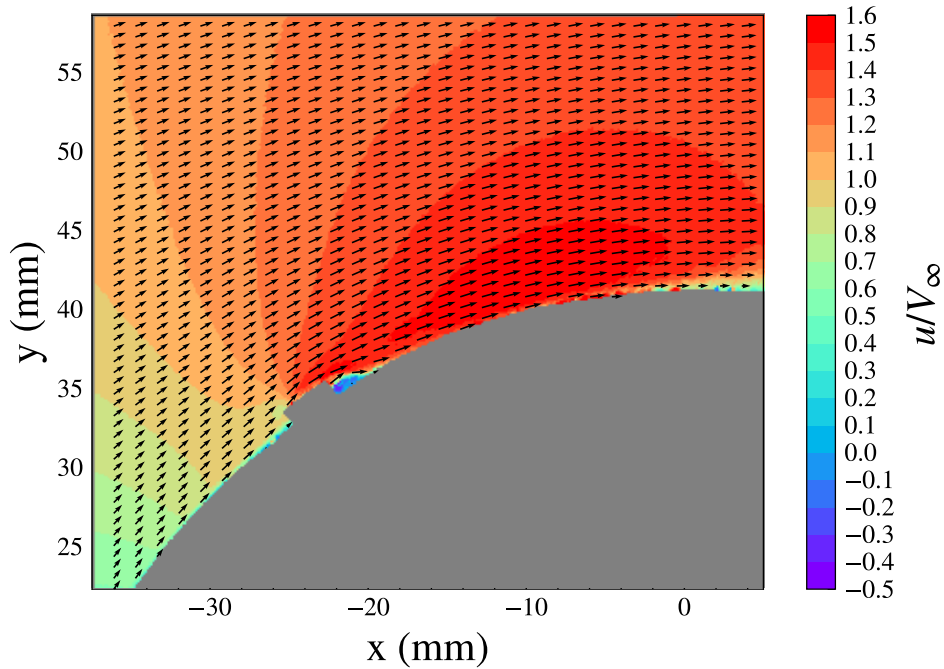
$$\frac{Re_{crit}^{d=d_1}}{Re_{crit}^{d=d_2}} < \frac{Re_{k,crit}^{d=d_1}}{Re_{k,crit}^{d=d_2}} \quad (5.1)$$

In order to gain greater insight into the effect of the of the polka-dot shape on the boundary layer, the information regarding the evolution of the boundary layer is consulted. Figure 5.10 presents the flowfield at Reynolds numbers before and after Re_{crit} over cylinder 3 ($d = 1$ mm) and 5 ($d = 3$ mm). As is presented in Figure 5.9, cylinder 3 and cylinder 5 correspond to the greater and smallest $C_{d,min}$ in series C respectively. Furthermore, as discussed above, they conversely have the lowest and the greatest Re_{crit} respectively. These two cylinders are considered as examples in order to analyse the differences in the boundary layer flow.

Due to the greater Re_{crit} of cylinder 5, at the lowest measured Reynolds number ($Re \approx 0.3 \cdot 10^5$), the C_d of cylinder 5 is seen to be greater than that of cylinder 3 by approximately 0.08. At the a higher Reynolds number ($Re \approx 1.2 \cdot 10^5$), the C_d of cylinder 3 is about 0.15 more than that of cylinder 5. Figure 5.11 presents the shape factor in the boundary layer of all the cylinders compared in Figure 5.9a. The values of the shape factor reaching values greater than 4 denote a very thick boundary layer that has either separated or is near separation. It is seen that for cylinder 3 (the green trace), the shape factor does not change much between the two Reynolds numbers. This is manifested as a very small reduction in drag between the two drag datapoints in Figure 5.9a. In contrast, the shape factor values of cylinder 5 reduces from about 8 (denoting separated flow or a thick and highly convex boundary layer) to about 1.5 (denoting a turbulent boundary layer). This is also seen in Figure 5.10b where before the drag crisis is triggered, the polka-dot works to thicken the boundary layer. In Figure 5.10b the polka dot is 'activated' and the disturbance it induces in the flow lead to a turbulent boundary layer forming.



(a) $Re = 0.3 \cdot 10^5$. The cylinder is still in precritical state and the polka-dot actually causes growth in the boundary layer since $Re_k < Re_{k,crit}$.



(b) $Re = 1.2 \cdot 10^5$. The drag crisis is triggered and the polka-dot induces turbulent flow since $Re_k > Re_{k,crit}$.

Figure 5.10: Boundary layer images of cylinder 5 before and after the drag crisis is triggered by the polka-dot.

Figure 5.12 reinforces the information presented by the shape factor plot in Figure 5.11. Before cylinder 5 sees drag crisis, a large degree of concavity is seen in the velocity profile in the boundary layer, even more so than the bare cylinder. In this flow state, the Re_k seen by the polka dot in cylinder 5 is lower than its corresponding $Re_{k,crit}$. As discussed in Section 2.3.2, under this condition, viscosity in the boundary layer is expected to inhibit the disturbance caused by the polka-dot and return the boundary layer to its original state. What is seen in Figure 5.12 is that even about

3 polka-dot diameters downstream of the dot, the subcritical boundary layer does not recover to its original state. This is seen by comparing the bare cylinder boundary with the $d = 3$ mm profile. This is manifested in the much greater shape factor due to the highly concave velocity profile that the subcritical $d = 3$ mm boundary layer exhibits.

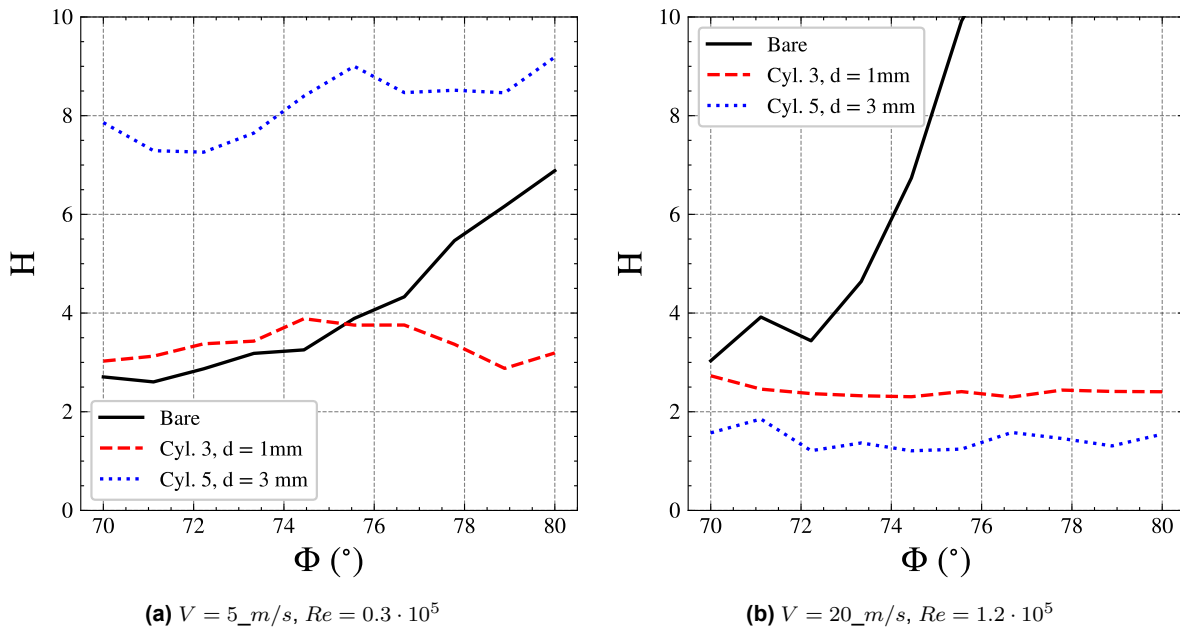


Figure 5.11: Comparison of the shape factor of the series C cylinders 3 and 5 in the range $70^\circ < \phi < 80^\circ$. The shape factor is also plotted for the bare cylinder boundary layer for reference.

Figure 5.12b meanwhile shows a highly convex boundary layer profile for cylinder 3 (now in critical flow as $Re_k > Re_{k,crit}$), a largely unchanged profile for cylinder 3, and detached flow for the bare cylinder. As expected and explained in Section 2.3.1, much greater velocity gradient near the cylinder wall corresponds to the turbulent flow seen here. While this sharp gradient contributes to a greater friction drag, greater velocity in the near-wall flow has a much greater reducing effect on the drag coefficient as seen in Figure 5.9a by delaying separation.

The shape factor of the boundary layer in cylinder 5 ($k = 1$ mm) is seen reducing from a value of about 3.5 to 2.5. This is seen in the slight increase in the convexity of the boundary layer profile in the region $0 < y < 0.5$. While the shape factor still does not strictly fall into the region that identifies transition (the value for which is around 1.5 as reported by Schlichting[27]), the increase in the convexity in the profile and reduction in the shape factor shows an increasingly effective polka-dot. This manifest in the gradual reduction of the coefficient of drag as seen in Figure 5.9a. In fact all the polka-dot element show almost the same behaviour. This is in contrary to the zigzag strip tested, wherein once $C_{d,min}$ is reached, the value of C_d remains almost constant. This difference might indicate a difference in the behaviour of the elements in the transcritical regime. Further investigation is warranted since the Reynolds number range of this research did not cover the subcritical or transcritical regime for any of the polka-dot configurations tested.

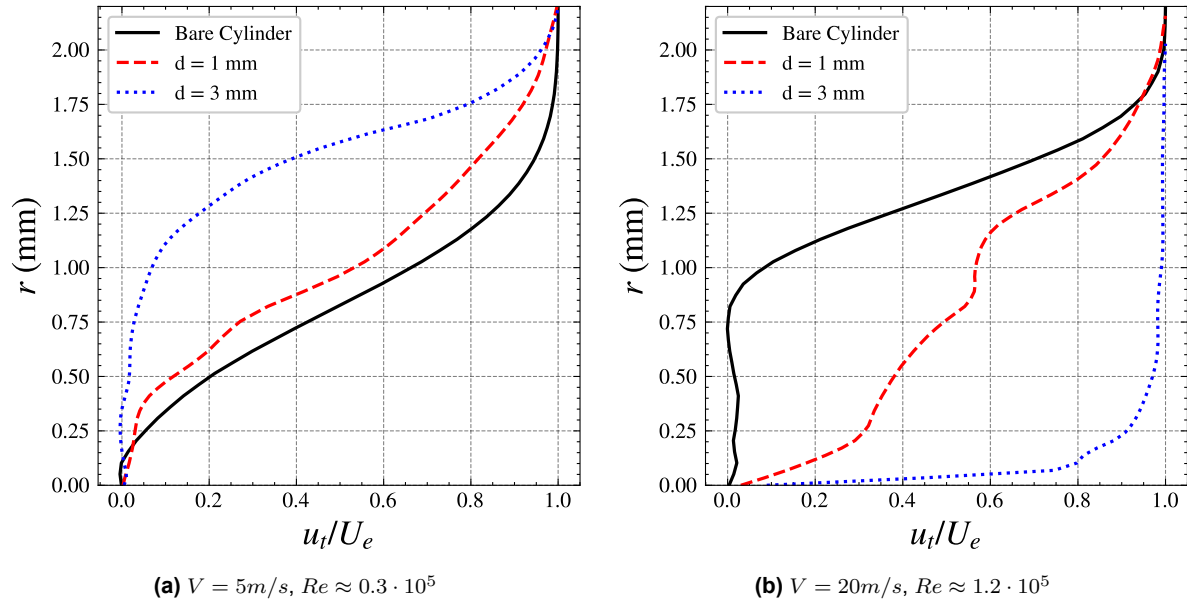


Figure 5.12: Comparison of the boundary layer profiles of cylinder 3 ($k = 1\text{ mm}$), cylinder 5 ($k = 3\text{ mm}$) and the bare cylinder at $\phi = 75^\circ$.

5.2.3. Effect of Polka-Dot Spacing

To assess the effect of polka-dot spacing, series D configurations were used. This series is comprised of the series A and B cylinders since they have identical polka-dot diameters (1.5 mm) and the same variations in polka-dot height with the difference between the series solely being the spacing (1.5 in series A and 2.5 in series B). The specifications of the configurations is presented in Table 4.4 and is repeated below for the reader's convenience.

Table 4.4 (repeated): The dimensions of polka-dot configurations in series D cylinders. The pairs of rows highlighted together correspond to the configurations where the individual polka-dots have identical height and aspect ratio such that the only change between them is the spacing.

Cyl. Nr.	k (mm)	d (mm)	AR	S/d	N (mm)
2	1.5	1.5	1	2.5	3.75
9	1.5	1.5	1	1.5	2.25
6	1	1.5	0.68	2.5	3.75
10	1	1.5	0.68	1.5	2.25
7	2.2	1.5	1.47	2.5	3.75
11	2.2	1.5	1.47	1.5	2.25
8	3	1.5	2	2.5	3.75
12	3	1.5	2	1.5	2.25

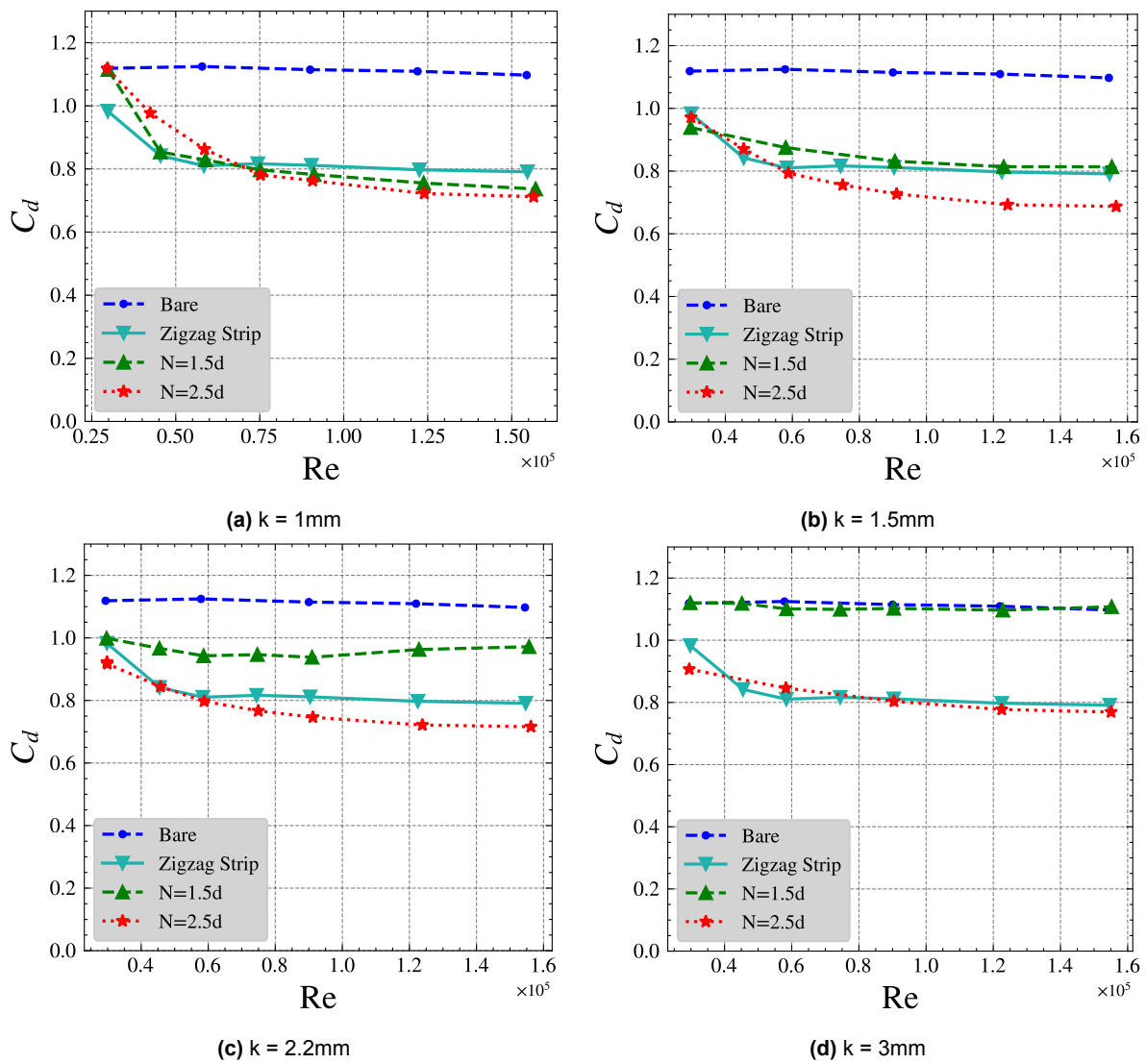


Figure 5.13: Comparison of the drag plots of the different pairs of cylinders with identical polka-dot dimensions but different polka-dot spacing. In each plot, the drag curves for the cylinder with the zigzag strip and the bare cylinder are also provided.

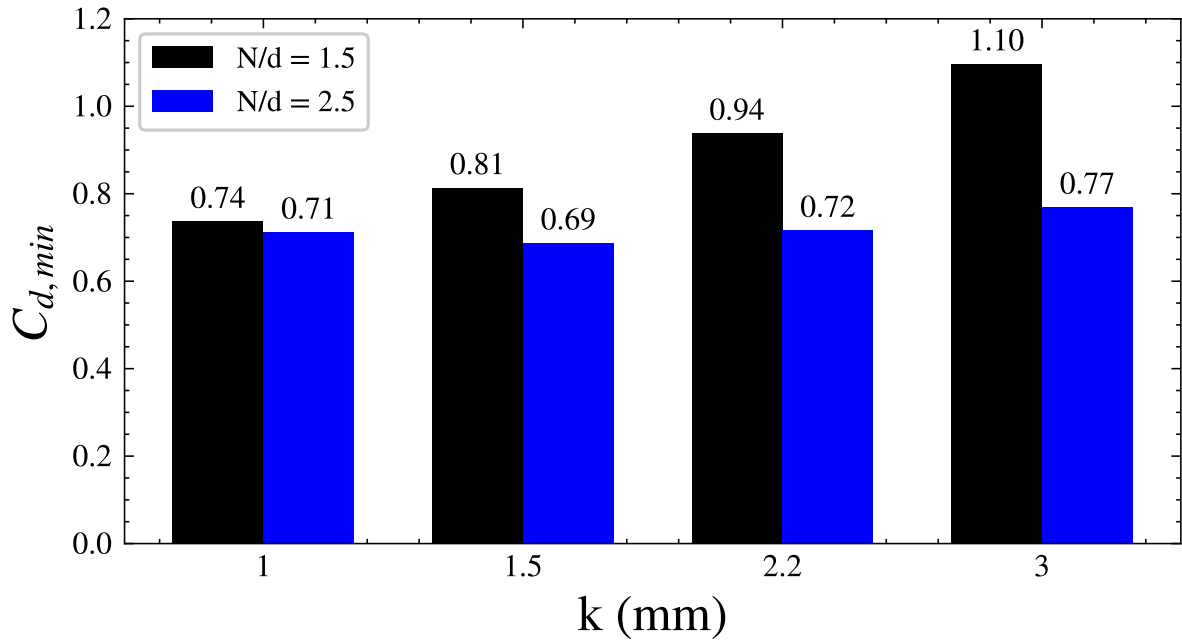


Figure 5.14: $C_{d,min}$ plotted for different polka-dot heights for series A and B cylinders.

As presented in Section 5.2.1, the $C_{d,min}$ of the cylinders generally increases with increasing polka-dot height. This is shown for both series A and series B in Figure 5.14. The exception here is cylinder 10 ($k = 1\text{mm}$ with $S/d = 2.5$ from series B). As it is further discussed in Section 5.2.1, according to Brownlie, this configuration is likely to have a lower $C_{d,min}$ than was measured in this research. Figure 5.14 clearly shows the linear trend that is followed and that cylinder 10 is an outlier.

For all four pairs of cylinders, it is seen from Figure 5.13 that the $C_{d,min}$ achieved is lower for the less dense spacing. In fact, with increasing polka-dot height, this difference grows. Figure 5.15 and Figure 5.16 shows this for the configurations with $k = 1\text{mm}$ and 1.5mm respectively by looking at the boundary layer shape factor on the cylinder surfaces. These configurations were chosen to explore this behaviour because as presented in Section 5.2.1, the tallest two polka-dot configurations in series A see flow separation earlier. This makes the $k = 2.2\text{mm}$ and $k = 3\text{mm}$ configurations unfit for comparison based on the shape factor.

Figure 5.15a shows that at the lower Reynolds number (subcritical conditions), both configurations see separation but in the non-separated region, the configuration with the closer spacing has a greater shape factor. In Figure 5.15b, both cylinders are in critical flow and have virtually identical shape factor distributions.

On the other hand, in Figure 5.16a ($k = 1.5\text{mm}$), no separation is seen but the configuration with denser spacing has a consistently greater value for shape factor in the region considered. In fact, the configuration with less dense spacing is in critical flow as the value of shape factor stays consistent about 1.4 denoting a turbulent boundary layer. In Figure 5.15b, both cylinders are in critical flow, but the configuration with denser spacing maintains a shape factor of about 1.8 while the one with less dense spacing remains at about 1.4 meaning that its boundary layer will likely separate later.

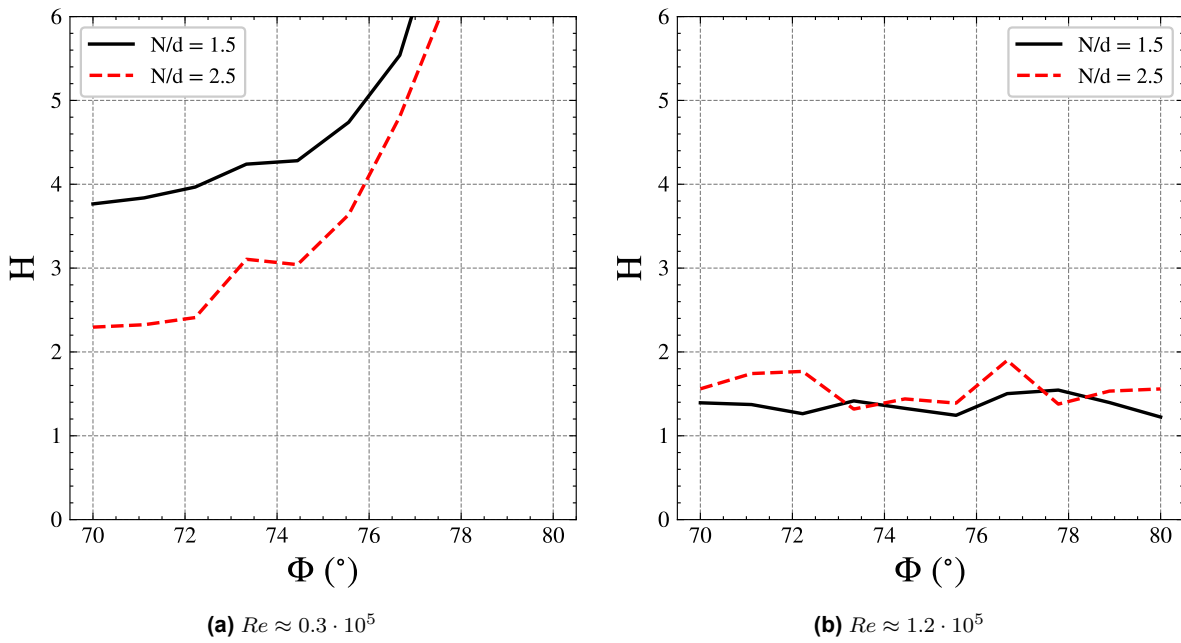


Figure 5.15: Shape factor plotted for cylinders 6 ($S/d = 2.5$) and 10 ($S/d = 1.5$). $k = 1\text{mm}$, $d = 1.5\text{mm}$.

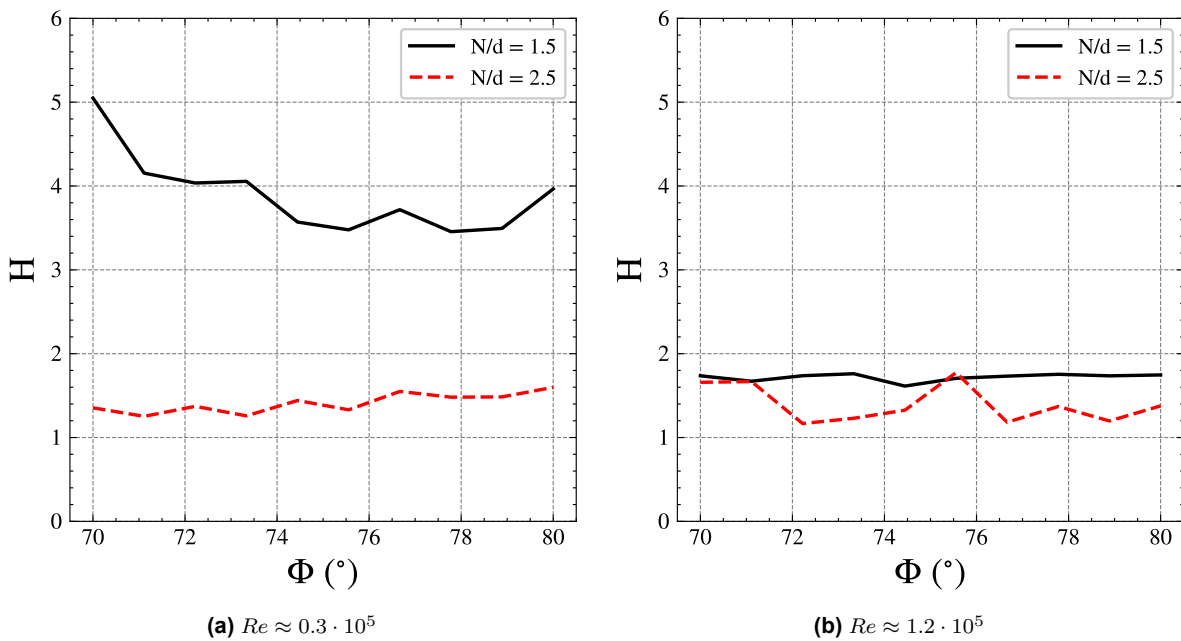


Figure 5.16: Shape factor plotted for cylinders 2 ($S/d = 2.5$) and 9 ($S/d = 1.5$). $k = 1.5\text{mm}$, $d = 1.5\text{mm}$.

Another notable effect of the change in polka-dot spacing is on the Re_k experienced by the polka-dots. As presented in Table 5.2 (series A, $S/d = 1.5$) for each cylinder Reynolds number, the increase in height causes a decrease in the value of Re_k while in Table 5.3 an increase is seen with increasing polka-dot height. This is an explanation of the smaller drag reduction seen in cylinders 11 ($k = 2.2\text{mm}$) and 12 ($k = 3\text{mm}$) of series A ($S/d = 1.5$). The effective flow velocity seen by the polka-dots is lower and therefore the tripping is much less effective. As seen in Table 5.2 and Table 5.3, the difference in Re_k caused due to difference in spacing increases. This is manifested in the flow in the form of the separation seen in cylinders 11 & 12 (shown in the flow visualisation images in Figure 5.6 and Figure 5.7).

Table 5.2: The measured values of Re_k for each of the series A configurations ($d = 1.5$ mm, $S/d = 1.5$) at each measured cylinder Reynolds number.

Cyl.	k (mm)	Re_k			
		@ $Re = 0.3 \cdot 10^5$	@ $Re = 0.6 \cdot 10^5$	@ $Re = 0.9 \cdot 10^5$	@ $Re = 1.2 \cdot 10^5$
10	1	377	1409	3139	5847
9	1.5	302	1237	3009	5737
11	2.2	281	1030	2406	4669
12	3	293	905	2165	3938

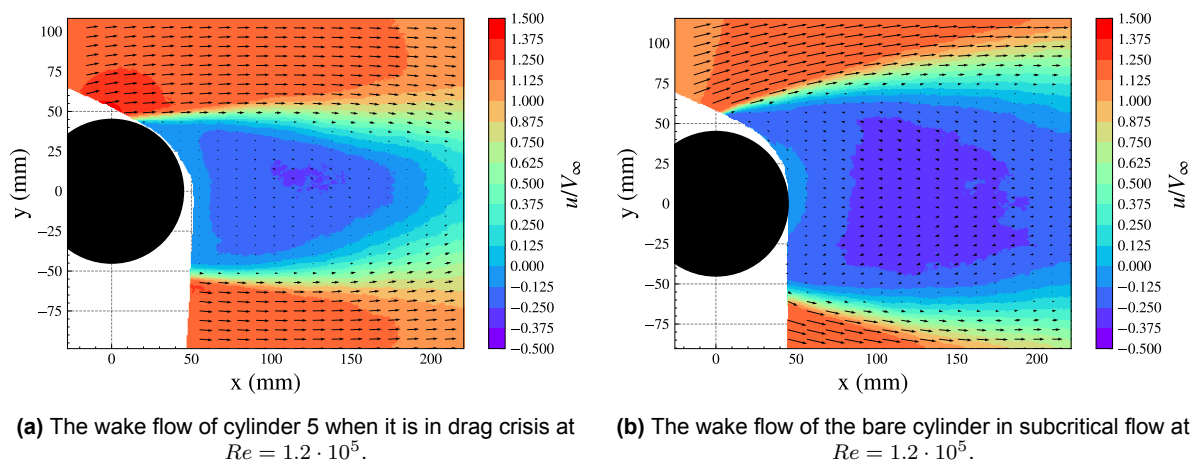
Table 5.3: The measured values of Re_k for each of the series B configurations ($d = 1.5$ mm, $S/d = 2.5$) at each measured cylinder Reynolds number.

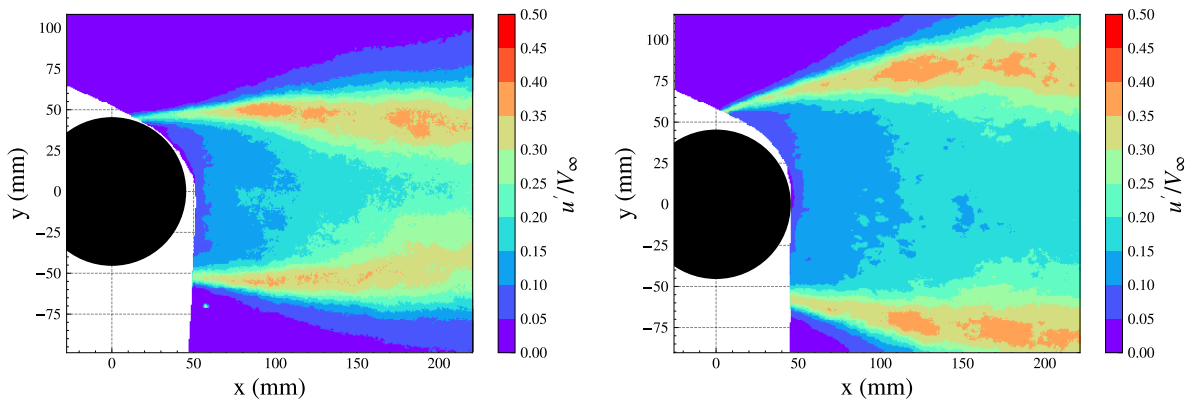
Cyl.	k (mm)	Re_k			
		@ $Re = 0.3 \cdot 10^5$	@ $Re = 0.6 \cdot 10^5$	@ $Re = 0.9 \cdot 10^5$	@ $Re = 1.2 \cdot 10^5$
6	1	400	1347	3174	5834
2	1.5	463	1311	3186	5928
7	2.2	468	1448	3262	5879
8	3	458	1222	3117	5710

5.3. Wake Width Analysis

The more delayed the boundary layer separation is, the greater the base pressure coefficient as was presented in Figure 2.14. The value of the base pressure does not vary trivially with separation location. Two reasons are put forth for this. Firstly, the potential flow pressure distribution itself is non-linear in the sinusoidal shape it follows. Secondly, the difference between the potential flow solution and the experimental distribution is dependent upon the characteristics of the viscous boundary layer that grows on the cylinder surface, which are also highly non-linear.

Along with the base pressure coefficient, another parameter that affects the pressure drag is the separation location. The later the separation takes place, the smaller the base region will be. The location of the boundary layer separation also dictates the width of the wake. As seen in, Figure 5.17 and Figure 5.18 the wake is visibly wider for the bare cylinder than for cylinder 5 which has the lowest recorded coefficient of drag in this research.

**Figure 5.17:** The averages streamwise wake velocities of the bare cylinder ($C_d = 1.1$) and cylinder 5 ($C_d = 0.7$). The bare cylinder has a visually wider wake that extends further downstream.



(a) The wake turbulence intensity of cylinder 5 when it is in drag crisis at $Re = 1.2 \cdot 10^5$.

(b) The wake turbulence intensity of the bare cylinder in subcritical flow at $Re = 1.2 \cdot 10^3$.

Figure 5.18: The streamwise wake flow standard deviation of the bare cylinder ($C_d = 1.1$) and cylinder 5 ($C_d = 0.7$). The bare cylinder has a visually wider wake that extends further downstream.

In fact, when the wake-width is computed for all the cylinders and Reynolds numbers using the method presented in Section 4.5.2, it is seen to have a high linear correlation to the coefficient of drag. Regardless of where the wake-width is sampled in the measurement domain, a high correlation is found with C_d .

Table 5.4: The r^2 scores for the regression of the C_d with the wake width measured at different downstream locations of the cylinder.

Sampling Location Downstream of Cylinder TE (x/D)	Regression r^2 Value
0.08	0.87
0.26	0.90
0.45	0.89
0.63	0.88
0.82	0.91
1.00	0.89
1.19	0.91
1.37	0.91
1.56	0.88
1.74	0.89

Table 5.4 presents the r^2 values for the different linear regressions carried out on the data. It is seen that the regression has a score of around 0.9 for all sampling locations. While there is a clear causation between the wake width of the flow and the coefficient of drag due to the fact that the wake width is directly related to base region size, the linearity in the correlation is of note.

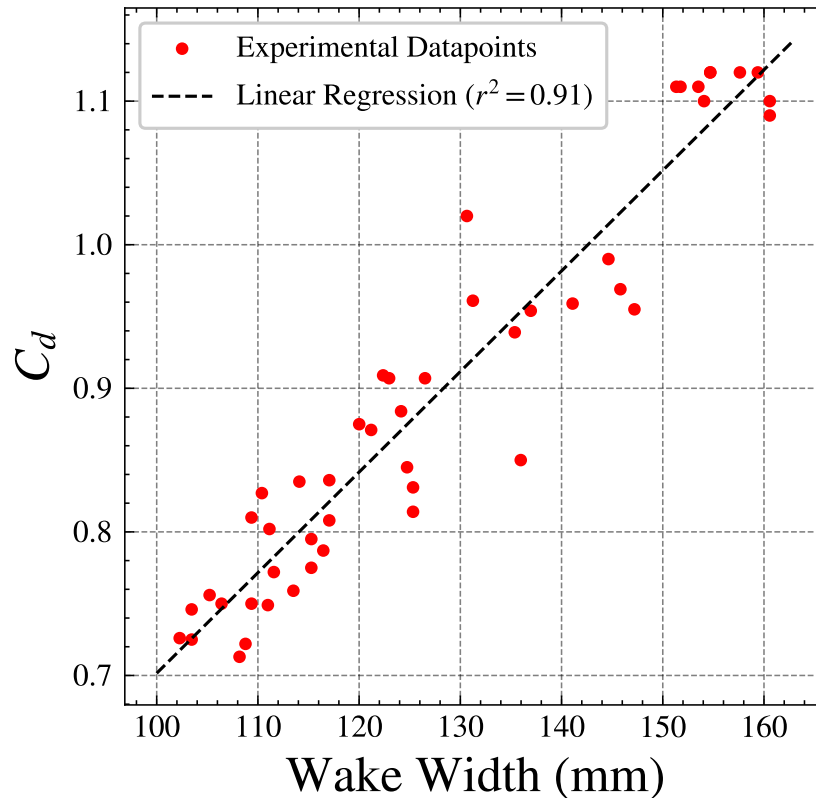


Figure 5.19: C_d plotted against the wake width sampled 0.82 diameters downstream of the cylinder trailing edge. $r^2 = 0.91$

Figure 5.19 presents the experimental data points and the regression for $x/D = 0.82$. The r^2 value of 0.91 signifies that the width of the base region can explain 91% of the variation in the coefficient of drag.

Figure 5.20 and Figure 5.21 visualise the wake flow as it varies with Reynolds number. A clear narrowing of the wake is seen, the largest of which takes place between $Re = 0.3 \cdot 10^5$ and $Re = 0.65 \cdot 10^5$. Additionally, the wake is seen to reduce in width by the end of the domain with increasing Reynolds number.

In order to further demonstrate the change seen in the topology of the wake, the wake profiles are extracted from Figure 5.21 and overlaid in Figure 5.22. These wake profiles were measured as the distance between the locations of maximum peak intensity in the wake flow as presented in Section 4.5.2 The C_d measurements for the same Re values are shown in Figure 5.23.

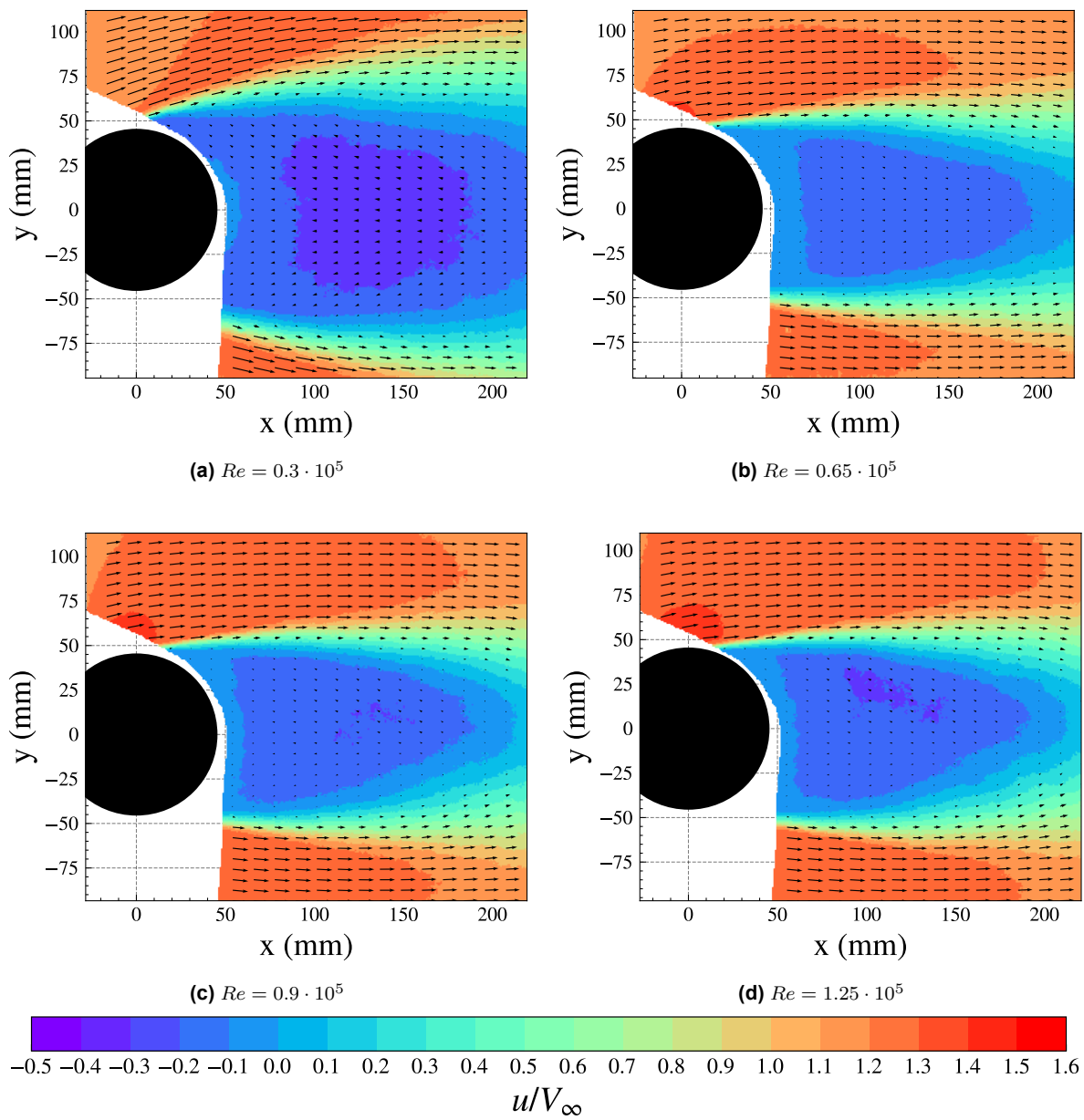


Figure 5.20: The mean streamwise wake velocity plots of cylinder 10 ($k = 1$ mm, $d = 1.5$ mm, $S/d = 1.5$).

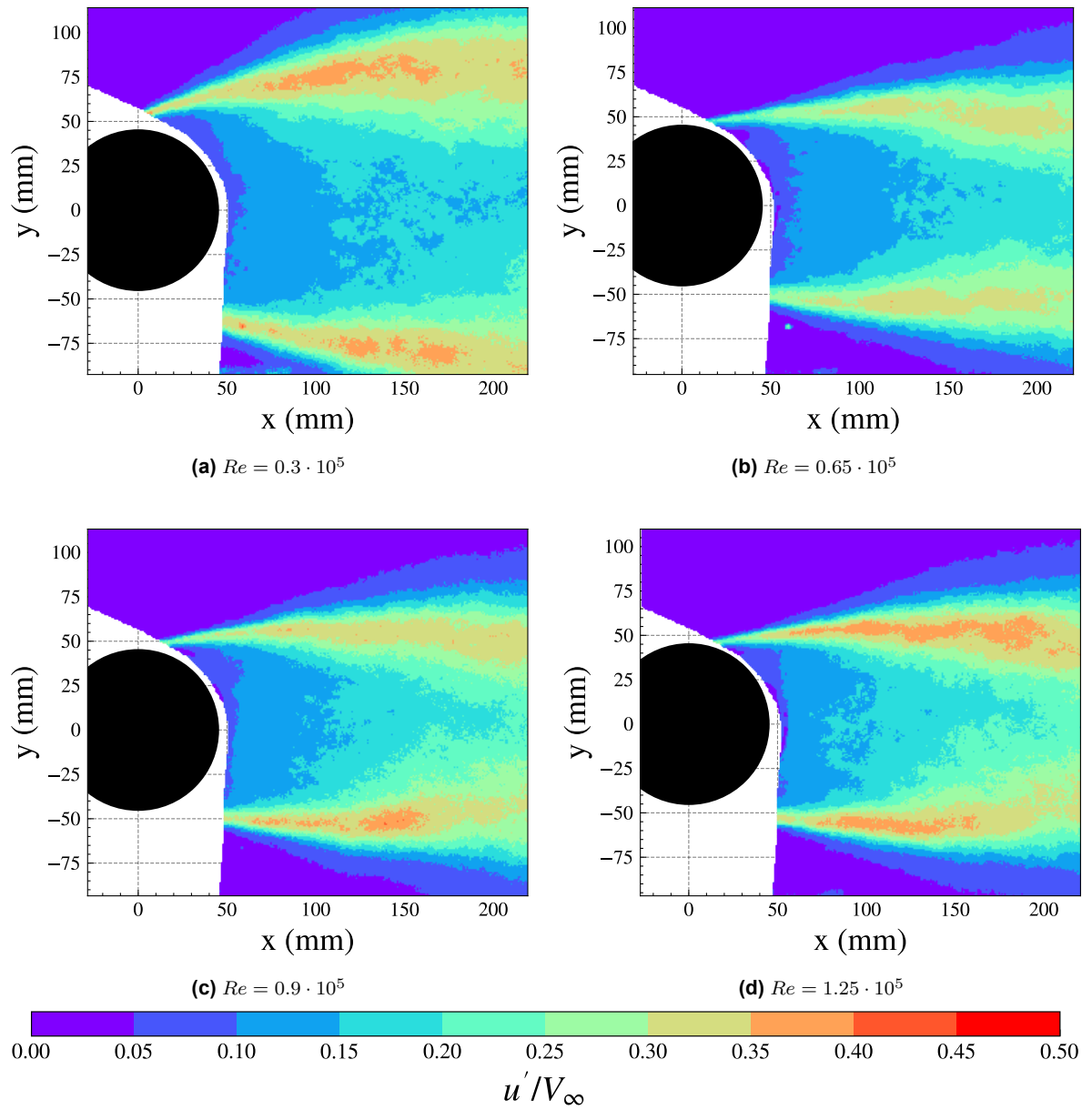


Figure 5.21: The standard deviation of streamwise wake velocity of cylinder 10 ($k = 1$ mm, $d = 1.5$ mm, $S/d = 1.5$).

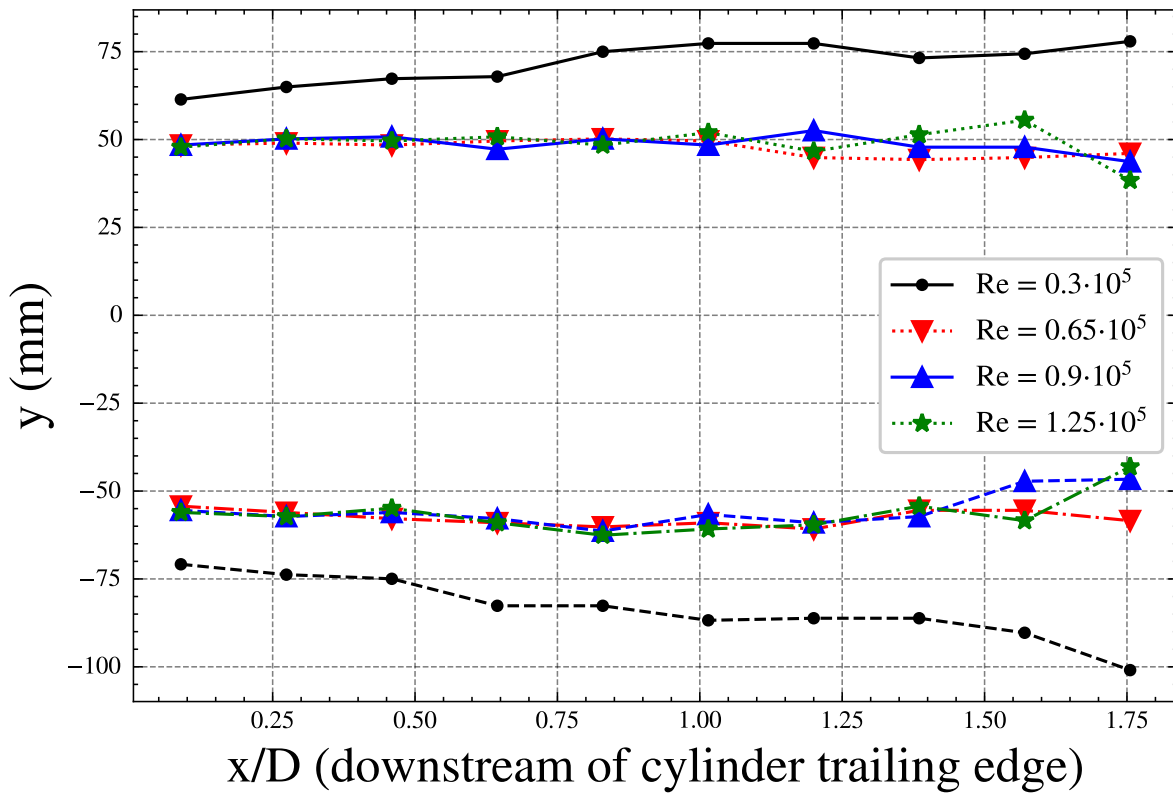


Figure 5.22: The wake profile for cylinder 10 ($k = 1\text{mm}$, $d = 1.5\text{mm}$, $S/d = 1.5$) as it varies throughout the measurement regime.

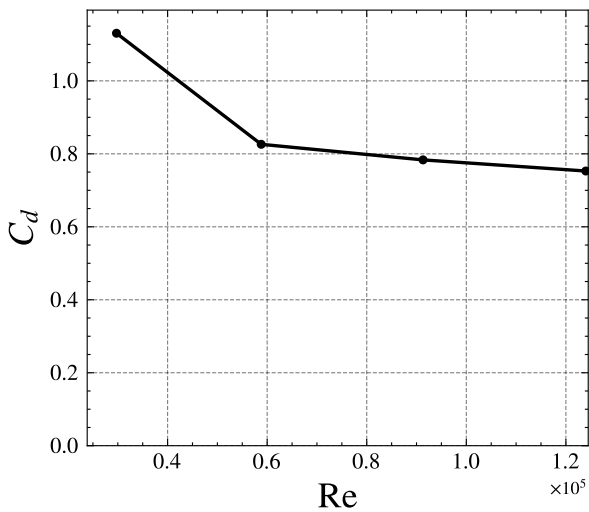


Figure 5.23: C_d plotted against Reynolds numbers for cylinder 10. The range of the Reynolds numbers matches that of Figure 5.22.

Between the two lower Reynolds numbers, a large change in C_d is seen and this is also manifested as a large change in wake width. In fact, at the most downstream end of the domain, the $Re = 0.3 \cdot 10^5$ (black) wake outline is still seen expanding. The other three data points see a small change between them in C_d and therefore their wake profiles are also nearly identical in terms of the width measured. The key difference between them is the wake topology at the downstream end of the domain. The $Re = 0.65 \cdot 10^5$ (red) plot, corresponding to the second highest C_d , sees no contraction in the wake. The $Re = 1.25 \cdot 10^5$ plot (green), corresponding to the smallest C_d , on the other hand exhibits the wake profile rapidly contracting after $x/D = 1.5$.

Given that the difference between the wake topologies of the last three data points is characterised in the far downstream end of the measurement domain, it is highly likely that the further downstream section of the wake also provides greater insight into the flow effect of the drag crisis and the polka-dot induced tripping. A larger wake domain, until at least 3-4 cylinder diameters downstream, would be more apt to perform the regression performed in this section. Through this it is also plausible that the r^2 value of the regression presented in Figure 5.19 is improved upon. In

the current domain size, it is exemplified by Figure 5.22 that there are data points wherein despite there being a difference measured C_d the wake width is measured to be the same. A larger wake measurement domain is likely to better these results as it will provide further insight into the wake flow and the off the surface pressure recovery the flow sees.

6

Conclusions and Recommendation

The purpose of this research was to investigate the use of polka-dots as discrete roughness elements in order to reduce the drag of cylinders in cross-flow. The regime of interest was identified as the pre-drag crisis subcritical regime where the drag coefficient of a bare cylinder was found to be approximately 1.1. 11 different polka-dot configurations were considered. Between the 11 configurations, polka-dot height, diameter and spacing were varied. For each cylinder configuration, the boundary layer and wake flow were imaged using PIV, and the loads on the cylinder were measured using a balance. From the boundary layer images, the boundary layer shape factor was calculated, from the wake images the wake width was obtained, and from the loads the coefficient of drag was extracted. Using these results, an analysis of the effects of the different polka-dot parameters was made possible.

This chapter presents the conclusions drawn from the results and recommendations for further research. First, Section 6.1 presents the key findings from the research and the conclusions that relate back to the research questions. Then, recommendations for future work in the field of polka-dot tripping and cylinder drag reduction are presented in Section 6.2.

6.1. Conclusions

This section addresses the research questions with the conclusions drawn from this research. These are all on the basis of the results presented in Chapter 5.

Of the 11 polka-dot configurations tested, all were successful in triggering a drag reduction in the domain of interest, with the exception of cylinder 8 for which the polka-dots caused flow separation. For almost every cylinder, Re_{crit} was found to have a value of Re below the tested regime. Therefore, it was impossible to characterise the values of Re_{crit} . Based on the gradient of the drag curve at the lower end of the regime, though, the relative positions of Re_{crit} were ascertained for the configurations. This allowed for a comparative analysis of the effect of polka-dot parameters on Re_{crit} as is presented below.

Furthermore, the polka-dot configurations were seen to cause a drag crisis with behaviour different from that of a bare cylinder. When a bare cylinder enters the drag crisis and reaches $C_{d,min}$, the drag coefficient is seen to abruptly level off. In comparison, the C_d of the polka-dot-triggered drag crisis tends to continue to decrease with Reynolds number. This is exemplified in Figure 6.1 where cylinder 10 (the cylinder with the sharpest kink in the drag crisis) is seen to have a gradually further decreasing value of drag coefficient even after the initial sharp decrease in C_d .

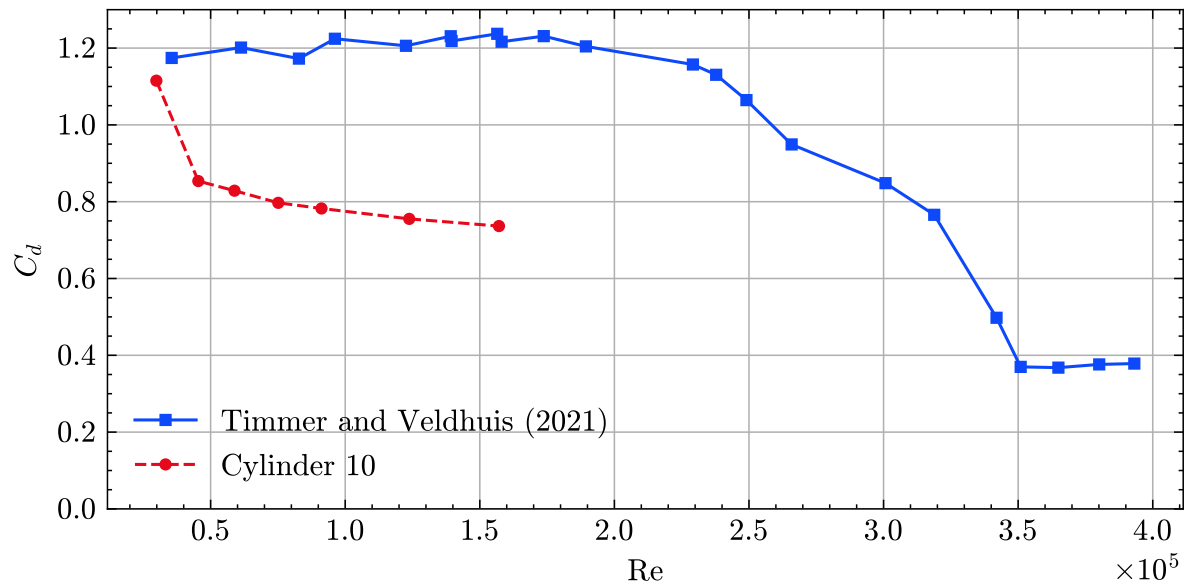


Figure 6.1: The drag curve of a bare cylinder (obtained from Timmer and Veldhuis [33]) plotted together with that of cylinder 10. While the bare cylinder sees a levelling-off of the C_d at $C_{d,min}$, the polka-dot equipped cylinder sees a further decline in its C_d .

Before a more detailed list of conclusions are presented in the subsections below, they are tabulated in Table 6.1. It presents a schematic overview of the effect of the polka-dot geometric parameters on the drag characteristics and the boundary layer flow of the cylinders.

Table 6.1: The effect of polka-dot geometrical parameters on the drag and flow characteristics of the cylinder.

Effect of increasing	on $C_{d,min}$	on Re_k for given Re	on Re_{crit}	on separation tendency
Polka-dot diameter	Decreasing	Decreasing	Increasing	No effect seen
Polka-dot height	Increasing	Dependent on spacing	Decreasing	Increasing
Polka-dot spacing	Decreasing	Increasing	Increasing	Decreasing

6.1.1. Effect of Polka-Dot Height

The general trend seen in the analysis of the series A and B cylinders is that cylinders with shorter polka-dots have a greater value for Re_{crit} . Furthermore, shorter polka-dots also led to a lower value for $C_{d,min}$. In fact, within the 4 cylinders from series A, it was found that for each millimetre of height reduced there was an approximate decrease in the $C_{d,min}$ of 0.2.

The trend of reducing Re_{crit} with increasing polka-dot height was, as expected theoretically, based on the ability of the polka-dot to introduce high-energy flow into the near-wall decelerated flow. Since at lower Reynolds numbers there is a thicker boundary layer, the shorter polka-dots do not see the greater energy flow in the higher parts of the boundary layer and therefore do not trip the flow. As the Reynolds number increases and the boundary layer thickness decreases, they start to see a greater energy flow and are 'activated' as tripping elements.

A trend of increasing $C_{d,min}$ with increasing roughness element height was also seen. This was expected on the basis of the work of Brownlie [8]. The earlier the drag crisis is triggered, the greater the value of $C_{d,min}$ is. This is explained by the fact that once within their critical regime, shorter polka-dots decrease the shape factor of the boundary layer to a greater extent and lead to a more convex boundary layer velocity profile.

6.1.2. Effect of Polka-Dot Diameter

By changing polka-dot diameter for the same height and normalised spacing, the effect of polka-dot shape (aspect ratio) was isolated. Through this, it was seen that cylinders equipped with polka-dots of greater diameter had a greater Re_{crit} . Additionally, increasing diameter was seen to increase the value of Re_k by accelerating the flow of the cylinder. Therefore from this it is also concluded that a greater polka-dot diameter leads to a greater $Re_{k,crit}$. Additionally, the greater value of $Re_{k,crit}$ was correlated to a lower measured value of $C_{d,min}$.

While series C is the only series where the effect of aspect ratio was isolated, the same trend of increasing Re_{crit} with increasing polka-dot height was also seen in series A & B. Within series A & B it is likely that this was compounded with the effect of reducing height as well to cause the decrease in $C_{d,min}$ as was discussed in the previous section.

Through imaging the boundary layer after the tripping of each of the elements, it was seen that the wider polka-dots led to a more effective tripping by reducing the shape factor of the boundary layer by a greater amount which explains the lower value of drag coefficient attained. It is seen that while $Re_k < Re_{k,crit}$, the polka-dots have an effect of increasing the velocity deficit in the lower part of the laminar boundary layer. Therefore, the polka-dots will likely encourage separation in their subcritical regime. Due to this, the conclusion can be drawn that the value of C_d for the polka-dot equipped cylinders is likely greater than that of the bare cylinder for $Re < Re_{crit}$.

6.1.3. Effect of Polka-Dot Spacing

The effect of polka-dot spacing was seen to be in line with the findings of von Doenhoff and Braslow [34]. The configurations with the spacing of 1.5 diameters were observed to have a lower value for Re_{crit} than their counterparts with 2.5 diameters of spacing. Additionally, in accordance with the findings of Brownlie the narrower spacing also led to a greater value for $C_{d,min}$ [8]. It was seen that the polka-dot spacing had an effect how the flow is accelerated over the polka-dot. For a wider spacing, greater values of Re_k were seen than in the narrower spacing. In addition, for the narrower spacing, an increase in height was seen to decrease the value of Re_k for the same cylinder Re , while in the wider spacing, an increase was seen. This effect was not fully characterised due to only two levels of spacing considered and further research is strongly suggested into the effect of polka-dot spacing.

Another key finding was that for polka-dots with greater height ($k = 2.2$ mm and $k = 3$ mm in this experiment), the configuration with narrower spacing led to flow separation earlier than that of the wider spacing. In fact for $k = 3$ mm, at $S/d = 1.5$, flow separation was seen from the position of the polka-dots onward. This was not seen in the $S/d = 2.5$ configuration with $k = 3$ mm. For the smaller heights ($k = 1$ mm and $k = 1.5$ mm), it was observed that the reduction in boundary layer shape factor was greater in the narrower spacing.

Closer polka-dot spacing, therefore, leads to a lower $Re_{k,crit}$ but at the same time makes the flow more susceptible to separation in taller polka-dot configurations. This happens as it is found that the wider spacing leads to a greater introduction of energy into the near wall flow. Lower spacing thus also leads to a smaller overall drag reduction in the cylinder.

6.1.4. Wake Flow Analysis

As is expected due to the drag being largely pressure driven, a large correlation was found between the wake width and the coefficient of drag measured. A key finding was that the relationship between the measured wake width and the measured coefficient of drag was well modelled by a linear regression. In fact, throughout the wake domain imaged, regardless of where in the wake the width was sampled, the linear fit was seen to predict the drag coefficient well (minimum $r^2 = 0.87$ and maximum $r^2 = 0.91$ depending on sampling location). The correlation score remained largely unchanged whether the wake width was sampled in the near wake where the wake boundary is

more clear or further downstream where there is a relatively diffused wake boundary.

This points to the fact that the wake width alone can be used as a way to estimate the drag coefficient of a cylinder. This can be especially useful in the case where a wake rake cannot be reliably used due to the presence of another object in the wake. It was observed that measuring wake width even less than 10% of the cylinder diameter downstream of the trailing edge can give a relatively accurate estimation of the cylinder drag.

Finally, it was seen that for cylinders with coefficients of drag very close together, a key difference was how the wake tapers off with the pressure recovery of the wake flow. It is likely that if a larger part of the wake geometry is considered, a better correlation to coefficient of drag can be ascertained.

6.2. Recommendations

Based on this research and the insight from it, a number of recommendations are put forth in this section. They include recommendations for carrying out similar experimental work based on the drawbacks of the setup in this research and also further topics that should be explored based on the results of this research.

Further Research into Polka-Dot Geometry and Spacing Effects

This research attempted to delve into the effect of polka-dot height, diameter and spacing at the same time, therefore allowing a high level understanding of the effect of each of these parameters. It is necessary to look further into each parameter with greater detail. A tomographic imaging of a spanwise section of the cylinder would also allow for much greater insight into the tripping process. Furthermore, more geometrical parameters could be considered such as the eccentricity of the polka-dot shape, i.e., an assessment of the effect of elliptical polka-dots.

Solutions for Cylinder Buffeting

Due to the cyclic nature of the aerodynamic loads on the cylinder, a large amount of oscillation was observed. This was particularly the case for the bare cylinder but was also noticeable for the cylinders equipped with roughness elements. The buffeting made PIV measurements impossible for $V_\infty = 5 \text{ m/s}$ ($Re \approx 1.5 \cdot 10^5$).

It is strongly suggested that future experimental studies of cylinder flow should consider some method of damping the vibration. One solution is to attach the cylinder at both ends rather than the cantilever arrangement used in this research. This would require two force balances or another innovative way of measuring the load on the cylinder.

More Involved Wake Analysis

As mentioned in the analysis of the wake flow, different rates of narrowing were seen in the downstream wake. It was also postulated that a larger wake imaging domain would likely lead to a better method of estimating coefficient of drag from the wake geometry. For example, adding another parameter such as the streamwise wake length would add valuable insight into the analysis. The wake width indirectly measures the size of the base region whereas the wake streamwise length would be a measure of distance to wake pressure recovery. In the current setup, the size of the imaged domain was insufficient for the measurement of the wake streamwise length.

Cylinder Inclination, Yaw and Motion

In this study, only right cylinders in planar flow were considered. In the implementation on a skin-suit, the polka-dots would have more complex and varied inflow conditions. Firstly, cylinder inclination is an important consideration, i.e., inflow that is not within the x-y plane as depicted in Figure 2.2. Secondly, yawed flow is also critical to consider, i.e., inflow such that the stagnation

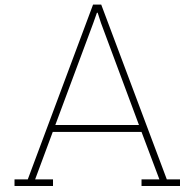
point of the cylinder is not necessarily at $\phi = 0^\circ$. Both these changes in the inflow condition are more representative of flow conditions that the limbs of an ice-skater would see. Lastly, the oscillatory motion of the limbs of a skater are likely to have hysteretic effects on the drag experienced by them. The effect of dynamic inflow conditions on polka-dots and their effect on tripping is an important consideration in the exploration of polka-dots as a drag reduction mechanism in sports.

References

- [1] E. Achenbach. "Distribution of local pressure and skin friction around a circular cylinder in cross-flow up to $Re = 5 \times 10^6$ ". en. In: *Journal of Fluid Mechanics* 34.4 (Dec. 1968). Publisher: Cambridge University Press, pp. 625–639. ISSN: 1469-7645, 0022-1120. DOI: 10.1017/S0022112068002120. URL: <https://www.cambridge.org/core/journals/journal-of-fluid-mechanics/article/distribution-of-local-pressure-and-skin-friction-around-a-circular-cylinder-in-crossflow-up-to-re-5-106/2699AB7EE2292DF574E70654DB1C3E13> (visited on 06/04/2023).
- [2] J.D. Anderson. *Fundamentals of aerodynamics*. English. Fifth edition. Anderson series. Section: xxiii, 1106 pages : illustrations ; 24 cm. New York: McGraw-Hill, 2011. ISBN: 978-0-07-339810-5 978-0-07-128908-5. URL: <http://catdir.loc.gov/catdir/enhancements/fy1002/2009048907-t.html> (visited on 06/04/2023).
- [3] J.B. Barlow, W.H. Rae, and A. Pope. *Low-speed wind tunnel testing*. eng. 3rd ed. OCLC: 39335023. New York: Wiley, 1999. ISBN: 978-0-471-55774-6.
- [4] P. W. Bearman. "On vortex shedding from a circular cylinder in the critical Reynolds number régime". en. In: *Journal of Fluid Mechanics* 37.3 (July 1969). Publisher: Cambridge University Press, pp. 577–585. ISSN: 1469-7645, 0022-1120. DOI: 10.1017/S0022112069000735. URL: <https://www.cambridge.org/core/journals/journal-of-fluid-mechanics/article/on-vortex-shedding-from-a-circular-cylinder-in-the-critical-reynolds-number-regime/45280DB5F5B99193906471C6BD396809> (visited on 06/04/2023).
- [5] V. M. Bozhkov, L. E. Vasil'ev, and S. V. Zhigulev. "Transverse subsonic flow past a cylinder". en. In: *Fluid Dynamics* 15.2 (Mar. 1980), pp. 303–306. ISSN: 1573-8507. DOI: 10.1007/BF01342626. URL: <https://doi.org/10.1007/BF01342626> (visited on 05/29/2023).
- [6] R. Brown. "Drag reduction of bluff bodies in tandem: Size and spacing effects on cylinders and cyclists". en. In: (2023). URL: <https://repository.tudelft.nl/islandora/object/uuid%3A3585b154-26e1-4bd0-abfc-f98caf3eb112> (visited on 08/22/2023).
- [7] L Brownlie. "Aerodynamic drag reduction in winter sports: The quest for "free speed"". en. In: *Proceedings of the Institution of Mechanical Engineers, Part P: Journal of Sports Engineering and Technology* 235.4 (Dec. 2021). Publisher: SAGE Publications, pp. 365–404. ISSN: 1754-3371. DOI: 10.1177/1754337120921091. URL: <https://doi.org/10.1177/1754337120921091> (visited on 06/30/2023).
- [8] L.W. Brownlie. "Aerodynamic characteristics of sports apparel". eng. Publisher: Simon Fraser University. PhD thesis. Simon Fraser University, 1992. URL: <https://summit.sfu.ca/item/4486> (visited on 04/03/2023).
- [9] L.W. Brownlie and C.R. Kyle. "Evidence that skin suits affect long track speed skating performance". en. In: *Procedia Engineering*. ENGINEERING OF SPORT CONFERENCE 2012 34 (Jan. 2012), pp. 26–31. ISSN: 1877-7058. DOI: 10.1016/j.proeng.2012.04.006. URL: <https://www.sciencedirect.com/science/article/pii/S1877705812016190> (visited on 06/30/2023).
- [10] C. Demartino and F. Ricciardelli. "Aerodynamics of nominally circular cylinders: A review of experimental results for Civil Engineering applications". en. In: *Engineering Structures* 137 (Apr. 2017), pp. 76–114. ISSN: 01410296. DOI: 10.1016/j.engstruct.2017.01.023. URL: <https://linkinghub.elsevier.com/retrieve/pii/S0141029617300974> (visited on 04/03/2023).
- [11] A.G. Eiffel. "Sur la résistance des sphères dans l'air en mouvement". fr. In: *Comptes rendus hebdomadaires des séances de l'Académie des sciences* 155 (1912).

- [12] A. Fage and V. M. Falkner. *Further experiments on the flow around a circular cylinder*. en. Technical Report. Accepted: 2014-10-21T12:03:18Z. H. M. Stationery Office, 1931. URL: <https://reports.aerade.cranfield.ac.uk/handle/1826.2/1416> (visited on 06/03/2023).
- [13] O Flachsbart. *Handbook Experimental-physik 4 part-2*. Tech. rep. Leipzig, 1932, p. 316.
- [14] J. H. Gerrard and M.J. Lighthill. "The wakes of cylindrical bluff bodies at low Reynolds number". In: *Philosophical Transactions of the Royal Society of London. Series A, Mathematical and Physical Sciences* 288.1354 (Jan. 1997). Publisher: Royal Society, pp. 351–382. DOI: 10.1098/rsta.1978.0020. URL: <https://royalsocietypublishing.org/doi/10.1098/rsta.1978.0020> (visited on 05/29/2023).
- [15] I. Konopov et al. "Aerodynamic and comfort characteristics of a double layer knitted fabric assembly for high speed winter sports". en. In: *Procedia Engineering*. The Engineering of Sport 8 - Engineering Emotion 2.2 (June 2010), pp. 2837–2843. ISSN: 1877-7058. DOI: 10.1016/j.proeng.2010.04.075. URL: <https://www.sciencedirect.com/science/article/pii/S1877705810003292> (visited on 06/30/2023).
- [16] C. Lyon, M. Selig, and A. Broeren. "Boundary layer trips on airfoils at low Reynolds numbers". In: *35th Aerospace Sciences Meeting and Exhibit*. _eprint: <https://arc.aiaa.org/doi/pdf/10.2514/6.1997-511>. American Institute of Aeronautics and Astronautics, Jan. 1997. DOI: 10.2514/6.1997-511. URL: <https://arc.aiaa.org/doi/abs/10.2514/6.1997-511> (visited on 07/26/2023).
- [17] C.D. Meinhart, S.T. Wereley, and J.G. Santiago. "A PIV Algorithm for Estimating Time-Averaged Velocity Fields". en. In: *Journal of Fluids Engineering* 122.2 (June 2000), pp. 285–289. ISSN: 0098-2202, 1528-901X. DOI: 10.1115/1.483256. URL: <https://asmedigitalcollection.asme.org/fluidsengineering/article/122/2/285/459651/A-PIV-Algorithm-for-Estimating-TimeAveraged> (visited on 04/12/2023).
- [18] C.E.K. van Moll. "An Experimental Analysis on the Effect of Surface Roughness on Cylinder Aerodynamics". MA thesis. TU Delft, Aug. 2014.
- [19] L. Oggiano et al. "A Review on Skin Suits and Sport Garment Aerodynamics: Guidelines and State of the Art". en. In: *Procedia Engineering* 60 (2013), pp. 91–98. ISSN: 18777058. DOI: 10.1016/j.proeng.2013.07.018. URL: <https://linkinghub.elsevier.com/retrieve/pii/S1877705813010692> (visited on 04/03/2023).
- [20] M. Raffel et al. *Particle Image Velocimetry: A Practical Guide*. en. Cham: Springer International Publishing, 2018. ISBN: 978-3-319-68851-0 978-3-319-68852-7. DOI: 10.1007/978-3-319-68852-7. URL: <https://link.springer.com/10.1007/978-3-319-68852-7> (visited on 04/11/2023).
- [21] D.P. Rizzetta and M.R. Visbal. "Direct Numerical Simulations of Flow Past an Array of Distributed Roughness Elements". en. In: *AIAA Journal* 45.8 (Aug. 2007), pp. 1967–1976. ISSN: 0001-1452, 1533-385X. DOI: 10.2514/1.25916. URL: <https://arc.aiaa.org/doi/10.2514/1.25916> (visited on 04/03/2023).
- [22] I. Rodríguez et al. "On the flow past a circular cylinder from critical to super-critical Reynolds numbers: Wake topology and vortex shedding". en. In: *International Journal of Heat and Fluid Flow* 55 (Oct. 2015), pp. 91–103. ISSN: 0142727X. DOI: 10.1016/j.ijheatfluidflow.2015.05.009. URL: <https://linkinghub.elsevier.com/retrieve/pii/S0142727X15000557> (visited on 06/21/2023).
- [23] R. P. J. O. M. van Rooij and W. A. Timmer. "Roughness Sensitivity Considerations for Thick Rotor Blade Airfoils". In: *Journal of Solar Energy Engineering* 125.4 (Nov. 2003), pp. 468–478. ISSN: 0199-6231. DOI: 10.1115/1.1624614. URL: <https://doi.org/10.1115/1.1624614> (visited on 07/19/2023).
- [24] A. Roshko. "Experiments on the flow past a circular cylinder at very high Reynolds number". en. In: *Journal of Fluid Mechanics* 10.3 (May 1961), pp. 345–356. ISSN: 0022-1120, 1469-7645. DOI: 10.1017/S0022112061000950. URL: https://www.cambridge.org/core/product/identifier/S0022112061000950/type/journal_article (visited on 04/03/2023).

- [25] T. Sarpkaya, M. Isaacson, and J. V. Wehausen. "Mechanics of Wave Forces on Offshore Structures". In: *Journal of Applied Mechanics* 49.2 (June 1982), pp. 466–467. ISSN: 0021-8936. DOI: 10.1115/1.3162189. URL: <https://doi.org/10.1115/1.3162189> (visited on 05/30/2023).
- [26] A. Schaffarczyk et al. "Aerodynamic Benefits by Optimizing Cycling Posture". In: *Applied Sciences* 12 (Aug. 2022), p. 8475. DOI: 10.3390/app12178475.
- [27] H. Schlichting and K. Gersten. *Boundary-Layer Theory*. en. Berlin, Heidelberg: Springer, 2017. ISBN: 978-3-662-52917-1 978-3-662-52919-5. DOI: 10.1007/978-3-662-52919-5. URL: <http://link.springer.com/10.1007/978-3-662-52919-5> (visited on 07/24/2023).
- [28] A.K. Skeide et al. "The significant impact of ribs and small-scale roughness on cylinder drag crisis". en. In: *Journal of Wind Engineering and Industrial Aerodynamics* 202 (July 2020), p. 104192. ISSN: 01676105. DOI: 10.1016/j.jweia.2020.104192. URL: <https://linkinghub.elsevier.com/retrieve/pii/S0167610520301021> (visited on 04/03/2023).
- [29] S. Suryanarayanan et al. "Effect of pressure gradients on the different stages of roughness induced boundary layer transition". en. In: *International Journal of Heat and Fluid Flow* 86 (Dec. 2020), p. 108688. ISSN: 0142727X. DOI: 10.1016/j.ijheatfluidflow.2020.108688. URL: <https://linkinghub.elsevier.com/retrieve/pii/S0142727X20304446> (visited on 04/03/2023).
- [30] E. Szechenyi. *Simulation of high reynolds numbers on a cylinder in a wind tunnel tests: Simulation de nombres de reynolds aelevaes sur un cylindre en soufflerie*. fr. Google-Books-ID: 6lonyAEACAAJ. ONERA, 1974.
- [31] S. Taneda. "Experimental Investigation of the Wake behind a Sphere at Low Reynolds Numbers". In: *Journal of the Physical Society of Japan* 11.10 (Oct. 1956). Publisher: The Physical Society of Japan, pp. 1104–1108. ISSN: 0031-9015. DOI: 10.1143/JPSJ.11.1104. URL: <https://journals.jps.jp/doi/10.1143/JPSJ.11.1104> (visited on 05/29/2023).
- [32] A. Thom. *An investigation of fluid flow in two dimensions*. en. Technical Report. Accepted: 2014-10-21T12:03:37Z. H. M. Stationery Office, 1928. URL: <https://reports.aerade.cranfield.ac.uk/handle/1826.2/1474> (visited on 07/02/2023).
- [33] W. A. Timmer and L. Veldhuis. "The Impact of Skinsuit Zigzag Tape Turbulators on Speed Skating Performance". en. In: *Applied Sciences* 11.3 (Jan. 2021), p. 988. ISSN: 2076-3417. DOI: 10.3390/app11030988. URL: <https://www.mdpi.com/2076-3417/11/3/988> (visited on 04/03/2023).
- [34] A.E. Von Doenhoff and A.L. Braslow. "The Effect of Distributed Surface Roughness on Laminar Flow". en. In: *Boundary Layer and Flow Control*. Elsevier, 1961, pp. 657–681. ISBN: 978-1-4832-1323-1. DOI: 10.1016/B978-1-4832-1323-1.50005-1. URL: <https://linkinghub.elsevier.com/retrieve/pii/B9781483213231500051> (visited on 04/03/2023).
- [35] C Wieselbergers. *New Data on the Laws of Fluid Resistance*. 19930080855. Gottingen: NASA, Jan. 1922. URL: <https://ntrs.nasa.gov/citations/19930080855> (visited on 06/03/2023).
- [36] C.H.K. Williamson and A. Roshko. "Vortex formation in the wake of an oscillating cylinder". en. In: *Journal of Fluids and Structures* 2.4 (July 1988), pp. 355–381. ISSN: 08899746. DOI: 10.1016/S0889-9746(88)90058-8. URL: <https://linkinghub.elsevier.com/retrieve/pii/S0889974688900588> (visited on 04/03/2023).
- [37] M. M. Zdravkovich. *Flow around circular cylinders: a comprehensive guide through flow phenomena, experiments, applications, mathematical models, and computer simulations*. Oxford science publications. Oxford ; New York: Oxford University Press, 1997. ISBN: 978-0-19-856396-9 978-0-19-856561-1.
- [38] Y. Zhang, A. van Zuijlen, and G. van Bussel. "The MEXICO rotor aerodynamic loads prediction: ZigZag tape effects and laminar-turbulent transition modeling in CFD". en. In: *Journal of Wind Engineering and Industrial Aerodynamics* 168 (Sept. 2017), pp. 152–163. ISSN: 0167-6105. DOI: 10.1016/j.jweia.2017.06.002. URL: <https://www.sciencedirect.com/science/article/pii/S0167610516307176> (visited on 07/26/2023).



Boundary Layer Flow Contours

This chapter contains the boundary layer flow images of all 12 cylinders tested. Each figure presents 4 images corresponding to the measured Reynolds numbers. The contour shown is the x-direction velocity normalised with the free stream velocity (u/V_∞). The overlaid vectors show the direction and magnitude of local velocity.

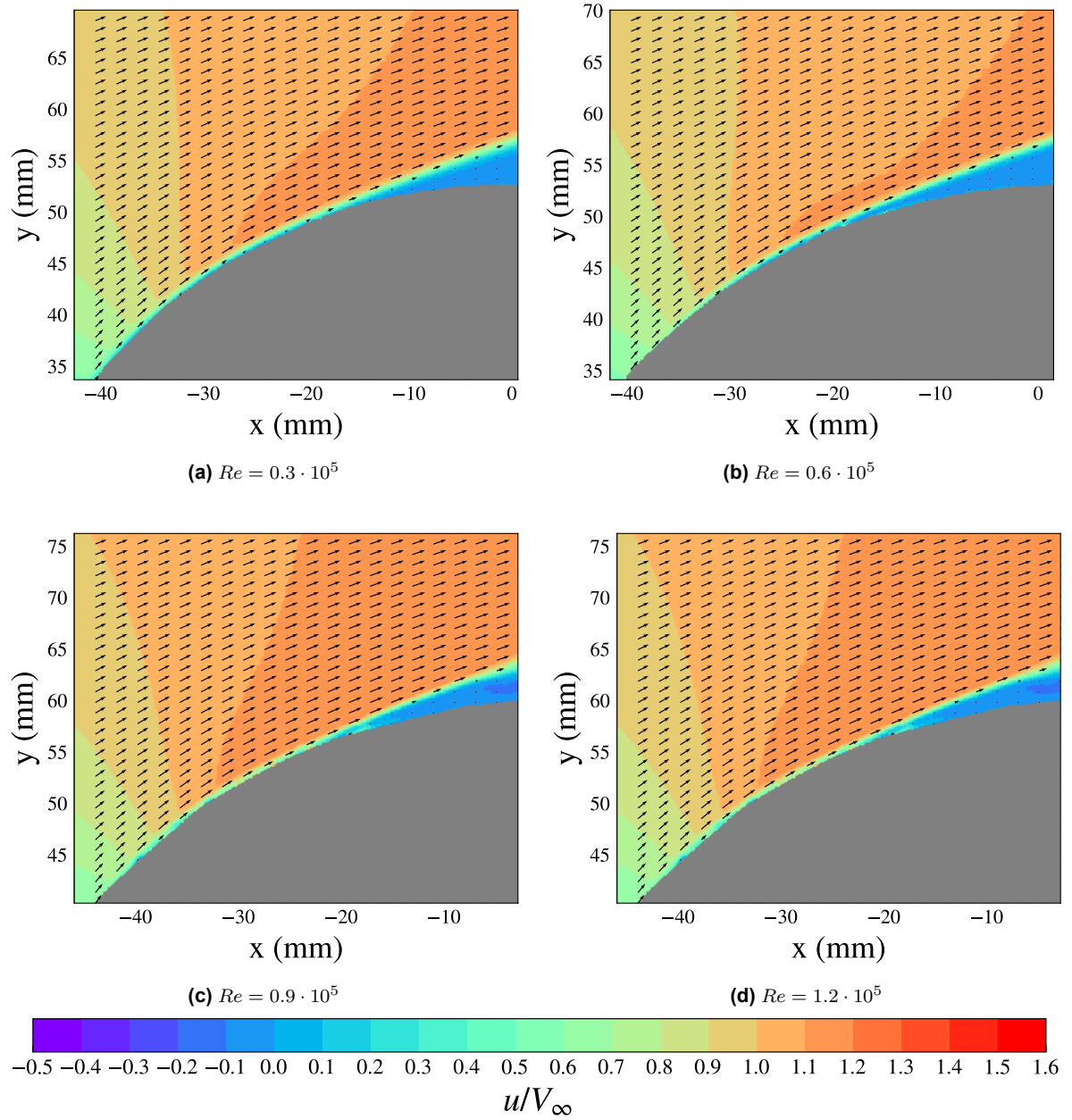


Figure A.1: Bare cylinder (cylinder 1).

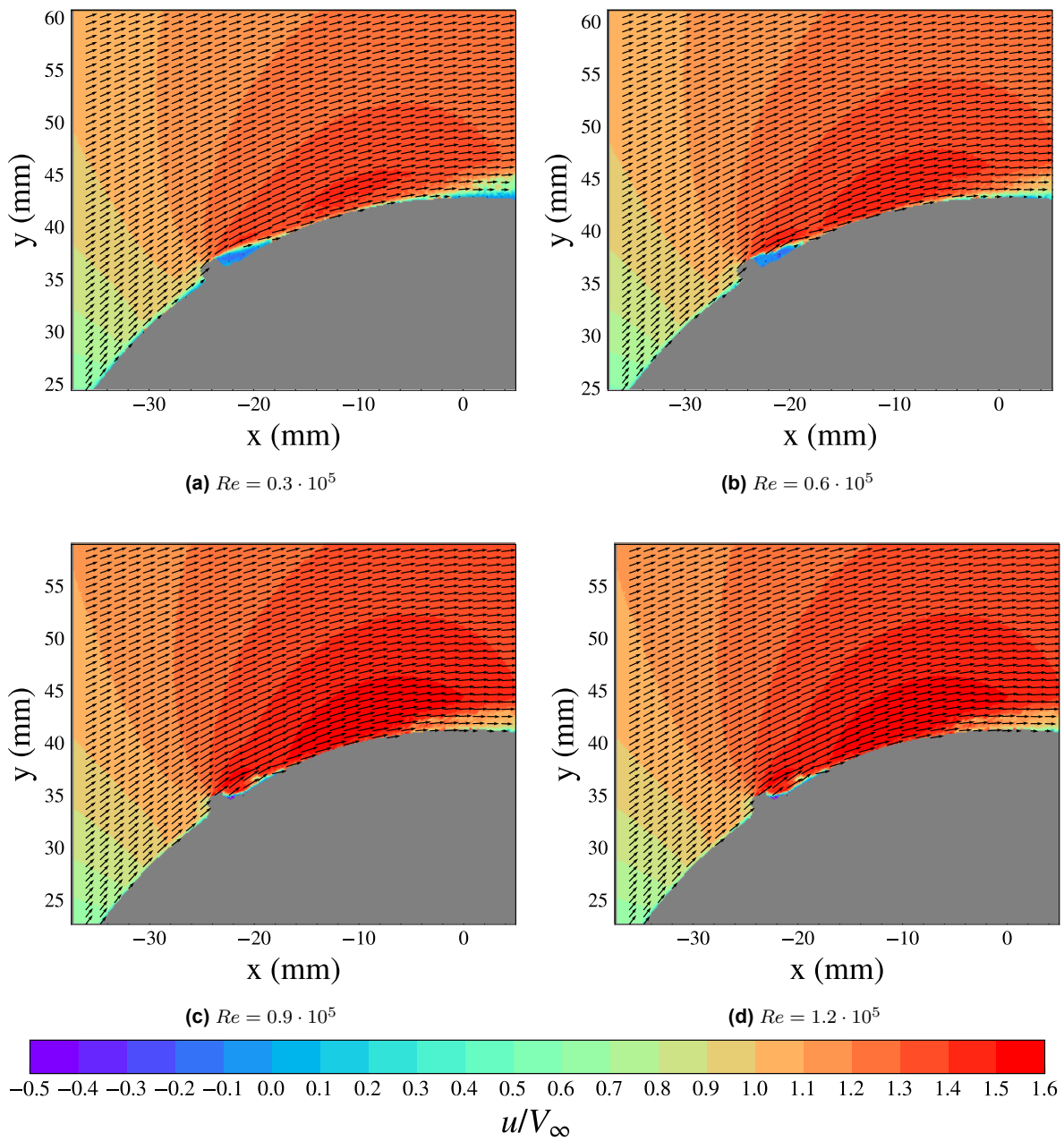


Figure A.2: Cylinder 2. $d = 1.5$ mm, $k = 1.5$ mm, $S/d = 2.5$

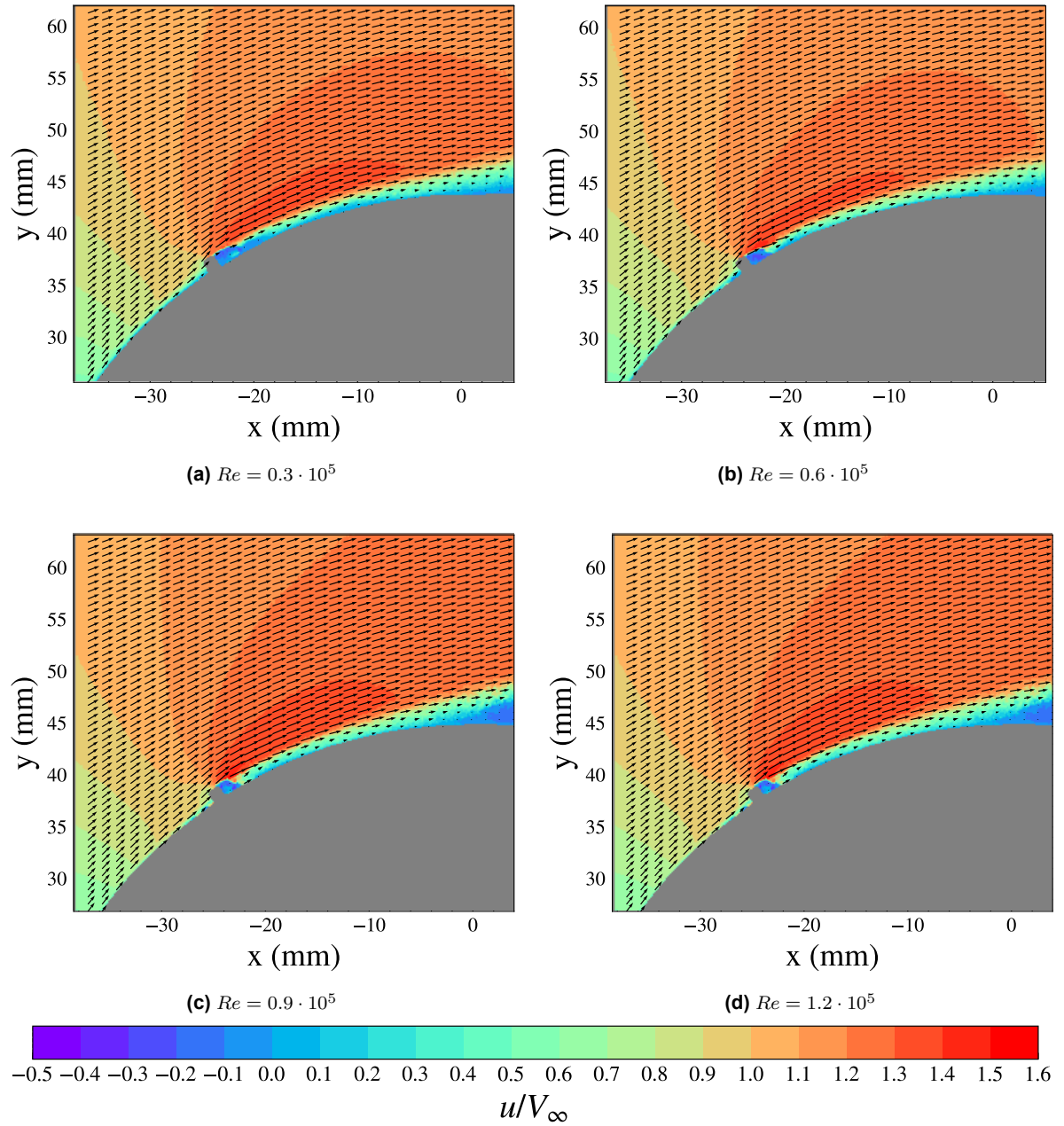


Figure A.3: Cylinder 3. $d = 1$ mm, $k = 1.5$ mm, $S/d = 1.5$

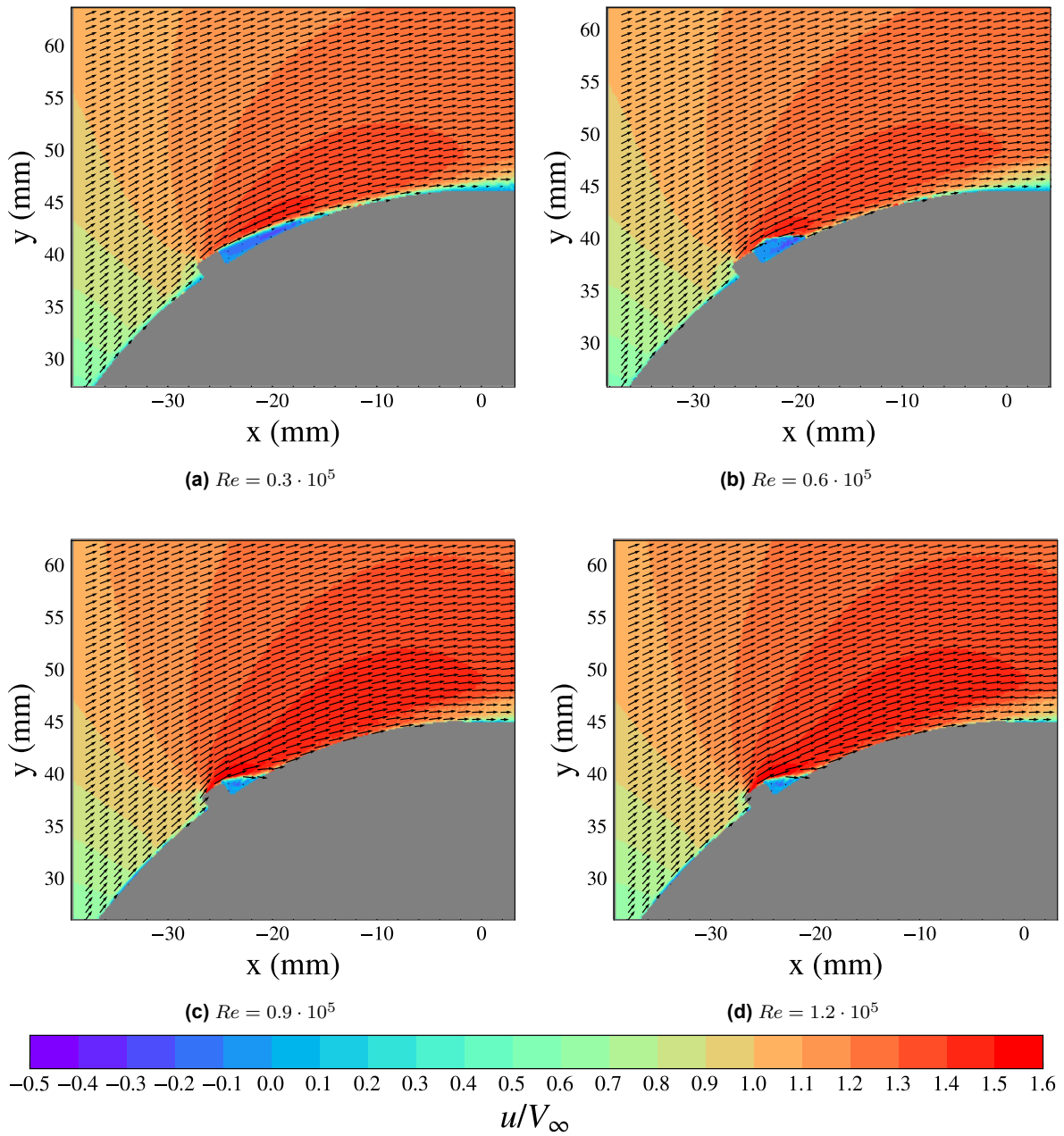


Figure A.4: Cylinder 4. $d = 2.2$ mm, $k = 1.5$ mm, $S/d = 1.5$

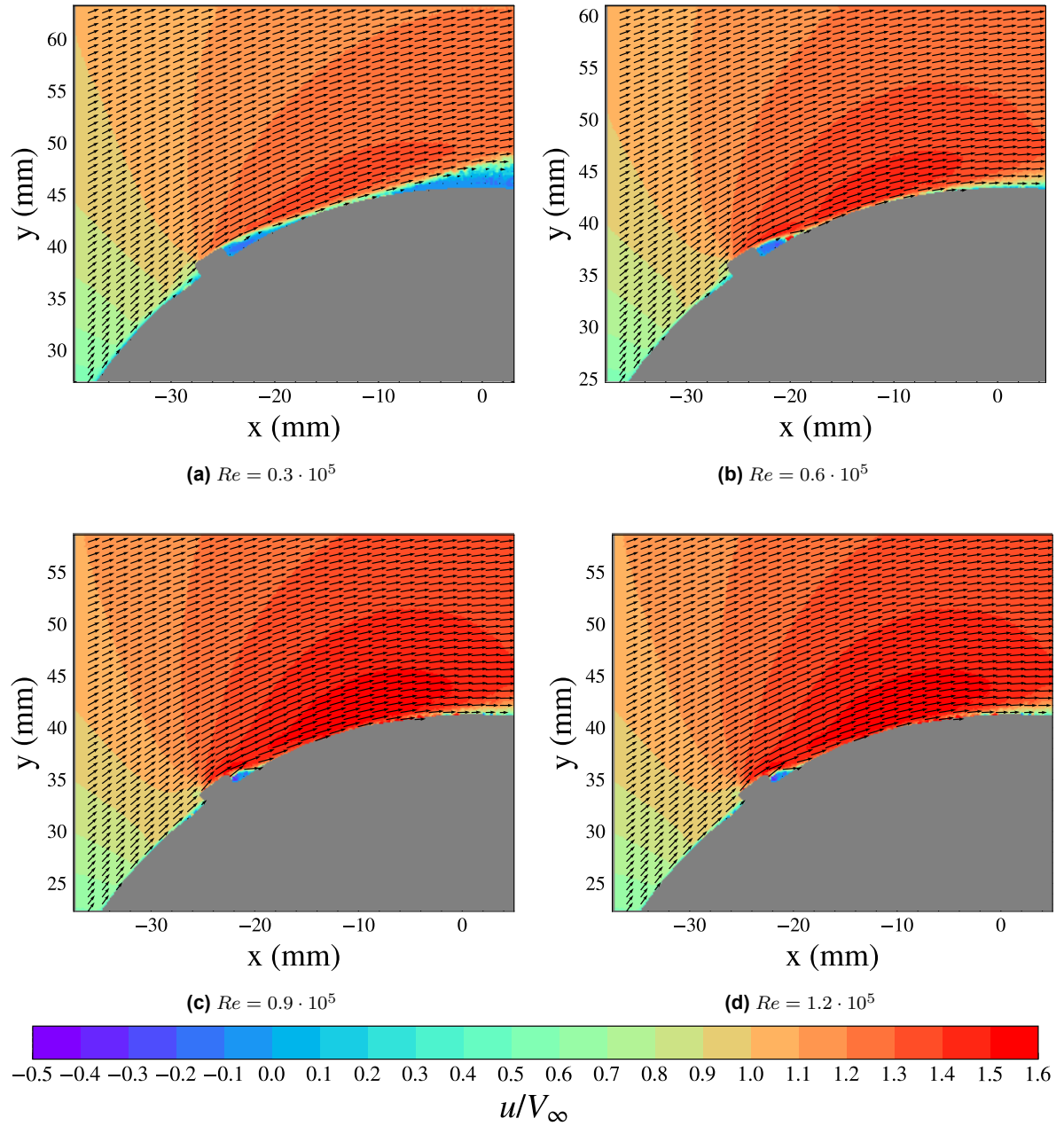


Figure A.5: Cylinder 5. $d = 2.2$ mm, $k = 3$ mm, $S/d = 1.5$

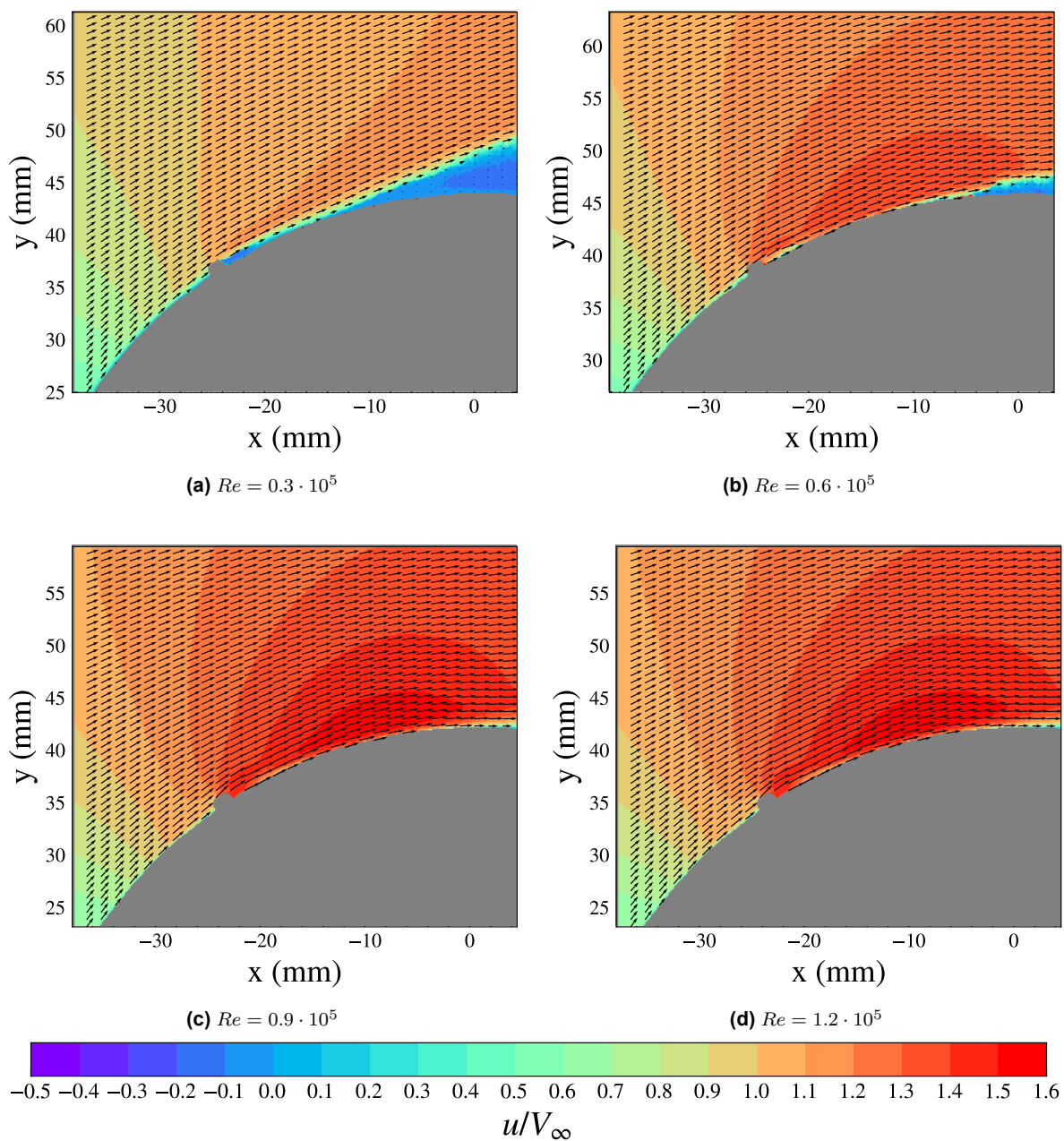


Figure A.6: Cylinder 6. $d = 1.5$ mm, $k = 1$ mm, $S/d = 2.5$

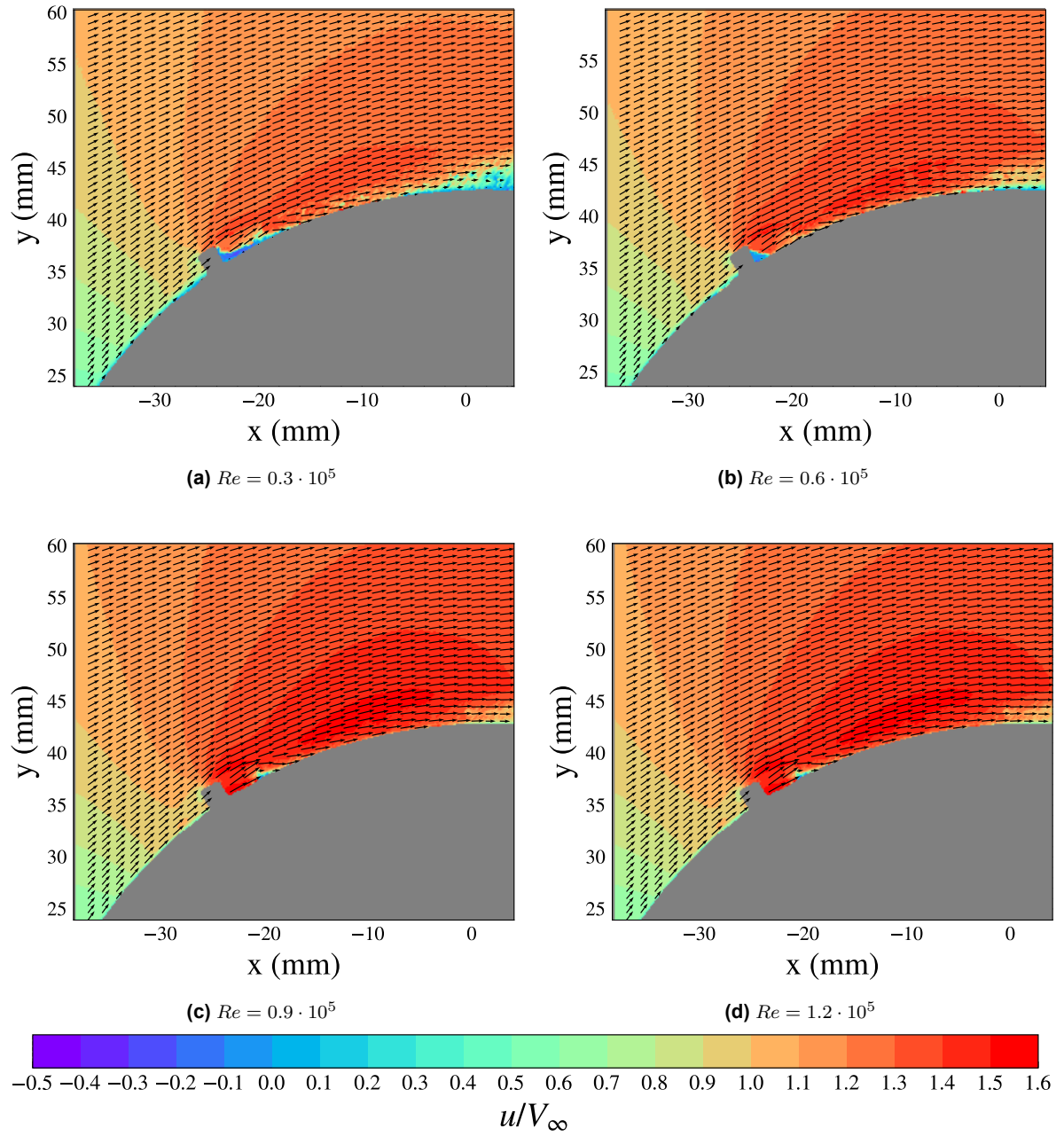


Figure A.7: Cylinder 7. $d = 1.5$ mm, $k = 2.2$ mm, $S/d = 2.5$

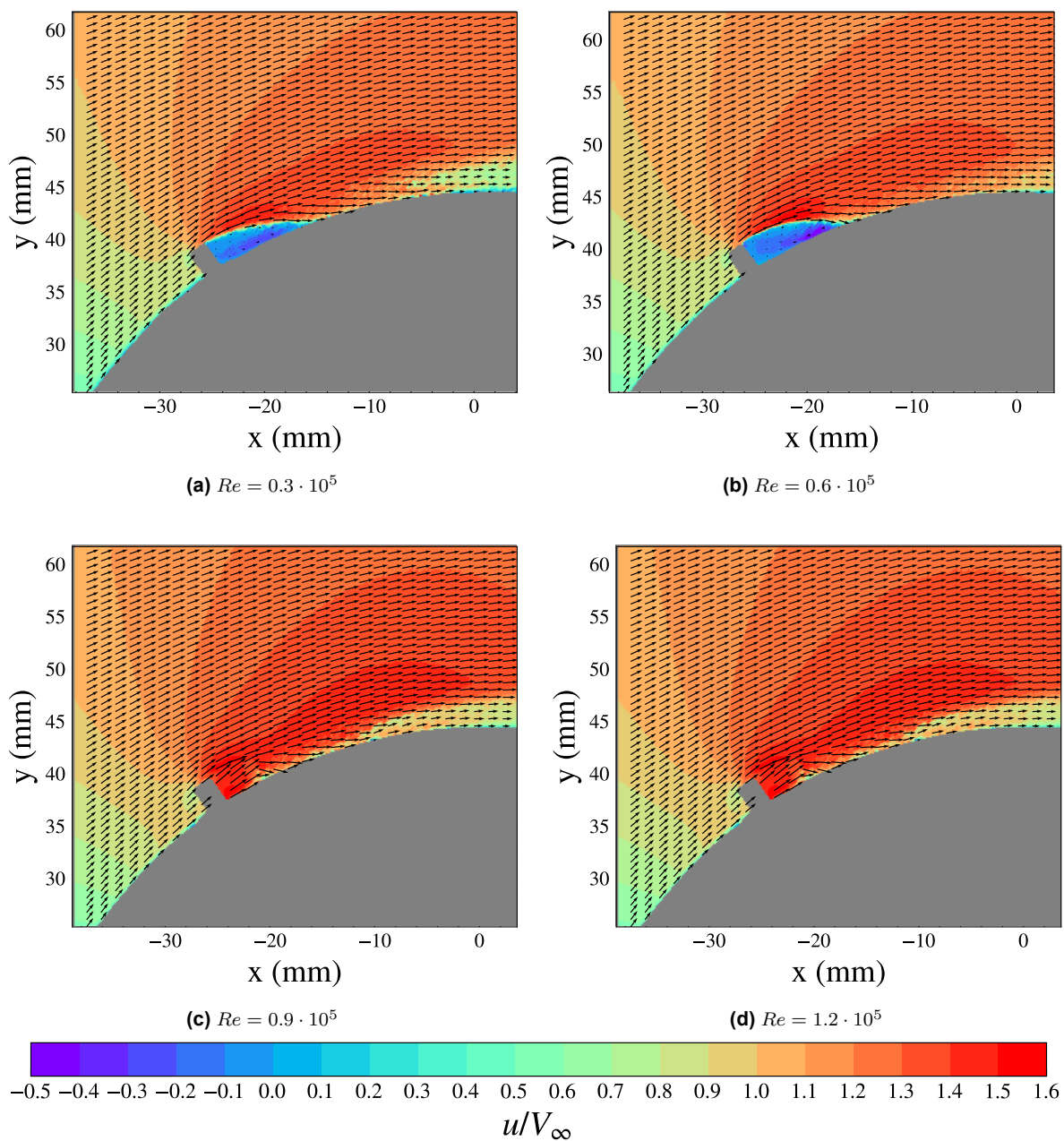


Figure A.8: Cylinder 8. $d = 1.5$ mm, $k = 3$ mm, $S/d = 2.5$

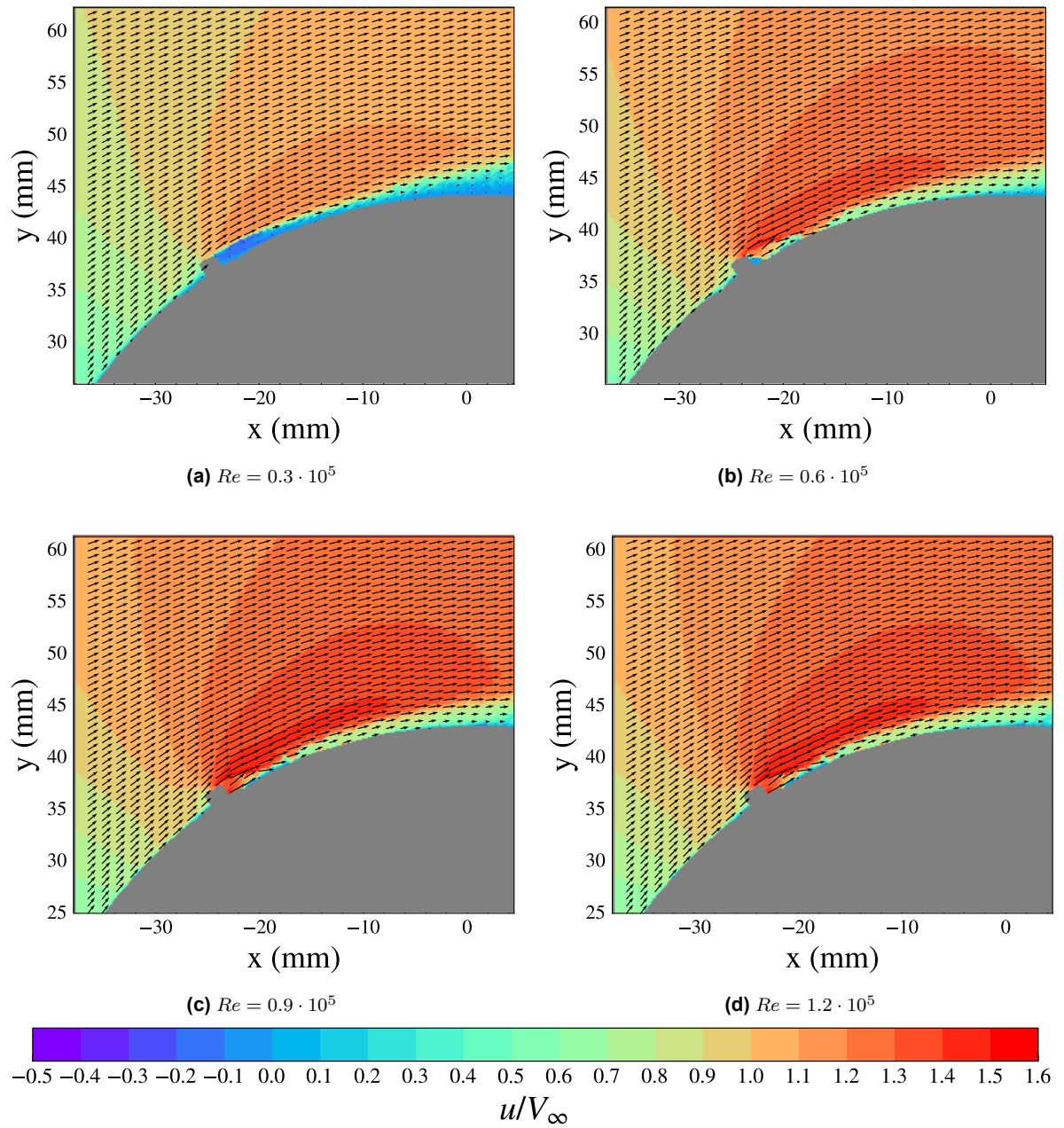


Figure A.9: Cylinder 9. $d = 1.5$ mm, $k = 1.5$ mm, $S/d = 1.5$

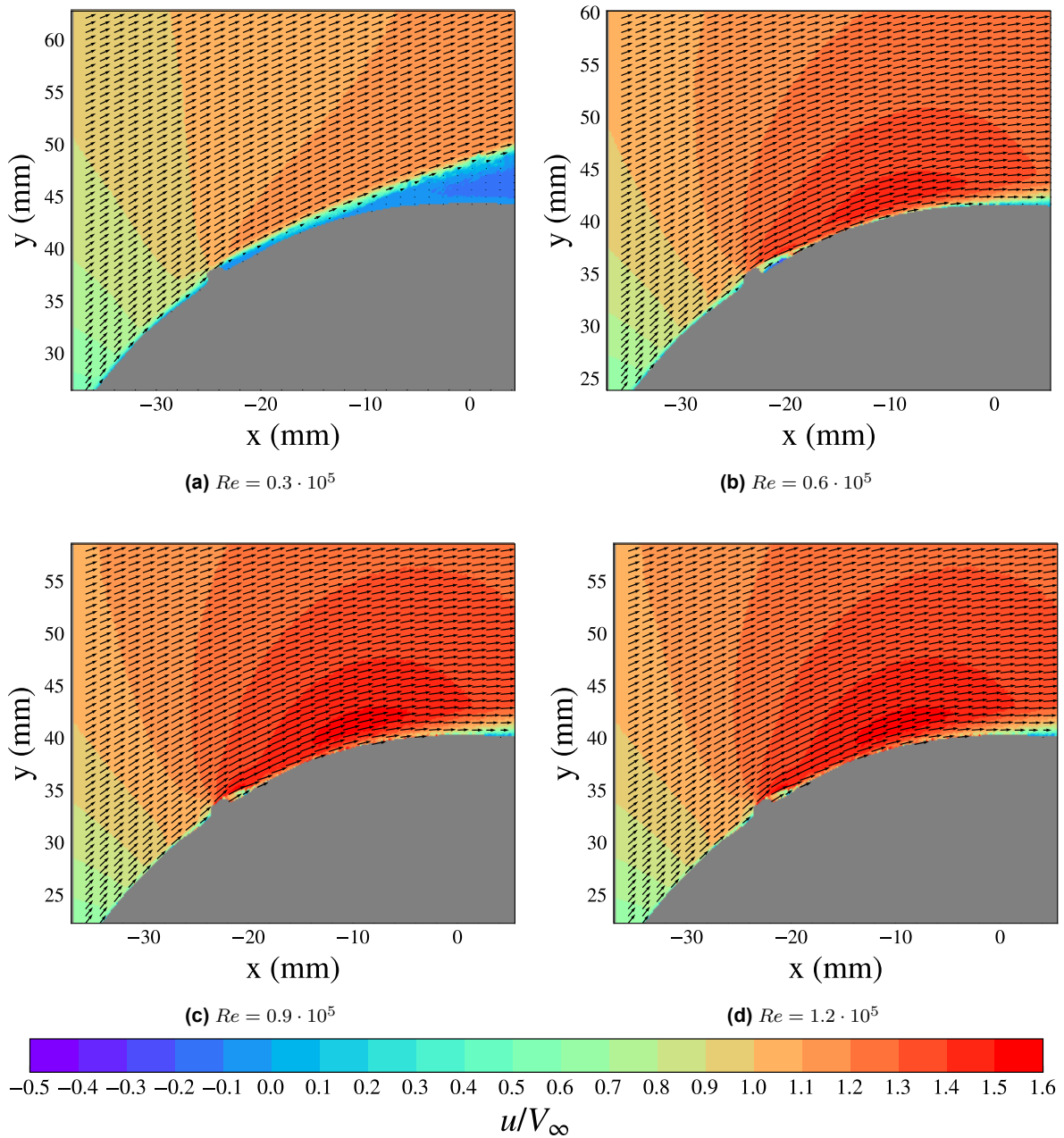


Figure A.10: Cylinder 10. $d = 1.5$ mm, $k = 1$ mm, $S/d = 2.5$

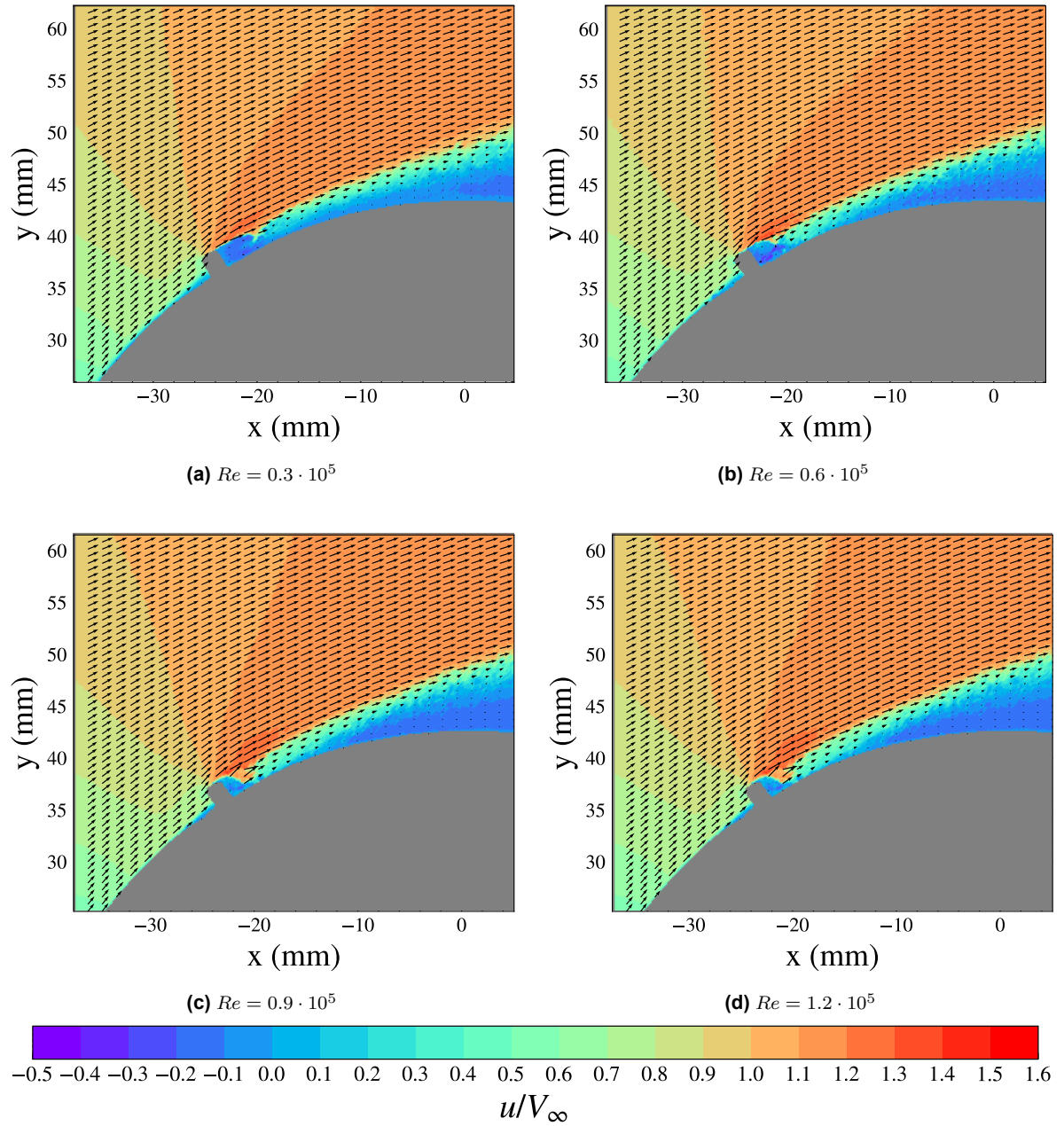


Figure A.11: Cylinder 11. $d = 1.5$ mm, $k = 2.2$ mm, $S/d = 1.5$

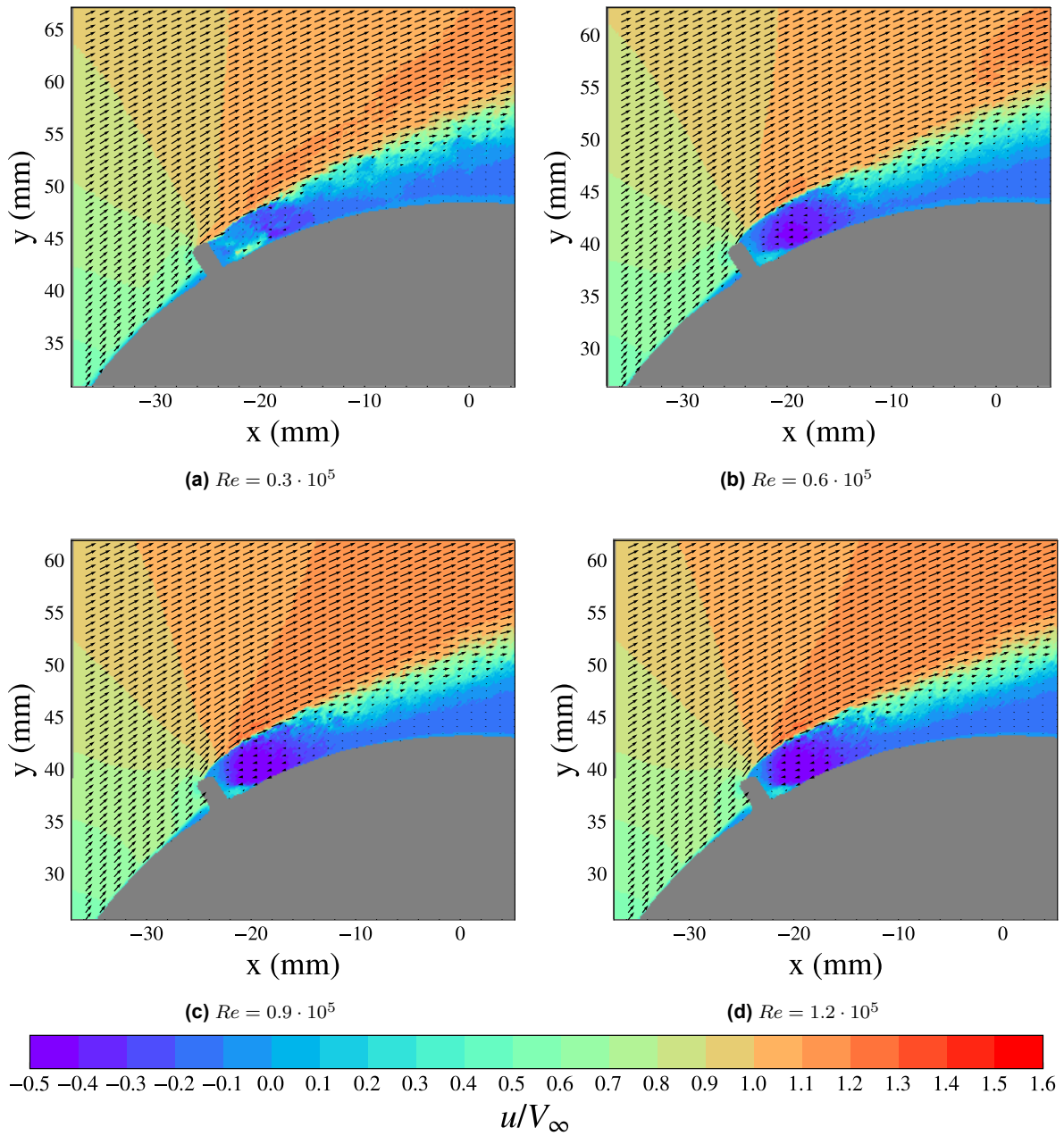


Figure A.12: Cylinder 12. $d = 1.5$ mm, $k = 3$ mm, $S/d = 1.5$